

# ALMA HCN AND HCO<sup>+</sup> J=3–2 OBSERVATIONS OF OPTICAL SEYFERT AND LUMINOUS INFRARED GALAXIES – CONFIRMATION OF ELEVATED HCN-TO-HCO<sup>+</sup> FLUX RATIOS IN AGNS –

MASATOSHI IMANISHI<sup>1,2</sup>

National Astronomical Observatory of Japan, National Institutes of Natural Sciences (NINS), 2-21-1 Osawa, Mitaka, Tokyo 181-8588, Japan

KOUCIHIRO NAKANISHI<sup>2</sup>

National Astronomical Observatory of Japan, National Institutes of Natural Sciences (NINS), 2-21-1 Osawa, Mitaka, Tokyo 181-8588, Japan

AND

TAKUMA IZUMI

Institute of Astronomy, School of Science, The University of Tokyo, 2-21-1 Osawa, Mitaka, Tokyo 181-0015, Japan

*Draft version November 6, 2018*

## ABSTRACT

We present the results of our ALMA observations of three AGN-dominated nuclei in optical Seyfert 1 galaxies (NGC 7469, I Zw 1, and IC 4329 A) and eleven luminous infrared galaxies (LIRGs) with various levels of infrared estimated energetic contributions by AGNs at the HCN and HCO<sup>+</sup> J=3–2 emission lines. The HCN and HCO<sup>+</sup> J=3–2 emission lines are clearly detected at the main nuclei of all sources, except for IC 4329 A. The vibrationally excited ( $v_2=1f$ ) HCN J=3–2 and HCO<sup>+</sup> J=3–2 emission lines are simultaneously covered, and HCN  $v_2=1f$  J=3–2 emission line signatures are seen in the main nuclei of two LIRGs, IRAS 12112+0305 and IRAS 22491–1808, neither of which show clear buried AGN signatures in the infrared. If the vibrational excitation is dominated by infrared radiative pumping, through the absorption of infrared 14  $\mu\text{m}$  photons, primarily originating from AGN-heated hot dust emission, then these two LIRGs may contain infrared-elusive, but (sub)millimeter-detectable, extremely deeply buried AGNs. These vibrationally excited emission lines are not detected in the three AGN-dominated optical Seyfert 1 nuclei. However, the observed HCN  $v_2=1f$  to  $v=0$  flux ratios in these optical Seyferts are still consistent with the intrinsic flux ratios in LIRGs with detectable HCN  $v_2=1f$  emission lines. The observed HCN-to-HCO<sup>+</sup> J=3–2 flux ratios tend to be higher in galactic nuclei with luminous AGN signatures compared with starburst-dominated regions, as previously seen at J=1–0 and J=4–3.

*Subject headings:* galaxies: active — galaxies: nuclei — quasars: general — galaxies: Seyfert — galaxies: starburst — submillimeter: galaxies

## 1. INTRODUCTION

According to widely accepted cold dark matter-based galaxy formation scenarios, small gas-rich galaxies collide, merge, and then evolve into massive galaxies, as seen in the present day universe (White & Rees 1978). Recent observations have shown that supermassive black holes (SMBHs) are ubiquitously present in the spheroidal components of present-day galaxies, and that there is a correlation between the mass of SMBHs and the spheroidal stellar components (Magorrian et al. 1998; Ferrarese & Merritt 2000; Gultekin et al. 2009; McConnell & Ma 2013). When gas-rich galaxies containing SMBHs at their center collide and merge, both active star formation and mass accretion onto SMBHs (= active galactic nucleus (AGN) activity) are predicted to occur, but while deeply embedded in dust and gas (Hopkins et al. 2005, 2006). Observations at low dust extinction wavelengths are necessary to investigate these types of obscured ac-

tivity in gas-rich galaxy mergers.

Molecular rotational J-transition line flux ratios in the (sub)millimeter wavelength range can be a powerful tool for this purpose because dust extinction effects are usually negligible, unless obscuration is extremely high with a hydrogen column density  $N_{\text{H}} \gg 10^{25} \text{ cm}^{-2}$  (Hildebrand 1983). In particular, interferometric observations can probe the properties of nuclear molecular gas in the close vicinity of an AGN, by minimizing contamination from spatially extended (kpc-scale) starburst emission in the host galaxy, and have provided an indication, based on the observations of nearby bright starburst and Seyfert (= modestly luminous AGNs) galaxies, that enhanced HCN J=1–0 emission could be a good AGN signature (Kohno 2005; Krips et al. 2008). Based on this, interferometric HCN and HCO<sup>+</sup> J=1–0 observations have been extensively performed for nearby gas-rich merging luminous infrared galaxies (LIRGs; infrared 8–1000  $\mu\text{m}$  luminosity  $L_{\text{IR}} > 10^{11} L_{\odot}$ ), and it has been confirmed that LIRGs with infrared-identified energetically important obscured AGN signatures tend to display higher HCN-to-HCO<sup>+</sup> flux ratios than starburst-dominated LIRGs (Imanishi et al. 2004, 2006b; Imanishi & Nakanishi 2006; Imanishi et al. 2007a, 2009). HCN and HCO<sup>+</sup> have similar dipole moments ( $\mu = 3.0$  debye

Electronic address: masa.imanishi@nao.ac.jp

<sup>1</sup> Subaru Telescope, National Astronomical Observatory of Japan, National Institutes of Natural Sciences (NINS), 650 North A'ohoku Place, Hilo, Hawaii, 96720, U.S.A.

<sup>2</sup> Department of Astronomical Science, The Graduate University for Advanced Studies (SOKENDAI), Mitaka, Tokyo 181-8588, Japan

and 3.9 debye, respectively), so that they also have similar critical densities at the same J-transitions. It is expected that HCN and HCO<sup>+</sup> emission arises from similar regions inside galaxies. Interpretations of the observed HCN-to-HCO<sup>+</sup> flux ratios are less ambiguous than the flux comparison among molecules with largely different dipole moments (e.g., HCN vs. CO). Using ALMA, a similar enhancement of observed HCN-to-HCO<sup>+</sup> flux ratios was also found at J=4–3 for LIRGs that are infrared-diagnosed to be AGN-important (Imanishi & Nakanishi 2013a,b, 2014; Iono et al. 2013; Garcia-Burillo et al. 2014; Izumi et al. 2015, 2016). These observations suggest that elevated HCN-to-HCO<sup>+</sup> flux ratios could be used to identify AGNs, including deeply buried (= obscured in virtually all directions) ones.

The physical origin of HCN flux enhancement in an AGN is not yet completely understood. Compared with a starburst (nuclear fusion), an AGN (mass accretion onto a SMBH) shows stronger X-ray emission when normalized to the ultraviolet luminosity (Shang et al. 2011; Ranalli et al. 2003). This strong X-ray emission may enhance the HCN abundance, relative to HCO<sup>+</sup> (Meijerink & Spaans 2005; Lintott & Viti 2006), and may be responsible for the enhanced HCN emission in AGNs. Next, because the radiative energy generation efficiency of a mass-accreting SMBH in an AGN (6–42% of Mc<sup>2</sup>) is much higher than the nuclear fusion reaction inside stars in a starburst (~0.7% of Mc<sup>2</sup>), an AGN can produce much higher surface brightness emission, and thereby a larger amount of hot dust (> 100 K) in its close vicinity, than a starburst. HCN abundance enhancement due to high gas/dust temperature chemistry (Harada et al. 2010) may also be the cause of the HCN flux enhancement in AGNs. It is also argued that the HCO<sup>+</sup> abundance can decrease in highly turbulent molecular gas in the close vicinity of a strongly X-ray-emitting AGN (Papadopoulos et al. 2007), which may result in an elevated HCN-to-HCO<sup>+</sup> abundance ratio. In fact, Yamada et al. (2007) and Izumi et al. (2016) made non-LTE calculations of HCN and HCO<sup>+</sup> emission over a wide parameter range and found that an enhanced HCN abundance is required to account for the high HCN-to-HCO<sup>+</sup> flux ratios observed in AGNs. HCN flux enhancement by infrared radiative pumping (Carroll & Goldsmith 1981; Ziurys & Turner 1986; Aalto et al. 1995; Garcia-Burillo et al. 2006; Sakamoto et al. 2010) is also suggested. Namely, HCN can be vibrationally excited by infrared 14  $\mu\text{m}$  photons that are strongly emitted from AGN-heated hot dust, and through its decay back to the vibrational ground level ( $v=0$ ) the HCN rotational J-transition flux at  $v=0$  could be higher than that of collisional excitation alone (Rangwala et al. 2011). However, chemical models also predict that the HCN and HCO<sup>+</sup> abundances around an AGN can vary strongly, depending on the surrounding molecular gas parameters (Meijerink & Spaans 2005; Harada et al. 2013). The proposed decrease in HCO<sup>+</sup> abundance could also occur in turbulent molecular gas in a starburst with strong cosmic rays (Papadopoulos et al. 2007). In addition, HCO<sup>+</sup>, as well as HCN, can be vibrationally excited by absorbing infrared 12  $\mu\text{m}$  photons (Davies et al. 1984; Kawaguchi et al. 1985), and the HCO<sup>+</sup> J-transition flux at  $v=0$  could also be increased through the action of infrared radiative pumping. Given these remaining theoretical ambiguities, further detailed

interferometric observations of galactic nuclei where the energetic roles of AGNs are reasonably well estimated are an important step toward better clarifying whether elevated HCN-to-HCO<sup>+</sup> flux ratios can indeed operate as good indicators of AGNs.

In light of this, we conducted ALMA Cycle 1 HCN J=3–2 (with a rest-frame frequency of  $\nu_{\text{rest}} = 265.89$  GHz) and HCO<sup>+</sup> J=3–2 ( $\nu_{\text{rest}} = 267.56$  GHz) observations of AGN-dominated nuclei in band 6 (211–275 GHz). These high-spatial-resolution ALMA observations enable us to minimize the contamination from spatially extended starburst activity in host galaxies, and thus provide a clearer view on whether AGNs indeed show enhanced HCN-to-HCO<sup>+</sup> flux ratios, compared to starburst galaxies. As spatially resolved pre-ALMA HCN and HCO<sup>+</sup> J=3–2 data for galaxies are still very limited in the literature (Sakamoto et al. 2010; Hsieh et al. 2012; Aalto et al. 2015a), our ALMA Cycle 2 and 3 LIRG data, with various AGN and starburst contributions, are also included so that we can compare the HCN-to-HCO<sup>+</sup> J=3–2 flux ratios of AGN-dominated nuclei to regions of strong starburst contributions.

Observations of HCN and HCO<sup>+</sup> at J=3–2 have several important advantages compared with other J-transition lines. First, our main targets are nearby LIRGs, AGNs, and starbursts, whose redshifts are as large as  $z \sim 0.3$ . HCN and HCO<sup>+</sup> J=3–2 lines can be observed simultaneously for these targets using ALMA. We note that (1) HCN and HCO<sup>+</sup> J=1–0 lines cannot be covered by ALMA if the target redshifts exceed  $z \sim 0.06$ , because these lines are shifted beyond the frequency coverage of ALMA band 3 (84–116 GHz), and (2) HCN and HCO<sup>+</sup> J=2–1 line observations of nearby galaxies are impossible in ALMA Cycles 1, 2, and 3, because ALMA band 5 (163–211 GHz) is not yet open. Second, compared with HCN/HCO<sup>+</sup> J=4–3 observations in ALMA band 7 (275–373 GHz) for nearby galaxies, HCN/HCO<sup>+</sup> J=3–2 observations in band 6 are less affected by the Earth’s atmospheric background noise and thus enable us to obtain higher quality, higher signal-to-noise (S/N) ratio data. Third, the effects of the precipitable water vapor value at the ALMA observing site are smaller in band 6 than in band 7, so that the probability of observation execution is expected to be higher for HCN/HCO<sup>+</sup> J=3–2 in band 6 than HCN/HCO<sup>+</sup> J=4–3 in band 7. Finally, in ALMA band 6, in addition to the HCN J=3–2 and HCO<sup>+</sup> J=3–2 lines, vibrationally excited  $v_2=1$ ,  $l=1f$  (hereafter  $v_2=1f$ ) emission lines of HCN ( $\nu_{\text{rest}} = 267.20$  GHz) and HCO<sup>+</sup> ( $\nu_{\text{rest}} = 268.69$  GHz) can also be simultaneously covered in one shot, with the 5 GHz-wide correlator unit. These  $v_2=1f$  emission lines can be used to investigate how infrared radiative pumping works in observed galaxies and affects rotational excitation at  $v=0$  (Sakamoto et al. 2010; Imanishi & Nakanishi 2013b; Aalto et al. 2015a,b; Imanishi et al. 2016a; Martin et al. 2016). The simultaneous observations of all of these lines make their flux ratios reliable, with the effect of possible systematic uncertainties being minimized.

In this paper, we report the results of our ALMA Cycle 1, 2, and 3 observations of AGN-dominated galactic nuclei, starburst-dominated regions, and the nuclei of AGN-starburst composite LIRGs. Throughout this paper, we adopt  $H_0 = 71 \text{ km s}^{-1} \text{ Mpc}^{-1}$ ,  $\Omega_M = 0.27$ , and  $\Omega_\Lambda = 0.73$  (Komatsu et al. 2009). Molecular lines without the

notation of  $v$  (the vibrational level) refer to  $v=0$  (i.e., the vibrational ground level). HCN refers to H<sup>12</sup>C<sup>14</sup>N.

## 2. TARGETS

Even though our high-spatial-resolution ALMA interferometric observations can eliminate the effects of spatially extended (kpc-scale) *circum-nuclear* starburst activity in the host galaxies, emission from *nuclear* starbursts at the central <200–300 pc of galaxies cannot be clearly separated. To purely probe the emission properties of AGN-affected molecular gas, we have to observe AGNs with the least contamination from *nuclear* starburst activity. Infrared slit spectroscopy at  $>3 \mu\text{m}$  using ground-based telescopes is one of the most powerful tools for selecting such almost pure AGNs, because the presence of nuclear starburst activity can be investigated by polycyclic aromatic hydrocarbon (PAH) emission features, which are not emitted from AGNs but can be produced from nuclear starbursts occurring at a location sufficiently shielded from the AGN’s X-ray radiation (Voit 1992; Moorwood 1986; Genzel et al. 1998; Roche et al. 1991; Imanishi & Dudley 2000; Esquej et al. 2014). We have performed extensive ground-based infrared 3–4  $\mu\text{m}$  (*L*-band) spectroscopy of optical Seyfert nuclei using narrow ( $<1.6''$ ) slits (Imanishi 2002, 2003; Rodriguez-Ardila & Viegas 2003; Imanishi & Wada 2004; Imanishi 2006; Imanishi et al. 2011a), and identified a large number of AGNs with undetectable nuclear starburst signatures.

Our next step is to further select nuclear-starburst-free AGNs which, with ALMA, are expected to emit a detectable amount of molecular emission lines. As our interest lies in AGN-affected molecular gas in the close vicinity of the central AGN engine, we have to estimate the amount of such nuclear AGN-affected molecular gas, rather than the entire amount of molecular gas in the host galaxy. Assuming that dense molecular gas and dust spatially co-exist in the dusty molecular tori around AGNs, AGNs with strong *nuclear* AGN-heated hot dust radiation in the infrared 3–10  $\mu\text{m}$  are expected to accompany bright AGN-affected nuclear molecular emission lines.

Finally, to clearly detect the vibrationally excited ( $v_2=1f$ ) HCN emission line without veiling by the much brighter HCO<sup>+</sup> emission line at  $v=0$  (only  $\sim 400 \text{ km s}^{-1}$  separation) (Sakamoto et al. 2010), AGN-dominated nuclei with *small molecular line widths* are appropriate targets. AGNs whose molecular line full widths at 10% intensity are  $<500 \text{ km s}^{-1}$  are desirable. We target Type 1 unobscured AGNs, because their dusty molecular tori in the close vicinity of AGNs are expected to be preferentially viewed from a *face-on* direction from our line-of-sight, making rotation-originated nuclear molecular line widths small. As long as turbulence-originated line widths are not very large, small observed nuclear molecular line widths are expected.

In summary, Type 1 unobscured AGNs without nuclear PAH emission features and with bright nuclear infrared 3–10  $\mu\text{m}$  continuum fluxes are suitable targets for our purpose. NGC 7469, I Zw 1, and IC 4329 A meet these criteria.

NGC 7469 ( $z=0.0164$ ) is included in both the Center for Astrophysics (CfA) (Huchra & Burg 1992) and 12  $\mu\text{m}$  (Rush et al. 1993) Seyfert galaxy samples, and is classified optically as a Seyfert 1 (Veilleux et al. 1995; Yuan

et al. 2010). It displays circum-nuclear starburst activity at 1–2 arcsec ( $\sim 0.3\text{--}0.7 \text{ kpc}$ ) in radius around the central AGN (Soifer et al. 2003; Galliano et al. 2005; Diaz-Santos et al. 2007; Reunanen et al. 2010). Although the 3.3  $\mu\text{m}$  PAH emission feature, a signature of starbursts, is detected in large aperture ( $>4''$ ) infrared spectroscopy (Imanishi et al. 2010), ground-based infrared  $<1''$ -wide slit spectroscopy targeting the nuclear region shows no detectable 3.3  $\mu\text{m}$  PAH emission feature (Imanishi & Wada 2004), suggesting that nuclear starburst activity is very weak and undetectable. The nuclear infrared 3–4  $\mu\text{m}$  flux of NGC 7469 is one of the highest among observed Seyfert 1 galaxies with no detectable 3.3  $\mu\text{m}$  PAH emission features (Imanishi & Wada 2004). Recent sensitive ground-based 8–13  $\mu\text{m}$  spectroscopy has shown some signatures of an 11.3  $\mu\text{m}$  PAH emission feature from the NGC 7469 nucleus (Honig et al. 2010; Esquej et al. 2014), but the estimated nuclear starburst luminosity is only  $\sim 20\%$  of the AGN luminosity (Esquej et al. 2014; Genzel et al. 1995). Interferometric CO J=2–1 and HCN/HCO<sup>+</sup> J=4–3 observations of the NGC 7469 nucleus revealed that molecular emission lines at the nuclear position are narrow with a full width at 10% intensity  $<400 \text{ km s}^{-1}$  (Davies et al. 2004; Izumi et al. 2015). Detailed results of ALMA Cycle 2 sub-arcsec spatial-resolution observations of NGC 7469 at HCN J=4–3 and HCO<sup>+</sup> J=4–3 were reported by Izumi et al. (2015).

I Zw 1 ( $z=0.0611$ ) is included in the Palomar-Green quasi-stellar objects (PG QSO) catalog and is classified optically as a Seyfert 1 (Schmidt & Green 1983). Imanishi et al. (2011a) performed infrared 3–4  $\mu\text{m}$  (*L*-band)  $1''6$ -wide slit spectroscopy and did not detect a 3.3  $\mu\text{m}$  PAH emission feature in the nuclear region of I Zw 1. The observed nuclear infrared 3–4  $\mu\text{m}$  flux is high among PAH non-detected AGNs. No detectable 11.3  $\mu\text{m}$  PAH emission feature is found at the nucleus (Burtscher et al. 2013). Single-dish CO J=1–0 and HCN J=1–0 observations of I Zw 1 with the IRAM 30-m telescope show narrow molecular line emission with full width at 10% intensity of  $<400 \text{ km s}^{-1}$  (Evans et al. 2006).

IC 4329 A ( $z=0.0160$ ) is an optical Seyfert 1 galaxy in the 12  $\mu\text{m}$  Seyfert galaxy sample (Rush et al. 1993). The nuclear 3–4  $\mu\text{m}$  (*L*-band) spectrum taken with a  $1''6$ -wide slit is dominated by a PAH-free featureless continuum, with one of the highest observed fluxes for this class of object (Imanishi & Wada 2004). The 11.3  $\mu\text{m}$  PAH emission is also not detected in the nuclear region (Honig et al. 2010). The detection of molecular rotational J-transition emission lines in the (sub)millimeter wavelength range toward the IC 4329 A nucleus has not been reported in the published literature.

As a comparison of these AGN-dominated optical Seyfert 1 galactic nuclei, we observed nearby merging LIRGs, because they often display starburst activity, in addition to deeply obscured AGNs. The relative energetic contributions from starbursts and obscured AGNs vary greatly among different LIRGs, but are reasonably estimated based on infrared spectroscopy, as long as emission from obscured AGNs contributes to the observed infrared flux.

IRAS 08572+3915 ( $z = 0.0580$ ) is an ultraluminous infrared galaxy (ULIRG;  $L_{\text{IR}} \gtrsim 10^{12} L_{\odot}$ ) with  $L_{\text{IR}} \sim 10^{12.1} L_{\odot}$  (Table 1), classified optically as a low-ionization nuclear emission-line region (LINER) galaxy (Veilleux et

al. 1999) or a Seyfert 2 (Yuan et al. 2010). It shows a merging double nuclear morphology (northwestern [NW] and southeastern [SE]) with a separation of  $\sim 5$  arcsec (Scoville et al. 2000; Kim et al. 2002; Imanishi & Saito 2014). The NW nucleus (IRAS 08572+3915 NW) is argued to contain an energetically dominant buried AGN, based on infrared spectroscopic and imaging energy diagnostic methods (Dudley & Wynn-Williams 1997; Imanishi & Dudley 2000; Soifer et al. 2000; Spoon et al. 2006; Imanishi et al. 2006a; Armus et al. 2007; Imanishi et al. 2007b; Veilleux et al. 2009; Nardini et al. 2010), and so has been selected as a target to scrutinize elusive buried AGNs through various methods (Imanishi et al. 2007a; Teng et al. 2009, 2015). We conducted ALMA Cycle 0 observations of IRAS 08572+3915 at HCN/HCO<sup>+</sup>/HNC J=4–3 lines and reported their molecular line flux ratios (Imanishi & Nakanishi 2014); detailed descriptions about IRAS 08572+3915 can be found in the paper cited. The CO J=1–0 emission line was detected in only the NW nucleus, based on pre-ALMA interferometric observations (Evans et al. 2002).

The Superantennae (IRAS 19254–7245;  $z = 0.0617$ ) is a ULIRG with  $L_{\text{IR}} \sim 10^{12.1} L_{\odot}$  (Table 1), classified optically as a Seyfert 2 (Mirabel et al. 1991). Infrared (Risaliti et al. 2003; Imanishi et al. 2010) and X-ray (Braito et al. 2003, 2009) observations support the presence of an energetically important obscured AGN. Due to its very low declination ( $-72^{\circ}$ ), no interferometric molecular gas observations were reported in the published literature prior to ALMA.

IRAS 12112+0305 ( $z = 0.0730$ ) is a ULIRG with  $L_{\text{IR}} \sim 10^{12.3} L_{\odot}$  (Table 1), classified optically as a LINER (Veilleux et al. 1999) or a Seyfert 2 (Yuan et al. 2010). It consists of two merging nuclei (northeastern [NE] and southwestern [SW]), with a separation of  $\sim 3$  arcsec (Kim et al. 2002). Infrared spectra at 3–35  $\mu\text{m}$  from nuclear emission, both combined and separately at individual nuclei, are dominated by strong PAH emission features (Imanishi et al. 2006a, 2007b; Nardini et al. 2009; Veilleux et al. 2009; Imanishi et al. 2010). Such infrared spectral shapes are usually seen when the observed infrared spectra are dominated by starburst emission (Moorwood 1986; Genzel et al. 1998; Imanishi & Dudley 2000). No clear observational AGN signatures are recognizable in infrared energy diagnostic methods. If a luminous AGN is present in either of the nuclei, the AGN must be deeply buried in gas and dust so as to be infrared elusive. The PAH-to-infrared luminosity ratio is smaller than that expected from modestly obscured starburst-dominated galaxies by a factor of 3–6, depending on the 3.3  $\mu\text{m}$ , 6.2  $\mu\text{m}$ , and 11.3  $\mu\text{m}$  PAH features (Imanishi et al. 2007b, 2010), suggesting that PAH emission is more flux-attenuated than in the comparison starburst galaxies, or that an elusive AGN contributes to the infrared luminosity without producing PAH emission. Interferometric observations detected CO J=1–0 emission from both nuclei, with a flux approximately three times higher at the NE nucleus than at the SW nucleus (Evans et al. 2002).

IRAS 22491–1808 ( $z = 0.0776$ ) is a ULIRG with  $L_{\text{IR}} \sim 10^{12.2} L_{\odot}$  (Table 1). We reported the results of our ALMA Cycle 0 observations of IRAS 22491–1808 at HCN/HCO<sup>+</sup>/HNC J=4–3 lines in Imanishi & Nakanishi (2014), and detailed information relating to this ULIRG

is presented in that paper. In summary, similar to IRAS 12112+0305, the infrared spectra of IRAS 22491–1808 at 3–35  $\mu\text{m}$  are characterized by large equivalent width PAH emission features (Imanishi et al. 2007b; Veilleux et al. 2009; Imanishi et al. 2010). The observed infrared emission at 3–35  $\mu\text{m}$  is interpreted as originating from starburst activity, and any putative AGN in this ULIRG must be particularly deeply embedded to elude infrared spectroscopic observations. Similar to IRAS 12112+0305, the PAH-to-infrared luminosity ratio is smaller than that expected from modestly obscured starburst-dominated galaxies by a factor of 3–8, depending on the 3.3  $\mu\text{m}$ , 6.2  $\mu\text{m}$ , and 11.3  $\mu\text{m}$  PAH features (Imanishi et al. 2007b, 2010). The observed HCN-to-HCO<sup>+</sup> J=4–3 flux ratios are substantially higher than those from starburst regions (Imanishi & Nakanishi 2014). Obtaining further molecular line data is desirable for a better understanding of the origin of the observed molecular line emission in this ULIRG.

NGC 1614 (IRAS 04315–0840) at  $z = 0.0160$  is a well-studied nearby LIRG with  $L_{\text{IR}} \sim 10^{11.7} L_{\odot}$  (Table 1). We observed NGC 1614 at HCN/HCO<sup>+</sup>/HNC J=4–3 lines in ALMA Cycle 0, as representative of starburst-dominated galaxies (Imanishi & Nakanishi 2013a); detailed properties of NGC 1614 can be found in the paper cited. In summary, NGC 1614 shows optical and infrared 2–35  $\mu\text{m}$  spectra whose emission properties are explained solely by nuclear starburst activity, with a spatial extension of a few arcsec (Alonso-Herrero et al. 2001; Miles et al. 1996; Soifer et al. 2001; Diaz-Santos et al. 2008; Imanishi et al. 2011b; Pereira-Santaella et al. 2012). In general, dust extinction is smaller in LIRGs than ULIRGs (Soifer et al. 2000, 2001), so that a quantitative discussion of starbursts and any putative AGNs is easier in LIRGs. The detected starburst-origin emission line luminosities in the infrared are high enough to account for the observed total infrared luminosity (Imanishi et al. 2010), leaving little room for the presence of an energetically significant AGN in NGC 1614, unlike the ULIRGs, IRAS 12112+0305, and IRAS 22491–1808. Low HCN-to-HCO<sup>+</sup> J=4–3 flux ratios are found in our ALMA Cycle 0 data at multiple starburst regions in NGC 1614 (Imanishi & Nakanishi 2013a).

The above five LIRGs were observed in ALMA Cycle 2. In addition to them, six new LIRGs have been observed in ALMA Cycle 3 at HCN/HCO<sup>+</sup> J=3–2, and their data have recently been sent to us. We include these six LIRGs (IRAS 12127–1412, IRAS 15250+3609, PKS 1345+12, IRAS 06035–7102, IRAS 13509+0442, and IRAS 20414–1651) in this paper.

IRAS 12127–1412 ( $z = 0.1332$ ) is a ULIRG with  $L_{\text{IR}} \sim 10^{12.2} L_{\odot}$  (Table 1). It shows two nuclei (NE and SW) with a separation of  $\sim 10$  arcsec (Kim et al. 2002; Imanishi & Saito 2014). The optical classification of this ULIRG is a LINER (Veilleux et al. 1999) or an HII-region (Yuan et al. 2010). The NE nucleus is thought to contain a luminous buried AGN, based on various infrared energy diagnostic methods (Imanishi et al. 2006a, 2007a; Veilleux et al. 2009; Imanishi et al. 2010; Nardini et al. 2008, 2009, 2010). The results of our ALMA Cycle 0 observations of IRAS 12127–1412 at HCN/HCO<sup>+</sup>/HNC J=4–3 lines were reported in Imanishi & Nakanishi (2014). These molecular emission lines were detected at the NE nucleus, but not at the SW

nucleus.

IRAS 15250+3609 ( $z = 0.0552$ ) is a ULIRG with  $L_{\text{IR}} \sim 10^{12.0} L_{\odot}$  (Table 1). It is classified optically as a LINER (Veilleux et al. 1995) or an AGN-starburst composite (Yuan et al. 2010). The presence of a luminous buried AGN is suggested from (1) a steeply rising continuum at  $>3.5 \mu\text{m}$ , most likely due to AGN-heated hot dust emission (Imanishi et al. 2010), (2) low equivalent widths of PAH emission features at  $>5 \mu\text{m}$  (Spoon et al. 2002; Nardini et al. 2010; Imanishi et al. 2011b; Stierwalt et al. 2013), and (3) a high emission surface brightness (Imanishi et al. 2011b). Nardini et al. (2010) estimated that  $\sim 50\%$  of the bolometric luminosity of IRAS 15250+3609 is explained by the buried AGN.

PKS 1345+12 (IRAS 13451+1232;  $z = 0.1215$ ) is a ULIRG with  $L_{\text{IR}} \sim 10^{12.3} L_{\odot}$  (Table 1). It is classified optically as a Seyfert 2 (Veilleux et al. 1999; Yuan et al. 2010). It has two nuclei with a separation of  $\sim 2$  arcsec along the east-west (EW) direction (Scoville et al. 2000; Kim et al. 2002; Imanishi & Saito 2014), and CO J=1–0 emission is detected in the western nucleus (Evans et al. 1999). Infrared  $\sim 2 \mu\text{m}$  spectroscopy detected an AGN-origin broad (full width at half maximum [FWHM]  $> 2000 \text{ km s}^{-1}$ ) Pa $\alpha$  ( $1.875 \mu\text{m}$ ) emission line, due to smaller dust extinction effects compared with the optical (Veilleux et al. 1997), suggesting that the hidden AGN is only modestly obscured. Based on the luminosity of the detected broad Pa $\alpha$  emission line, Veilleux et al. (1997) argued that the AGN could be responsible for the bulk of the bolometric luminosity of PKS 1345+12. A rising infrared 2.5–5  $\mu\text{m}$  spectrum with a non-detectable 3.3  $\mu\text{m}$  PAH emission feature also supports the AGN-dominated nature of this ULIRG (Imanishi et al. 2010). PKS 1345+12 shows an excess of the radio-to-infrared luminosity ratio, compared with the majority of LIRGs (Drake et al. 2004), suggesting that the AGN is radio-loud.

IRAS 06035–7102 ( $z = 0.0795$ ) is a ULIRG with  $L_{\text{IR}} \sim 10^{12.2} L_{\odot}$  (Table 1). It is classified optically as a LINER (Duc et al. 1997), although there are several indications that an optically elusive luminous buried AGN exists due to (1) low PAH emission equivalent widths and strong absorption features by dust and ice at  $>3 \mu\text{m}$  (Spoon et al. 2002; Dartois et al. 2007; Farrah et al. 2009; Imanishi et al. 2010) and (2) a steeply rising continuum at  $>3.5 \mu\text{m}$  (Imanishi et al. 2010). Nardini et al. (2010) argued that the putative buried AGN accounts for  $\sim 20\%$  of the bolometric luminosity of IRAS 06035–7102.

IRAS 13509+0442 ( $z = 0.1364$ ) is a ULIRG with  $L_{\text{IR}} \sim 10^{12.3} L_{\odot}$  (Table 1). It is classified optically as an HII region (Veilleux et al. 1999) or an AGN-starburst composite (Yuan et al. 2010). Its infrared 2.5–35  $\mu\text{m}$  spectrum is characterized by large equivalent width PAH emission features (Imanishi et al. 2007b, 2010), suggesting that the observed 2.5–35  $\mu\text{m}$  infrared flux is dominated by starburst emission, with no obvious AGN signatures. However, the observed PAH-to-infrared luminosity ratio is a factor of 2–4 lower than that expected from modestly obscured starburst-dominated galaxies (Imanishi et al. 2007b, 2010).

IRAS 20414–1651 ( $z = 0.0870$ ) is a ULIRG with  $L_{\text{IR}} \sim 10^{12.3} L_{\odot}$  (Table 1), classified optically as an HII region (Veilleux et al. 1999) or an AGN-starburst composite (Yuan et al. 2010). Similar to IRAS 13509+0442, the

PAH-emission-dominated infrared 2.5–35  $\mu\text{m}$  spectrum of IRAS 20414–1651 (Imanishi et al. 2007b; Nardini et al. 2009; Veilleux et al. 2009; Imanishi et al. 2010) suggests that the observed infrared 2.5–35  $\mu\text{m}$  flux is dominated by starburst activity, without any discernible AGN signatures in the infrared. Yet, the observed PAH-to-infrared luminosity ratio is low by a factor of 5–12, compared to modestly obscured starburst-dominated galaxies (Imanishi et al. 2007b, 2010).

Table 1 presents the basic properties of these three optical Seyfert 1 galaxies and eleven LIRGs.

### 3. OBSERVATIONS AND DATA ANALYSIS

Our observations of the three AGN-dominated Seyfert 1 galactic nuclei (NGC 7469, I Zw 1, IC 4329 A) in band 6 were made within the scope of our ALMA Cycle 1 program 2012.1.00034.S (PI = M. Imanishi). Observations of the eleven LIRGs were performed within our ALMA Cycle 2 program 2013.1.00032.S (PI = M. Imanishi) and Cycle 3 program 2015.1.00027.S (PI = M. Imanishi). Our Cycle 1 program was transferred to Cycle 2, and actual observations were conducted during the ALMA Cycle 2 observing period. Observation details are summarized in Table 2. Although HCN/HCO<sup>+</sup> J=4–3 and HNC J=3–2/J=4–3 data were also taken for LIRGs during our Cycle 2 and 3 programs, we focus on the HCN/HCO<sup>+</sup> J=3–2 emission line properties in this paper, because only HCN/HCO<sup>+</sup> J=3–2 emission line data were obtained for the AGN-dominated optical Seyfert 1 nuclei. The remaining emission lines of LIRGs will be discussed by Imanishi et al. (2016c).

We adopted the widest 1.875-GHz-width mode in each spectral window to cover as wide a frequency as possible. To simultaneously observe our target lines, HCN J=3–2 ( $\nu_{\text{rest}} = 265.89 \text{ GHz}$ ), HCO<sup>+</sup> J=3–2 ( $\nu_{\text{rest}} = 267.56 \text{ GHz}$ ), HCN  $v_2=1f$  J=3–2 ( $\nu_{\text{rest}} = 267.20 \text{ GHz}$ ), and HCO<sup>+</sup>  $v_2=1f$  J=3–2 ( $\nu_{\text{rest}} = 268.69 \text{ GHz}$ ), we used three spectral windows, each of which covered (1) HCN J=3–2, (2) HCN  $v_2=1f$  J=3–2 and HCO<sup>+</sup> J=3–2, and (3) HCO<sup>+</sup>  $v_2=1f$  J=3–2, respectively. Because the interferometer in ALMA band 6 can cover 5 GHz at the upper sideband or lower sideband, HCN and HCO<sup>+</sup> at both  $v=0$  (the vibrational ground level) and  $v_2=1$  (the vibrationally excited level) could be observed simultaneously at J=3–2, which is not possible at J=4–3 in ALMA band 7.

We began our data analysis from calibrated data provided by the Joint ALMA Observatory, using CASA (<https://casa.nrao.edu>). We first checked the visibility plots to see if the signatures of the targeted bright emission lines were visible. The presence of HCN J=3–2 and HCO<sup>+</sup> J=3–2 emission lines was evident in the visibility plots of all observed galaxies, except for IC 4329 A. We estimated the continuum flux level using channels that were unaffected by strong emission lines. The estimated continuum levels were subtracted using the task “uvcontsub”; the task “clean” was then applied to create final continuum-subtracted molecular line data. The clean task was also applied to the extracted continuum data themselves. For these clean procedures, 40-channel binning of velocity channel with  $\sim 0.5 \text{ km s}^{-1}$  spacing for each (resulting resolution is  $\sim 20 \text{ km s}^{-1}$ ) and a pixel scale of  $0''.1 \text{ pixel}^{-1}$  were basically utilized. For LIRGs observed in ALMA Cycle 3, data were taken and delivered with four channels binning (Spec Avg. = 4 in the

ALMA Observing Tool) to reduce the ALMA data rate, for which we used 20-channel spectral binning. The net velocity resolution was  $\sim 40 \text{ km s}^{-1}$ . Since these LIRGs observed in ALMA Cycle 3 showed large line widths with  $>200 \text{ km s}^{-1}$  in FWHM for bright molecular emission lines (see §3), we can properly trace their emission line profiles and estimate their fluxes based on Gaussian fitting. As some of our targets displayed spatially extended structures, we applied the primary beam correction to all data, although its effects are relatively limited as long as we discuss emission from the central few arcsec regions. When we created the  $\sim 20 \text{ km s}^{-1}$  resolution spectrum of The Superantennae (the broadest molecular line source) from the cleaned data, it was found that continuum levels in the spectral windows that contained the HCN J=3–2 and HCO<sup>+</sup> J=3–2 emission lines were negative in our first continuum determination due to continuum over-subtraction. We thus re-determined the continuum levels in these spectral windows using only a small number of data points at the edge of each spectral window, sufficiently separated from the broad HCN/HCO<sup>+</sup> J=3–2 emission line peaks. In the revised determination, signals outside the emission lines in the continuum-subtracted spectra became almost zero. However, it was uncertain whether data at the edge of these spectral windows were completely line-free. For The Superantennae, continuum determination ambiguities could be larger than for other sources. According to the ALMA Cycle 1, 2, and 3 Proposer’s Guides, the absolute calibration uncertainty of our ALMA band 6 data should be  $<10\%$ . The position reference frames are FK5 for objects observed in ALMA Cycles 1 and 2, and ICRS for those observed in ALMA Cycle 3.

#### 4. RESULTS

Figure 1 displays continuum maps of the three optical Seyfert 1 galaxies, NGC 7469, I Zw 1, and IC 4329 A. Continuum emission at  $\sim 250\text{--}260 \text{ GHz}$  (observed frame) is clearly detected at the nuclear regions in all sources. In NGC 7469, continuum emission is also detected in the three starburst regions, which we denote as SB1, SB2, and SB3. The observed continuum emission properties are summarized in Table 3.

Continuum maps of the LIRGs observed in ALMA Cycles 2 and 3 are shown in Figures 2 and 3, respectively. Continuum emission is detected in the nuclei of all galaxies. In IRAS 12112+0305, the emission is seen both at the NE and SW nuclei, with the NE nucleus brighter than that of the SW. In NGC 1614, continuum emission is spatially extended, and arises primarily from two distinct regions. We investigate the possible continuum emission signal for the fainter IRAS 08572+3915 SE and IRAS 12127–1412 SW nuclei, but detection is  $<3\sigma$  within  $1''$  around the near-infrared position defined by Kim et al. (2002). The fainter northern nucleus of The Superantennae, located at  $\sim 1''.5$  west and  $\sim 8''$  north of the main southern nucleus (Reunanen et al. 2007; Jia et al. 2012), is also undetected with  $>3\sigma$  in the continuum map within  $1''$  around the expected position. For IRAS 22491–1808, we attribute the detected nuclear position in the continuum to the eastern nucleus (Kim et al. 2002; Haan et al. 2011). The fainter secondary western nucleus,  $\sim 2''$  separated from the main eastern nucleus (Kim et al. 2002), is not clearly detected. For PKS 1345+12, the coordinate

of the ALMA continuum emission peak agrees with that of a VLBI radio emission peak (Ma et al. 1998), and we regard that the detected continuum emission originates from the CO J=1–0 detected western nucleus (Evans et al. 1999).

For IRAS 13509+0442 in Figure 3, continuum emission is detected not only at the nucleus but also at (13 53 31.66, +04 28 13.1)J2000,  $\sim 1''$  east and  $8\text{--}9''$  north of the IRAS 13509+0442 nucleus. This source is detected also in our band 7 continuum map at  $\sim 313 \text{ GHz}$  at the same position with  $\sim 3.6 \text{ mJy}$  (Imanishi et al. 2016c). In the Sloan Digital Sky Survey (SDSS) optical image, two sources were detected at  $\sim 10''$  north of IRAS 13509+0442, identified as SDSS J135331.89+042816.4 ( $z=0.186$  galaxy) and J135331.44+042813.8, but their positions were significantly ( $>3''$ ) offset from our ALMA continuum-detected source. Further high-spatial-resolution multiple-frequency data will help to unravel the nature of this optically faint, millimeter-bright source.

In Figure 4, we show the full frequency coverage spectra, within the beam size, at the nuclear positions of three optical Seyfert 1 galaxies and three starburst regions (SB1, SB2, and SB3) of NGC 7469. To investigate the emission properties from the entire starburst ring of NGC 7469, we also present an area-integrated spectrum in Figure 4e, by integrating signals at the annular region with  $0''.8\text{--}2''.5$  radius, centered at the nuclear position of NGC 7469.

The full frequency coverage spectra for the eleven LIRGs are shown in Figure 5. Spectra at the nuclear positions are shown, within the beam size, with the exception of NGC 1614. In the spectrum of IRAS 15250+3609 in Figure 5(j), a broad dip is visible at the higher frequency side of the HCO<sup>+</sup> J=3–2 emission. A similar profile was observed for HCO<sup>+</sup> J=4–3 and J=3–2 emission lines in the ULIRG Arp 220 (Sakamoto et al. 2009), and was interpreted as the P Cygni profile due to outflow. It is likely that IRAS 15250+3609 displays similar HCO<sup>+</sup> outflow activity. A similar dip, however, is not clearly evident at the higher frequency side of the HCN J=3–2 emission line, suggesting that a larger fraction of HCO<sup>+</sup> is in the outflow component than HCN. A narrow dip at the lower frequency side of the HCO<sup>+</sup> J=3–2 emission is interpreted to be of inflow origin, as seen in some fraction LIRGs (Veilleux et al. 2013). In Figure 5(n), no significant molecular emission line was observed at the position of the NE source detected in the continuum map of IRAS 13509+0442.

Integrated intensity (moment 0) maps were created for the HCN J=3–2 and HCO<sup>+</sup> J=3–2 emission lines, by summing velocity channels with discernible signal signs, with no cut-off in signal-to-noise ratios. Because NGC 7469 and NGC 1614 show morphologies with multiple emission components, their moment 0 maps are presented in Figures 6 and 7, respectively. Figure 8 shows the moment 0 maps of the remaining galaxies whose molecular emission predominantly arises from nuclear regions only. The HCN J=3–2 and HCO<sup>+</sup> J=3–2 emission line properties in these moment 0 maps are summarized in Tables 4 and 5, respectively. The peak positions of the HCN J=3–2 and HCO<sup>+</sup> J=3–2 emission lines spatially agree with the continuum emission peaks within one pixel ( $0''.1$ ) in both the RA and DEC direc-

tions, with the exception of NGC 1614. The secondary nuclei of IRAS 08572+3915, The Superantennae, IRAS 22491–1808, IRAS 12127–1412 and PKS 1345+12 are not detected with  $>3\sigma$  in the moment 0 maps of the HCN J=3–2 and HCO<sup>+</sup> J=3–2 emission lines.

For NGC 1614, the peak positions of the HCN J=3–2 and HCO<sup>+</sup> J=3–2 moment 0 maps in Figure 7 are significantly offset from the continuum peak positions in Figure 2. The molecular gas emission peaks in the moment 0 maps of NGC 1614 agree within one pixel between HCN J=3–2 and HCO<sup>+</sup> J=3–2. We denote the northern peak at (04 34 00.00, –08 34 44.4)J2000 and southern peak at (04 33 59.98, –08 34 45.2)J2000 as SB1 and SB2, respectively, based on the HCN J=3–2 moment 0 map of NGC 1614. Full frequency coverage spectra of NGC 1614 at the SB1 and SB2 peaks, within the beam size, are shown in Figure 5(f) and 5(g), respectively. An area-integrated spectrum in a circular region with a radius of  $2''.5$  around (04 34 00.03, –08 34 44.6)J2000 is also shown in Figure 5(h).

Gaussian fits for the HCN J=3–2 and HCO<sup>+</sup> J=3–2 emission lines in the spectra, within the beam size, at the individual multiple positions of NGC 7469 and NGC 1614 are shown in Figures 6 and 7, respectively. Figure 9 displays Gaussian fits for the remaining sources. Estimates of the HCN J=3–2 and HCO<sup>+</sup> J=3–2 emission line fluxes are based on the peak pixel values in the moment 0 maps and Gaussian fits within the beam size, and are summarized in Tables 4 and 5, respectively. Both estimates generally agree within  $\sim 20\%$ . We will adopt the fluxes estimated from Gaussian fits for these detected emission lines. For the area-integrated spectra of NGC 7469 and NGC 1614, only flux estimates based on Gaussian fits are available, and will be used for our discussion.

Zoom-in spectra of the AGN-dominated nuclei of the two optical Seyfert 1 galaxies with clearly detectable HCN and HCO<sup>+</sup> J=3–2 emission lines (NGC 7469 and I Zw 1) are displayed in Figure 10, to better investigate the HCN and HCO<sup>+</sup>  $v_2=1f$  J=3–2 emission lines. Their presence is, however, unclear. We created their moment 0 maps by summing ten velocity channels at the expected frequencies of the HCN and HCO<sup>+</sup>  $v_2=1f$  J=3–2 lines, but there is no signature of these emission lines at all. The  $3\sigma$  upper limit, relative to the rms noise, is shown in Table 6.

In the spectra of IRAS 08572+3915, IRAS 12112+0305 NE, IRAS 22491–1808, and IRAS 20414–1651 in Figure 5, an emission tail is recognizable at the lower frequency side of the HCO<sup>+</sup> J=3–2 emission line. Figure 10 displays zoomed-in spectra around the HCO<sup>+</sup> J=3–2 emission lines for these four sources, to better distinguish the emission tails. As these tails are not visible at the higher frequency side of the HCO<sup>+</sup> J=3–2 emission lines, the most natural interpretation for the lower frequency side of the tails is the contribution from the HCN  $v_2=1f$  J=3–2 emission line (Aalto et al. 2015a,b).

IRAS 15250+3609 shows a weak emission sub-peak at the expected frequency of the HCN  $v_2=1f$  J=3–2 line, at the lower frequency side of the strong HCO<sup>+</sup> J=3–2 emission (Figure 5). However, a similar weak emission sub-peak is also observed at the lower frequency side of the HCN J=3–2 emission line (Figure 5). Figure 11 compares the velocity profile of the HCN J=3–2 and HCO<sup>+</sup>

J=3–2 emission lines, after normalizing the Gaussian-fit peak flux for the main bright emission component. The emission line flux of the sub-peak component, relative to the main component, is higher for HCO<sup>+</sup> J=3–2 than HCN J=3–2. Although this could be due partly to the contribution from the HCN  $v_2=1f$  J=3–2 emission to the sub-peak component of HCO<sup>+</sup> J=3–2, the expected HCN  $v_2=1f$  J=3–2 emission peak for  $z=0.0552$  is slightly offset from the observed sub-peak component of HCO<sup>+</sup> in velocity (Figure 11). It is more likely that the outflow-origin redshifted and blueshifted components, relative to the main molecular emission component at the nucleus, are stronger for HCO<sup>+</sup> than HCN, which produces stronger P Cygni profile for HCO<sup>+</sup>. A similar trend is seen also at the J=4–3 data of HCN and HCO<sup>+</sup> for IRAS 15250+3690 (Imanishi et al. 2016c). We made moment 0 maps of the sub-peak component of the HCN J=3–2 (10 velocity channels) and HCO<sup>+</sup> J=3–2 (7 velocity channels) and detected these emission lines with 0.70 [Jy beam<sup>-1</sup> km s<sup>-1</sup>] ( $5.8\sigma$ ) and 0.72 [Jy beam<sup>-1</sup> km s<sup>-1</sup>] ( $9.2\sigma$ ) for HCN J=3–2 and HCO<sup>+</sup> J=3–2, respectively. The peak position of the HCO<sup>+</sup> J=3–2 sub-peak component spatially coincides with the continuum peak, but that of HCN J=3–2 is shifted to the north with 2 pix ( $0''.2$ ). However, the position determination accuracy of the HCN J=3–2 sub-peak component is on the order of (beam-size)/(signal-to-noise-ratio)  $\sim 1.21/5.8 \sim 0''.21$ . We see no clear evidence that the sub-peak component is spatially offset from the continuum peak at the nucleus. If the sub-peak component is of outflow origin, the outflow is compact and is located close to the nucleus in the moment 0 maps. Since the continuum flux at  $\sim 250$  GHz is  $\sim 11$  mJy beam<sup>-1</sup> (Table 3), the flux attenuation by outflow of HCO<sup>+</sup> gas at J=3–2 is  $\sim 20\%$ , or an optical depth with  $\tau \sim 0.2$ , for the broad absorption component at  $v_{\text{opt}} = 15800\text{--}16400$  km s<sup>-1</sup> (Figure 11). For the narrow absorption component at  $v_{\text{opt}} \sim 16800$  km s<sup>-1</sup> (Figure 11), which is likely to be of inflow origin, the flux attenuation is  $>40\%$ .

For IRAS 08572+3915, IRAS 12112+0305 NE, IRAS 22491–1808, and IRAS 20414–1651, we created the integrated intensity (moment 0) maps by integrating signals marked with the horizontal solid straight lines (bracketed by the short vertical solid lines) in Figure 10, where the bulk of the possible HCN  $v_2=1f$  J=3–2 emission lines are covered, while contamination from HCO<sup>+</sup> J=3–2 emission lines is minimized, based on our Gaussian fits of the HCO<sup>+</sup> J=3–2 emission lines. In the HCN  $v_2=1f$  J=3–2 emission line moment 0 maps of IRAS 12112+0305 NE and IRAS 22491–1808, the HCN  $v_2=1f$  J=3–2 emission line was detected with  $4.5\sigma$  and  $4\sigma$ , respectively (Table 6), although a possible contribution from the bright HCO<sup>+</sup>  $v=0$  J=3–2 emission line cannot completely be ruled out. These moment 0 maps are shown in Figure 12. For IRAS 08572+3915 and IRAS 20414–1651, we barely see possible sign of HCN  $v_2=1f$  J=3–2 emission at the position close to the continuum peak, but the detection significance is  $\sim 2\sigma$  in the moment 0 maps, partly because not all the HCN  $v_2=1f$  J=3–2 emission components can be used to create the moment 0 maps, due to the contamination from the nearby much brighter HCO<sup>+</sup>  $v=0$  J=3–2 emission line. We see no discernible signature of the HCN  $v_2=1f$  J=3–2 emission line in the remaining

LIRGs. There is no clear sign of the  $\text{HCO}^+$   $v_2=1f$   $J=3-2$  emission line in any of the observed galaxies.

The deconvolved, intrinsic emission sizes, estimated using the CASA task “imfit”, for spatially not-clearly resolved sources are shown in Table 7. The luminosities of the vibrational ground ( $v=0$ )  $\text{HCN}/\text{HCO}^+$   $J=3-2$  emission lines are provided in Table 8. Table 9 tabulates the luminosities of vibrationally excited ( $v_2=1f$ )  $\text{HCN}$   $J=3-2$  emission lines for sources with  $>3\sigma$  detection (IRAS 12112+0305 NE and IRAS 22491–1808).

Intensity-weighted mean velocity (moment 1) and intensity-weighted velocity dispersion (moment 2) maps for  $\text{HCN}/\text{HCO}^+$   $J=3-2$  ( $v=0$ ) emission lines are shown in Figure 13. The similar emission morphology and dynamics in moment 0, 1, and 2 maps between  $\text{HCN}$   $J=3-2$  and  $\text{HCO}^+$   $J=3-2$  support our previous view (§1) that these emission lines originate in spatially similar regions within individual galaxies.

## 5. DISCUSSION

### 5.1. Vibrationally excited $\text{HCN}/\text{HCO}^+$ $J=3-2$ emission lines

#### 5.1.1. Luminous infrared galaxies

Because the energy levels of the vibrationally excited ( $v_2=1$ ) state for  $\text{HCN}$  ( $\sim 1030$  K) and  $\text{HCO}^+$  ( $\sim 1200$  K) are too high to be excited by collisions, infrared radiative pumping is thought to be necessary for vibrational excitation (Sakamoto et al. 2010). Due to a large amount of AGN-heated hot ( $>$  few 100 K) dust emission, the  $14\ \mu\text{m}$  luminosity in an AGN is significantly higher than that in a starburst for the same bolometric luminosity (Marshall et al. 2007; Vega et al. 2008). Thus,  $\text{HCN}$  vibrational excitation, through the absorption of infrared  $14\ \mu\text{m}$  photons, is expected to occur more efficiently in an AGN than in a starburst. In fact, the  $\text{HCN}$   $v_2=1f$  emission lines at  $J=3-2$  and/or  $J=4-3$  have recently been detected in gas/dust-rich LIRGs, which most likely, or plausibly, contain luminous AGNs, i.e., NGC 4418 (Sakamoto et al. 2010; Costagliola et al. 2015), IRAS 20551–4250 (Imanishi & Nakanishi 2013b; Imanishi et al. 2016a), Mrk 231 (Aalto et al. 2015a), and a few further LIRGs (Aalto et al. 2015b; Martin et al. 2016), demonstrating that this infrared radiative pumping mechanism actually works in some AGNs.

As the frequencies of  $\text{HCN}$   $v_2=1f$  and  $\text{HCO}^+$   $v=0$  are very close to each other at  $J=3-2$  and  $J=4-3$ , we can only clearly separate these lines for galaxies with small molecular line widths, such as NGC 4418 (Sakamoto et al. 2010), IRAS 20551–4250 (Imanishi & Nakanishi 2013b; Imanishi et al. 2016a), and IC 860 (Aalto et al. 2015b). For the majority of the other galaxies, these lines are blended. Even if the  $\text{HCN}$   $v_2=1f$   $J=3-2$  or  $J=4-3$  emission line is detected, it is recognized as a tail at the lower frequency side of the much brighter  $\text{HCO}^+$   $v=0$   $J=3-2$  or  $J=4-3$  emission line (Aalto et al. 2015a,b; Martin et al. 2016). The four ULIRGs, IRAS 08572+3915, IRAS 12112+0305 NE, IRAS 22491–1808, and IRAS 20414–1651, show these profiles. In particular, IRAS 12112+0305 NE and IRAS 22491–1808 can be categorized as sources that display detectable  $\text{HCN}$   $v_2=1f$   $J=3-2$  emission lines, given the  $>4\sigma$  detection in the moment 0 maps (Figure 12). For IRAS 08572+3915 and IRAS 22491–1808, similar  $\text{HCN}$   $v_2=1f$   $J=4-3$  emission tails

were not clearly seen in our ALMA Cycle 0 band 7 data (Imanishi & Nakanishi 2014); however, this is not surprising due to the improved performance of ALMA Cycle 2 data and intrinsically lower noise in band 6 with lower background emission, than in band 7. For IRAS 12112+0305 NE, a similar signature of the  $\text{HCN}$   $v_2=1f$   $J=4-3$  emission line at the lower frequency side of  $\text{HCO}^+$   $v=0$   $J=4-3$  was observed in our ALMA Cycle 2 data, despite a lower detection significance than  $J=3-2$ , while no significant emission tail is recognizable at the lower frequency side of  $\text{HCN}$   $v=0$   $J=4-3$  (Imanishi et al. 2016c).

While IRAS 08572+3915 is classified as a ULIRG possessing a luminous buried AGN in the infrared spectrum, IRAS 12112+0305 NE, IRAS 22491–1808, and IRAS 20414–1651 display no clear infrared buried AGN signatures. The signatures of the  $\text{HCN}$   $v_2=1f$   $J=3-2$  emission lines in our data suggest the presence of strong mid-infrared  $14\ \mu\text{m}$  continuum-emitting sources at the nuclei of these two LIRGs. The  $\text{HCN}$   $v_2=1f$   $J=3-2$  to infrared luminosity ratios are  $>7 \times 10^{-9}$  and  $\sim 9 \times 10^{-9}$  for IRAS 12112+0305 NE and IRAS 22491–1808, respectively. These ratios are several factors higher than that in the Galactic active ( $>10 L_\odot/M_\odot$ ) and luminous ( $>10^7 L_\odot$ ) star-forming region, W49A ( $<1.2 \times 10^{-9}$ ) (Nagy et al. 2015; Imanishi et al. 2016a). A luminous buried AGN is a plausible origin, although the possibility of a very compact extreme starburst cannot be completely ruled out (Aalto et al. 2015b). IRAS 12112+0305 NE and IRAS 22491–1808 are candidates that contain extremely deeply buried AGNs whose signatures are not seen in infrared  $5-35\ \mu\text{m}$  spectroscopic energy diagnostic methods due to dust extinction, but are revealed by our (sub)millimeter method because of the reduced effects of dust extinction (Draine & Lee 1984). If this is the case, (sub)millimeter observations could be an even more powerful method for detecting extremely deeply buried AGNs in LIRGs. IRAS 20414–1651 may also belong to this class, but higher quality data are needed to quantitatively better estimate the  $\text{HCN}$   $v_2=1f$   $J=3-2$  emission line luminosity.

The  $\text{HCO}^+$   $v_2=1f$   $J=3-2$  emission line is not clearly detected in any of the observed three optical Seyfert 1s and eleven LIRGs. Like  $\text{HCN}$ , infrared radiative pumping should also work for  $\text{HCO}^+$ , because  $\text{HCO}^+$  can be excited to the  $v_2=1$  level by absorbing infrared  $12\ \mu\text{m}$  photons (Davies et al. 1984; Kawaguchi et al. 1985). The infrared radiative pumping rate ( $P_{\text{IR}}$ ) is

$$P_{\text{IR}} \propto B_{v_2=0-1,vib} \times F_{\nu(\text{IR})} \times N_{v=0}, \quad (1)$$

where  $B_{v_2=0-1,vib}$  is the Einstein B coefficient from  $v=0$  to  $v_2=1$ ,  $F_{\nu(\text{IR})}$  is the infrared flux in [Jy] used for the infrared radiative pumping of  $\text{HCN}$  and  $\text{HCO}^+$ , and  $N_{v=0}$  is the column density at the  $v=0$  level. Here, the possible difference in population between  $\text{HCN}$  and  $\text{HCO}^+$  at rotational J-levels within  $v=0$  and  $v_2=1$  is not considered. As discussed in Imanishi et al. (2016a), the  $B_{v_2=0-1,vib}$  values are comparable within 10% between  $\text{HCN}$  and  $\text{HCO}^+$ . The  $F_{\nu(\text{IR})}$  values at  $12\ \mu\text{m}$  and  $14\ \mu\text{m}$  for the observed galaxies are derived from their Spitzer IRS low-resolution spectra (Brandl et al. 2006; Imanishi et al. 2007b; Wu et al. 2009). For sources with strong  $9.7\ \mu\text{m}$  silicate dust absorption features, power law continua determined from data points outside the broad  $9.7\ \mu\text{m}$  absorption features are utilized to estimate the intrinsic



infrared flux at 14  $\mu\text{m}$  and 12  $\mu\text{m}$ , which are used for the vibrational excitation to  $v_2=1$  of HCN and HCO<sup>+</sup>, respectively. In none of the galaxies was the intrinsic 14  $\mu\text{m}$  flux >30% larger than the intrinsic 12  $\mu\text{m}$  flux. Therefore, at least for the observed galaxies in this paper, the term  $B_{v_2=0-1,vib} \times F_{\nu(IR)}$  does not differ greatly between HCN and HCO<sup>+</sup> and thereby, under similar HCN and HCO<sup>+</sup> abundance, the infrared radiative pumping rate is comparable between HCN and HCO<sup>+</sup>. If the flux of the HCN  $v_2=1f$  J=3–2 emission line is significantly higher than that of HCO<sup>+</sup>  $v_2=1f$  J=3–2, HCN should then have a significantly higher column density, and thereby a higher abundance, than HCO<sup>+</sup>, unless excitation conditions at J=3 significantly differ between HCN and HCO<sup>+</sup> (Imanishi et al. 2016a).

The upper limit of the HCO<sup>+</sup>  $v_2=1f$  J=3–2 flux (Table 6) is only 10–20% lower than the flux of the HCN  $v_2=1f$  J=3–2 emission lines, even for IRAS 12112+0305 NE and IRAS 22491–1808. Thus, our only constraint is that the HCN abundance is at least comparable to HCO<sup>+</sup> or possibly higher.

### 5.1.2. Optical Seyfert galaxies

The original science goal of our ALMA Cycle 1 program was to detect the HCN  $v_2=1f$  J=3–2 emission lines from the AGN-dominated nuclear regions of the three Seyfert 1 galaxies, NGC 7469, I Zw 1, and IC 4329 A. In NGC 7469 and I Zw 1, the clear detection of the HCN and HCO<sup>+</sup> J=3–2 emission lines at  $v=0$  suggests that at least a modest amount of dense molecular gas is present at the nuclei. If the infrared radiative pumping mechanism is commonly working in AGNs, it is expected that a number of HCN and HCO<sup>+</sup>  $v_2=1f$  emission lines are produced. We did not detect HCN/HCO<sup>+</sup>  $v_2=1f$  J=3–2 emission lines in these AGN-dominated Seyfert 1 nuclei, and this requires some quantitative consideration. For the NGC 7469 nucleus, the HCN  $v_2=1f$  J=4–3 emission line was also undetected by ALMA observations (Izumi et al. 2015).

For the non-detected  $v_2=1f$  J=3–2 emission lines of HCN and HCO<sup>+</sup>, we use the  $3\sigma$  upper limits from the moment 0 maps tabulated in Table 6 for our discussion. As there is no existing report for the detection of the HCO<sup>+</sup>  $v_2=1f$  J=3–2 emission line in external galaxies, we focus here on the HCN  $v_2=1f$  J=3–2 line. The observed  $v_2=1f$  to  $v=0$  flux ratios at J=3–2 for HCN are <0.02 and <0.04 for NGC 7469 and I Zw 1 nuclei, respectively. For LIRGs with detected HCN  $v_2=1f$  emission lines, the observed HCN  $v_2=1f$  to  $v=0$  flux ratios at J=3–2 or J=4–3 are  $\sim 0.04$  in IRAS 20551–4250 and Mrk 231 (Imanishi & Nakanishi 2013b; Aalto et al. 2015a; Imanishi et al. 2016a), and 0.1–0.2 for the other sources (Sakamoto et al. 2010; Aalto et al. 2015b; Martin et al. 2016). The observed ratios in NGC 7469 (<0.02) and I Zw 1 (<0.04) are lower than these ratios.

We consider that a plausible scenario for the non-detection of the HCN  $v_2=1f$  J=3–2 emission line in NGC 7469 and I Zw 1 is the small line opacity of the HCN  $v=0$  J=3–2 emission. Thus far, the HCN  $v_2=1f$  J=3–2 or J=4–3 emission lines have been detected in LIRGs with buried AGNs whose signatures are unclear in the optical spectroscopic classification, except for Mrk 231 (Sakamoto et al. 2010; Imanishi & Nakanishi 2013b; Aalto et al. 2015a,b; Martin et al. 2016). Although Mrk

231 is classified optically as a Seyfert 1 galaxy due to the detection of broad optical emission lines (Veilleux et al. 1999; Yuan et al. 2010), the AGN emission in Mrk 231 is estimated to be highly obscured in infrared and X-ray data (Armus et al. 2007; Teng et al. 2014). It is likely that Mrk 231 is not a bona fide unobscured Seyfert 1 galaxy, but rather an obscured AGN.

For the obscured AGN-hosting LIRGs with detectable HCN  $v_2=1f$  emission lines, significant flux attenuation by line opacity of the HCN  $v=0$  emission is indicated (Sakamoto et al. 2010; Aalto et al. 2015a,b; Imanishi et al. 2016a; Martin et al. 2016). For NGC 4418, IRAS 20551–4250, and Mrk 231, the line-opacity-corrected intrinsic HCN  $v_2=1f$  to  $v=0$  flux ratios are quantitatively estimated to be  $\sim 0.01$  (Sakamoto et al. 2010; Aalto et al. 2015a; Imanishi et al. 2016a). These ratios are smaller than the upper limits at the NGC 7469 and I Zw 1 nuclei. NGC 7469 and I Zw 1 are classified optically as Seyfert 1 (= unobscured AGNs); thus, the direction along our line of sight in front of the AGN is at least clear of gas and dust. It is likely that molecular gas and dust are present in the close vicinity of the AGNs in the direction perpendicular to our sightline. If the ratio of rotational to random velocity of molecular gas does not differ greatly between unobscured optical Seyfert 1 AGNs and buried AGNs in LIRGs, the column density ratio along the maximum and minimum column density directions is not dissimilar. The presence of a transparent direction suggests that the total amount of nuclear molecular gas in unobscured AGNs is smaller than buried AGNs in LIRGs (Imanishi et al. 2007b, 2010). Thus, the flux attenuation of the HCN and HCO<sup>+</sup>  $v=0$  emission by line opacity is also expected to be smaller in unobscured AGNs. Izumi et al. (2015) estimated the line opacity for the HCN  $v=0$  J=4–3 emission to be <3.5 for the NGC 7469 nucleus. Even if unobscured AGNs and buried AGNs show intrinsically similar HCN  $v_2=1f$  to  $v=0$  flux ratios, the *observed* HCN  $v_2=1f$  to  $v=0$  flux ratios in buried AGNs can become larger due to higher HCN  $v=0$  flux attenuation. The upper limits of the observed HCN  $v_2=1f$  to  $v=0$  flux ratios at J=3–2 at the NGC 7469 and I Zw 1 nuclei are still consistent with the scenario that the efficiency of infrared radiative pumping in these unobscured-AGN-dominant nuclei is as high as that of buried AGNs with detected HCN  $v_2=1f$  emission lines. If this scenario is indeed the case, then HCN  $v_2=1f$  J=3–2 emission lines should be detected from the nuclei of NGC 7469 and I Zw 1 in data with a factor of 5–10 better sensitivity, even in the case that the line opacity correction of HCN  $v=0$  J=3–2 emission is negligible. Future higher sensitivity observations and line opacity estimates for the HCN  $v=0$  J=3–2 emission line will help to quantify how infrared radiative pumping works in various types of AGNs, including unobscured AGNs in optical Seyfert 1 galaxies and buried AGNs in LIRGs.

## 5.2. HCN to HCO<sup>+</sup> J=3–2 flux ratios

### 5.2.1. Observed ratios

The HCN-to-HCO<sup>+</sup> J=3–2 flux ratios at individual positions in individual galaxies are displayed in Figure 14. The NGC 7469 nucleus and I Zw 1 are classified as Seyfert 1s. In NGC 7469, SB1, SB2, SB3, and the SB ring (0'8–2'5 annular region) are taken

to be starburst-dominated. For NGC 1614, all regions are regarded as starburst-dominated. Among the other LIRGs, IRAS 08572+3915, The Superantennae, IRAS 12127-1412, IRAS 15250+3609, PKS 1345+12, and IRAS 06035-7102 are categorized as obscured AGNs, based on infrared spectroscopic energy diagnostic methods (§2). IRAS 12112+0305 NE and IRAS 22491-1808 are now classified as infrared-elusive, but (sub)millimeter-detectable, extremely deeply buried AGN candidates (§5.1.1). We tentatively include IRAS 20414-1651 in this category as well, because its spectrum in Figure 10 shows a more clearly discernible HCN  $v_2=1$  J=3-2 emission signature at the lower frequency part of the bright HCO<sup>+</sup>  $v=0$  J=3-2 emission than other ULIRGs (IRAS 12112+0305 SW, IRAS 12127-1412, PKS 1345+12, IRAS 06035-7102, IRAS 13509+0442). IRAS 12112+0305 SW and IRAS 13509+0442 show no AGN signature in either infrared or our new ALMA (sub)millimeter data. Our ALMA Cycle 2 results of the buried-AGN-hosting ULIRG IRAS 20551-4250 (Imanishi et al. 2016a), and multiple AGN-dominated nuclear regions of the optical Seyfert 2 galaxy, NGC 1068 (Imanishi et al. 2016b), are also plotted. In addition to these ALMA data, HCN J=3-2 and HCO<sup>+</sup> J=3-2 simultaneous observational data for NGC 4418 (Sakamoto et al. 2010) and NGC 1097 (Hsieh et al. 2012) taken with Submillimeter Array (SMA), and those for Mrk 231 (Aalto et al. 2015a) obtained with IRAM Plateau de Bure Interferometer (PdBI), are added, by classifying NGC 4418, the NGC 1097 nucleus, the NGC 1097 starburst ring, and Mrk 231 as a buried AGN, Seyfert 1, starburst, and an obscured AGN, respectively.

In Figure 14, we see a clear trend for AGNs, including infrared-elusive buried AGN candidates, to show elevated HCN-to-HCO<sup>+</sup> J=3-2 flux ratios, compared with starburst regions. Multiple starburst regions in NGC 7469 and NGC 1614, and other starburst galaxies (IRAS 12112+0305 SW, IRAS 13509+0442, and NGC 1097 off-nuclear starburst) consistently show low HCN-to-HCO<sup>+</sup> J=3-2 flux ratios. Hence, the low ratios are interpreted to be a general property of starbursts, rather than a specific property of a particular starburst region. The excess of the flux ratios in AGN-dominant nuclei in optical Seyferts and LIRGs with luminous obscured AGN signatures, compared with starbursts, is taken to be a robust result.

A similar HCN-to-HCO<sup>+</sup> flux enhancement in AGNs at J=1-0 has been proposed (Kohno 2005; Krips et al. 2008; Costagliola et al. 2011; Privon et al. 2015; Izumi et al. 2016), and was the basis for our ALMA observations. The enhanced HCN-to-HCO<sup>+</sup> flux ratios in AGNs appear to be common at different J-transition lines. As mentioned in §1, the HCN-to-HCO<sup>+</sup> flux comparison at J=3-2 is applicable to many interesting nearby LIRGs at  $z=0.06-0.3$  (Kim & Sanders 1998), whose HCN and HCO<sup>+</sup> observations at J=1-0 are not possible with ALMA.

### 5.2.2. Interpretation

The observed HCN-to-HCO<sup>+</sup> flux enhancement in AGNs, compared with starbursts, is naturally explained if (1) the HCN abundance is enhanced and/or (2) HCN excitation to J=3 is higher, as discussed by Imanishi et al. (2016a). Regarding scenario (1), it is clear that enhanced

molecular abundance generally produces a higher flux of that molecule in the optically thin regime. When line opacity becomes significant, the emission line flux does not increase proportionally to the increased abundance. However, adopting the widely accepted clumpy molecular gas model, where molecular clouds consist of randomly moving clumps with a small volume filling factor and the line opacity is primarily inside each clump, rather than different clumps in the foreground with different velocities (Solomon et al. 1987), an increasing HCN abundance will result in an increased HCN flux even in the optically thick regime, if each clump has a decreasing radial density profile (Imanishi et al. 2007a). This behavior differs from molecular clouds with a smooth gas distribution, where the observed molecular line flux saturates at some point when the opacity exceeds a certain threshold.

Regarding scenario (2), the critical density of HCN is a factor of  $\sim 5$  higher than HCO<sup>+</sup> at the same J-transition (Meijerink et al. 2007; Greve et al. 2009), under the same line opacity. For molecular gas with the same temperature and density, HCO<sup>+</sup> J=3-2 is more easily excited (to close to the thermalized condition) than HCN J=3-2. As the temperature of molecular gas in the close vicinity of an AGN can be higher than that in a starburst due to the AGN's higher emission surface brightness (§1), if HCO<sup>+</sup> J=3-2 is thermally excited and HCN J=3-2 is only sub-thermally excited in some starbursts, and if AGNs can excite HCN J=3-2 closer to the thermal condition, then the observed HCN-to-HCO<sup>+</sup> J=3-2 flux ratios in AGNs can show some excess, relative to those in starbursts, even under similar abundance. Among the galaxies observed in our ALMA programs, HCN J=1-0 flux data are available for IRAS 08572+3915 by pre-ALMA interferometric observations (Imanishi et al. 2007a) and for I Zw 1 by single-dish telescope observations (Evans et al. 2006). The HCN J=3-2 to J=1-0 flux ratios are  $\sim 1.1$  and  $\sim 2.2$  for IRAS 08572+3915 and I Zw 1, respectively. These values are substantially lower than the ratio of nine, which is expected from thermally excited optically thick molecular gas. The deviation is larger for IRAS 08572+3915 than I Zw 1. For IRAS 08572+3915, the J=4-3 to J=3-2 flux ratios are  $1.3 \pm 0.1$  for HCN and  $1.4 \pm 0.1$  for HCO<sup>+</sup> (Imanishi & Nakanishi 2014), both of which are lower than the 1.8 ( $=16/9$ ) expected for thermally excited optically thick gas. The significant sub-thermal excitation of IRAS 08572+3915 may be partly responsible for the relatively low observed HCN-to-HCO<sup>+</sup> J=3-2 flux ratio, compared with other AGNs (Figure 14).

It has been argued that an infrared radiative pumping mechanism can enhance the observed HCN  $v=0$  J=3-2 flux (Carroll & Goldsmith 1981; Aalto et al. 1995; Rangwala et al. 2011). Although this is true, such infrared radiative pumping should also work for HCO<sup>+</sup> (§1). As described in §5.1.1 and Imanishi et al. (2016a), under the same abundance, the rate of infrared radiative pumping to the  $v_2=1$  level does not differ a great deal between HCN and HCO<sup>+</sup> for the observed galaxies. Even though this infrared radiative pumping may work more efficiently in AGNs than in starbursts and increase the *absolute fluxes* of HCN and HCO<sup>+</sup>  $v=0$  J=3-2 emission lines compared with collisional excitation alone, it is not clear whether this may be largely responsible for the elevated HCN-to-HCO<sup>+</sup>  $v=0$  J=3-2 *flux ratios* in AGNs.

### 5.2.3. Line opacity

If HCN abundance enhancement is (at least partly) responsible for the elevated HCN-to-HCO<sup>+</sup> J=3–2 flux ratios in AGNs, the HCN line opacity could be higher than HCO<sup>+</sup>. Even though some AGNs show high observed HCN-to-HCO<sup>+</sup> flux ratios, other AGNs may not, due to higher HCN flux attenuation than HCO<sup>+</sup> by line opacity. Thus, the selection of AGN-important galaxies, based on the observed high HCN-to-HCO<sup>+</sup> flux ratios, may be incomplete and miss some fraction of AGNs unless HCN line opacity is properly corrected for.

In the widely accepted clumpy molecular gas model (Solomon et al. 1987) mentioned in §5.2.2, the opacity in a molecular cloud mostly comes from each clump. If the properties of each clump inside a molecular cloud are assumed to be uniform (Solomon et al. 1987), the observed molecular line flux from a molecular cloud is attenuated without significantly changing the observed velocity profiles. An effective way to estimate the HCN line opacity is the comparison of molecular isotopologues such HCN and H<sup>13</sup>CN, assuming a certain intrinsic <sup>12</sup>C-to-<sup>13</sup>C abundance ratio. The H<sup>13</sup>CN J=3–2 emission line was detected for the AGN-hosting LIRG IRAS 20551–4250, and it was estimated that line opacity correction causes the *intrinsic* HCN-to-HCO<sup>+</sup> J=3–2 flux ratio to be substantially larger than the *observed* flux ratio (Imanishi et al. 2016a). Among obscured-AGN-classified LIRGs, PKS 1345+12 and IRAS 06035–7102 also show not-as-high observed HCN-to-HCO<sup>+</sup> J=3–2 flux ratios in Figure 14. It is not clear at this stage whether the *intrinsic* HCN-to-HCO<sup>+</sup> J=3–2 flux ratios are similarly non-high or higher than the observed ratios for these two sources. Line opacity correction is definitely required to refine the AGN selection based on the HCN-to-HCO<sup>+</sup> J=3–2 flux ratios.

In the nuclei of some LIRGs, the concentration of molecular gas could be extreme, and so the volume filling factor of molecular gas clumps in molecular clouds could be large. The molecular gas geometry may be better approximated by a spatially smooth distribution (Downes et al. 1993; Scoville et al. 2015) rather than the clumpy structure. In this case, double-peaked molecular emission line profiles could be produced through self-absorption by foreground molecular gas, which works preferentially for the most abundant central velocity component (Aalto et al. 2015b). IRAS 12112+035 NE and IRAS 20414–1651 display such double-peaked emission line profiles for HCN J=3–2 and HCO<sup>+</sup> J=3–2 (Figures 5 and 9). For IRAS 12112+0305 NE, a similar profile is also evident at J=4–3 of HCN and HCO<sup>+</sup>, albeit at lower S/N ratios (Imanishi et al. 2016c). The origin of this double-peaked line profile could be (1) self-absorption and/or (2) emission being dominated by molecular gas in a prominent rotating disk.

For case (1), we tried single Gaussian fits using data not significantly affected by the central dips. These fits are shown as dotted curved lines in the spectra of IRAS 12112+0305 NE and IRAS 20414–1651 in Figure 9. The estimated HCN J=3–2 and HCO<sup>+</sup> J=3–2 emission line fluxes, based on the single Gaussian component fits, are included in Tables 4 and 5, respectively. For IRAS 12112+0305 NE, the fluxes based on the two Gaussian component fits of the double-peaked profiles are smaller

than those of the single Gaussian fits by  $\sim 25\%$  and  $\sim 50\%$  for HCN J=3–2 and HCO<sup>+</sup> J=3–2, respectively. If these flux differences are due to self-absorption by foreground molecular gas inside IRAS 12112+0305 NE, then it is estimated that the HCN J=3–2 and HCO<sup>+</sup> J=3–2 fluxes are attenuated by a factor of  $\sim 1.3$  and  $\sim 2$ , respectively. For IRAS 20414–1651, the fluxes based on the two Gaussian fits are smaller than those of the single Gaussian fits by a factor of 3–5 for both HCN J=3–2 and HCO<sup>+</sup> J=3–2.

For IRAS 12112+0305 NE and IRAS 20414–1651, H<sup>13</sup>CN J=3–2 data have been taken in ALMA Cycle 2 and been marginally detected in the moment 0 maps with  $0.28 \text{ [Jy beam}^{-1} \text{ km s}^{-1}]$  ( $3.2\sigma$ ) and  $0.20 \text{ [Jy beam}^{-1} \text{ km s}^{-1}]$  ( $3.3\sigma$ ) (Imanishi et al. 2016c), respectively, which correspond to the observed HCN-to-H<sup>13</sup>CN J=3–2 flux ratios with  $\sim 30$  and  $\sim 20$ . Assuming that the intrinsic <sup>12</sup>C/<sup>13</sup>C abundance ratios in these ULIRGs are 50–100 (Henkel & Mauersberger 1993; Henkel et al. 1993; Martin et al. 2010; Henkel et al. 2014) and that H<sup>13</sup>CN J=3–2 emission is optically thin, it is suggested that HCN J=3–2 emission is flux-attenuated with a factor of 1.5–3 and 2.5–5 for IRAS 12112+0305 NE and IRAS 20414–1651, respectively. Hence, if the central dips detected in the HCN J=3–2 and HCO<sup>+</sup> J=3–2 emission in IRAS 12112+0305 NE and IRAS 20414–1651 are due to self-absorption, the flux attenuation estimated from the comparison of Gaussian fittings is smaller than that derived from the HCN-to-H<sup>13</sup>CN J=3–2 flux comparison by a factor of 1–2 for IRAS 12112+0305 NE, while these two estimates look comparable within uncertainty for IRAS 20414–1651. However, despite limited signal-to-noise ratios, double-peaked emission line profiles with similar velocity peaks to the bright HCN J=3–2 and HCO<sup>+</sup> J=3–2 emission lines or top-flat type line profiles, rather than a centrally-peaked single Gaussian profile, are seen for the H<sup>13</sup>CN J=3–2 and CS J=7–6 emission lines in IRAS 12112+0305 NE and for H<sup>13</sup>CN J=3–2 in IRAS 20414–1651 (Imanishi et al. 2016c). Since the self-absorption effect is expected to be much smaller for the fainter H<sup>13</sup>CN J=3–2 emission line than HCN J=3–2 and HCO<sup>+</sup> J=3–2, it is not clear whether the observed double-peaked emission line profiles detected in IRAS 12112+0305 NE and IRAS 20414–1651 are explained solely by the self-absorption.

We next consider the second rotating disk scenario. In the intensity-weighted mean velocity (moment 1) maps of IRAS 12112+0305 NE and IRAS 22491–1651 in Figure 13, the signature of a rotational motion is marginally seen along the north-east to south-west direction, with a velocity difference of  $\sim 200\text{--}300 \text{ km s}^{-1}$  and  $\sim 400 \text{ km s}^{-1}$ , respectively. They are comparable to the observed velocity difference of the double peaks in Figure 9. Figure 15 shows the spectra within the beam size, at 3 pix ( $0''.3$ ) north and 3 pix ( $0''.3$ ) east (i.e.,  $\sim 0''.4$  north-east), and at 3 pix ( $0''.3$ ) south and 3 pix ( $0''.3$ ) west (i.e.,  $\sim 0''.4$  south-west), relative to the continuum peak positions, for IRAS 12112+0305 NE and IRAS 22491–1651. It is shown that the red (blue) component is relatively strong at the  $0''.4$  north-east (south-west) position, as is expected from the moment 1 maps of both objects. We interpret that compact rotating disks which are not clearly resolved with our ALMA beam size ( $0''.5\text{--}0''.8$ ) can also contribute significantly to the observed double-peaked emission line

profiles in IRAS 12112+0305 NE and IRAS 20414–1651.

In summary, AGNs tend to show elevated HCN-to-HCO<sup>+</sup> J=3–2 flux ratios, but some AGNs have non-high observed HCN-to-HCO<sup>+</sup> J=3–2 flux ratios. This could be explained by a larger flux attenuation caused by line opacity for HCN than HCO<sup>+</sup>, if the HCN abundance is higher than HCO<sup>+</sup>. In this respect, although we may be able to say that the elevated observed HCN-to-HCO<sup>+</sup> J=3–2 flux ratios are good AGN signatures, not all AGNs are selected based on the observed high HCN-to-HCO<sup>+</sup> J=3–2 flux ratios. Line opacity correction will make our method even more powerful and complete by reducing the number of missing AGNs. Clear double-peaked HCN J=3–2 and HCO<sup>+</sup> J=3–2 emission line profiles are seen in IRAS 12112+0305 NE and IRAS 20414–1651, which we interpret that rotating disks contribute significantly, in addition to a possible self-absorption effect.

### 5.3. Non-detection of molecular gas in IC 4329 A

The non-detection of the HCN J=3–2 and HCO<sup>+</sup> J=3–2 emission lines in IC 4329 A was unexpected. In this subsection, we briefly consider its possible causes. The three Seyfert 1 galaxies, NGC 7469, I Zw 1, and IC 4329 A, were selected because their nuclear infrared *L*-band (3–4  $\mu\text{m}$ ) emission is thought to be dominated by AGN-heated hot dust emission and their observed fluxes are high (§2). If dust and molecular gas spatially coexist in the nuclear region, strong collisionally excited molecular gas emission is also expected there. The observed nuclear *L*-band (3–4  $\mu\text{m}$ ) flux of IC 4329 A is about  $\sim 5$  times higher than those of NGC 7469 and I Zw 1 (Imanishi & Wada 2004; Imanishi et al. 2011a). At a first-order approximation, the HCN J=3–2 peak flux in IC 4329 A is expected to be higher than NGC 7469 and I Zw 1. However, the observed HCN J=3–2 emission peak is more than a factor of ten and five smaller than those of NGC 7469 and I Zw 1, respectively (Figure 4).

The nuclear HCN J=3–2 emission peak is roughly predicted from the nuclear infrared emission, based on their correlation (Imanishi & Nakanishi 2014). If we assume that the observed infrared luminosity in Table 1 originates from the nuclear region, then the expected HCN J=1–0 emission peaks are  $\sim 18$  mJy,  $\sim 3$  mJy, and  $\sim 4$  mJy for NGC 7469, I Zw 1, and IC 4329 A, respectively. If the HCN J=3–2 emission peak is nine times larger than that of HCN J=1–0, which is expected in thermally excited optically thick gas, then the expected HCN J=3–2 flux peaks are  $\sim 165$  mJy,  $\sim 25$  mJy, and  $\sim 35$  mJy, for NGC 7469, I Zw 1, and IC 4329 A, respectively. For NGC 7469, since it is estimated that about one third of the infrared luminosity originates from the nuclear region (Genzel et al. 1995), the expected HCN J=3–2 flux peak from the NGC 7469 nucleus is  $\sim 55$  mJy. For the NGC 7469 nucleus and I Zw 1, the observed HCN J=3–2 peak fluxes ( $\sim 25$  mJy and  $\sim 10$  mJy, respectively) agree with the above expected values within a factor of 2–3. However, the observed HCN J=3–2 peak flux of IC 4329 A is more than an order of magnitude smaller than the above expectation. Possible explanations include (1) infrared emission is spatially extended, rendering the fraction of the nuclear component small, and (2) HCN J=3–2 is only sub-thermally excited, and the HCN J=3–2 to J=1–0 flux ratio is thus considerably (more than an order of magnitude) smaller than nine. With regard to (1), as no

clear spatially extended off-nuclear emission is detected at infrared 10  $\mu\text{m}$  (Asmus et al. 2014), this seems unlikely. Regarding (2), because IC 4329 A contains a luminous X-ray-emitting AGN (Brightman & Nandra 2011; Brenneman et al. 2008), this also seems unlikely for nuclear molecular gas.

One scenario that could explain the weak HCN and HCO<sup>+</sup> J=3–2 emission in IC 4329 A is that the observed featureless nuclear infrared *L*-band (3–4  $\mu\text{m}$ ) continuum is not dominated by AGN-heated hot dust emission, but by other emission mechanisms such as synchrotron emission. Figure 16 displays the spectral energy distributions of NGC 7469, I Zw 1, and IC 4329 A in the infrared and radio wavelength ranges. The radio emission at  $< 20$  GHz is usually dominated by synchrotron emission. The *q*-value, defined as the decimal logarithm of the far-infrared (40–500  $\mu\text{m}$ ) to radio flux ratio (Condon et al. 1991), is often used to detect radio-loud AGNs, which show stronger synchrotron emission than the majority of radio-quiet AGNs. While the *q*-values of NGC 7469 and I Zw 1 (Table 10) are within the range of starburst-dominated galaxies and many radio-quiet AGNs ( $q \sim 2.3$ – $2.4$ ) (Condon et al. 1991; Barvainis et al. 1996; Crawford et al. 1996; Roy et al. 1998), that of IC 4329 A ( $q \sim 1.5$ ) (Table 10) is substantially lower, suggesting that IC 4329 A contains a radio-loud AGN. However, the observed infrared *L*-band (3–4  $\mu\text{m}$  or  $\sim 10^5$  GHz) flux is well above the extrapolation from the synchrotron emission component at  $< 20$  GHz. The strong infrared excess at 200– $10^5$  GHz in IC 4329 A, as well as NGC 7469 and I Zw 1, suggests that their infrared *L*-band (3–4  $\mu\text{m}$ ) emission is dominated by AGN-heated hot dust emission (Alonso-Herrero et al. 2011; Ichikawa et al. 2015), rather than synchrotron emission. Thus, this possibility also seems unlikely.

A second scenario is that the column density of the obscuring gas and dust surrounding the central AGN of IC 4329 A is very small. The infrared *L*-band (3–4  $\mu\text{m}$ ) continuum emission primarily arises from hot dust with  $> a$  few 100 K, located at the innermost region of the obscuring material, with limited contribution from outer cooler dust. On the other hand, collisionally excited HCN and HCO<sup>+</sup> J=3–2 emission lines can still be produced at the outer regions, whose gas/dust temperature is several 10 K to a few 100 K. If the obscuring gas/dust column density around an AGN is substantially smaller in IC 4329 A than in NGC 7469 and I Zw 1, then the smaller than expected HCN and HCO<sup>+</sup> J=3–2 emission line fluxes from the infrared *L*-band (3–4  $\mu\text{m}$ ) continuum flux could thus be explained. From the infrared spectral energy distribution, Ichikawa et al. (2015) estimated that the outer to innermost radius ratio of nuclear-obscuring dust in IC 4329 A is a factor of  $\sim 3$  smaller than NGC 7469, suggesting that this scenario is a possibility.

As a third possibility, if the molecular line widths of IC 4329 A are much larger than those of NGC 7469 and I Zw 1, the observed HCN/HCO<sup>+</sup> J=3–2 emission peak could be small, even if their fluxes are large. If IC 4329 A follows the similar HCN J=3–2 to nuclear infrared luminosity correlation and has similar molecular line widths to NGC 7469 and I Zw 1, the HCN J=3–2 flux peak is then expected to be  $> 15$  mJy. To explain the actual observed HCN J=3–2 flux peak with  $< 1.5$  mJy, molecular line widths  $> 10$  times larger than those of NGC

7469 and I Zw 1, i.e., at least a FWHM  $\sim 2000\text{--}3000$  km s<sup>-1</sup>, are required. This is more than a factor of 2 larger than the highly turbulent ongoing major merger ULIRG, The Superantennae (Mirabel et al. 1991). Because IC 4329 A is classified as a fairly settled spiral or S0 galaxy with a nuclear dust lane, but with no obvious highly disturbed morphology (Malkan et al. 1998), such an extremely large molecular line width seems unlikely. For IC 4329 A, there has been no molecular gas detection reported in the published literature, even for CO J=1–0 and J=2–1. Future ALMA high-sensitivity observations of bright CO emission at the IC 4329 A nucleus may help to test this scenario, if detection is realized.

In Figure 16, the observed flux increases with decreasing frequency from 10<sup>5</sup> GHz (3  $\mu$ m) to 10<sup>4</sup> GHz (30  $\mu$ m). However, the spectral energy distribution is flatter in IC 4329 A than NGC 7469 and I Zw 1, which means that the temperature of the dust thermal emission in this frequency range is higher in IC 4329 A. For given dust thermal radiation luminosity, if the dust temperature is higher, then the required dust mass can be smaller; consequently, the molecular mass becomes smaller, if dust and molecular gas spatially coexist in a similar manner. This could contribute to the observed weaker-than-expected molecular gas emission in IC 4329 A. The 2–10 keV X-ray luminosities of NGC 7469, I Zw 1, and IC 4329 A are  $\sim 2 \times 10^{43}$  ergs s<sup>-1</sup>,  $\sim 8 \times 10^{43}$  ergs s<sup>-1</sup>, and  $\sim 6 \times 10^{43}$  ergs s<sup>-1</sup>, respectively (Pinoncelli et al. 2005; Brightman & Nandra 2011; Brenneman et al. 2008)<sup>3</sup>. The high 2–10 keV X-ray luminosity of IC 4329 A indicates the presence of a luminous AGN. This luminous AGN, together with the estimated small outer-to-inner-radius ratio for nuclear dust, in IC 4329 A may be related to its higher dust effective temperature derived from the 10<sup>4</sup>–10<sup>5</sup> GHz (3–30  $\mu$ m) data.

In summary, the considerably smaller-than-expected HCN and HCO<sup>+</sup> J=3–2 emission line flux peak in IC 4329 A could be due to some combination of (1) a low column density of obscuring gas/dust around an AGN and/or (2) a small dust mass to infrared *L*-band (3–4  $\mu$ m) luminosity ratio, due to a high dust effective temperature. In either scenario, our (sub)millimeter energy diagnostic method is not sensitive to almost bare AGNs with a very limited amount of surrounding molecular gas, such as IC 4329A, because at least a detectable amount of molecular line emission is required for our method to be effective.

## 6. SUMMARY

We conducted HCN and HCO<sup>+</sup> J=3–2 observations in our ALMA Cycle 1, 2, and 3 programs, at both vibrational ground ( $v=0$ ) and vibrationally excited ( $v_2=1f$ ) levels, of three optical Seyfert 1 galactic nuclei, diagnosed to be energetically dominated by unobscured AGNs (NGC 7469, I Zw 1, and IC 4329 A) and eleven LIRGs with different levels of estimated energetic contribution by an AGN (IRAS 08572+3915, The Superantennae, IRAS 12112+0305, IRAS 22491–1808, NGC 1614, IRAS 12127–1412, IRAS 15250+3609, PKS 1345+12, IRAS 06035–7102, IRAS 13509+0442, and

IRAS 20414–1651). Among the LIRGs, NGC 1614 is dominated by starburst activity; IRAS 08572+3915, The Superantennae, IRAS 12127–1412, IRAS 15250+3609, PKS 1345+12, and IRAS 06035–7102 show infrared signatures of luminous obscured AGNs; and IRAS 12112+0305, IRAS 22491–1808, IRAS 13509+0442, and IRAS 20414–1651 display no obvious AGN signatures in the infrared. Our primary scientific goals were to investigate (1) if enhanced HCN-to-HCO<sup>+</sup> flux ratios at J=3–2 are found in AGNs, compared to starburst-dominated regions, as previously seen at J=1–0 and J=4–3, and (2) if vibrationally excited  $v_2=1f$  J=3–2 emission lines of HCN and HCO<sup>+</sup> are detected in AGNs, as HCN  $v_2=1f$  emission lines had been detected in several obscured AGNs. We found the following main results:

1. HCN and HCO<sup>+</sup> J=3–2 emission lines at  $v=0$  were clearly detected in all observed primary galactic nuclei, except for IC 4329 A. In NGC 7469, these emission lines were also clearly detected at three distinct starburst ring regions in the host galaxy. The spatially extended HCN J=3–2 and HCO<sup>+</sup> J=3–2 emission was also detected in the starburst-dominated LIRG, NGC 1614. In IRAS 12112+0305, the emission lines were detected in both the brighter main NE nucleus and fainter secondary SW nucleus.
2. The HCO<sup>+</sup> J=3–2 emission lines of IRAS 12112+0305 NE and IRAS 22491–1808 showed significant lower frequency tails, which we interpret to be due to the contribution from vibrationally excited ( $v_2=1f$ ) HCN J=3–2 emission lines. In the moment 0 maps, the HCN  $v_2=1f$  J=3–2 emission lines were detected with  $>4\sigma$  in both objects. The vibrational excitation of HCN is believed to originate in infrared radiative pumping, by absorbing infrared 14  $\mu$ m photons. Because for given bolometric luminosity, an AGN can produce much stronger infrared 14  $\mu$ m photons than a starburst, an AGN is a plausible origin for the infrared 14  $\mu$ m continuum-emitting source, even though a very compact extreme starburst cannot be completely ruled out. If the AGN scenario is the case, IRAS 12112+0305 NE and IRAS 22491–1808 may contain extremely deeply buried AGNs whose signatures were not seen in previous infrared spectroscopic energy diagnostic methods, but were first detected in our ALMA (sub)millimeter data.
3. The signature of a similar lower frequency tail was recognizable for the HCO<sup>+</sup> J=3–2 emission line of IRAS 08572+3915 and IRAS 20414–1651, but its detection significance in the moment 0 maps is lower than the above two LIRGs. IRAS 15250+3609 displays an emission sub-peak at close to the expected frequency of the HCN  $v_2=1f$  J=3–2 emission line, but it seems more likely that outflow origin HCO<sup>+</sup>  $v=0$  J=3–2 emission is largely contributing to this sub-peak. The remaining LIRGs with infrared-obscured AGN signatures, The Superantennae, IRAS 12127–1412, PKS 1345+12 and IRAS 06035–7102, and the starburst-classified LIRGs, NGC 1614, IRAS 12112+0305 SW, and IRAS 13509–0442, show no discernible signature of

<sup>3</sup> For these Seyfert 1 galaxies, absorption-corrected and -uncorrected 2–10 keV X-ray luminosities are comparable, due to the estimated low X-ray-absorbing hydrogen column density ( $N_H$ ).

the vibrationally excited HCN  $v_2=1f$   $J=3-2$  emission line.

4. Vibrationally excited HCN  $v_2=1f$   $J=3-2$  emission lines were not clearly seen in the two unobscured AGN-dominated Seyfert 1 nuclei, NGC 7469 and I Zw 1, despite our original expectation for the detection. The upper limits of the HCN  $v_2=1f$  to  $v=0$   $J=3-2$  flux ratios were lower than the observed ratios in several LIRGs with detected HCN  $v_2=1f$   $J=3-2$  emission lines. However, when the intrinsic ratios after line opacity correction for HCN  $v=0$   $J=3-2$  emission were derived in these LIRGs, the upper limits in NGC 7469 and I Zw 1 were still larger than the intrinsic ratios. We interpret that the line opacity and flux attenuation of HCN  $v=0$  emission lines are relatively small in optical Seyfert 1 AGNs, compared with deeply buried AGNs in LIRGs. Currently, we do not see any evidence that the infrared radiative pumping efficiency is different between these two types of AGNs.
5. The vibrationally excited  $\text{HCO}^+$   $v_2=1f$   $J=3-2$  emission lines were not recognizable in any of the observed galactic nuclei.
6. We identified that galaxies that do (or may) contain AGNs tend to display higher HCN-to- $\text{HCO}^+$   $J=3-2$  flux ratios than starburst regions, as previously argued at  $J=1-0$  and  $J=4-3$ . However, a small fraction of AGN-classified sources do not necessarily show very high observed HCN-to- $\text{HCO}^+$   $J=3-2$  flux ratios. Line-opacity-corrected intrinsic flux ratios are needed for all sources to refine the AGN selection in this method.
7. IRAS 15250+3609 showed a significant dip at the higher frequency (blueshifted) side of the  $\text{HCO}^+$   $J=3-2$  emission line and a sub-emission-peak at the lower frequency (redshifted) side of the  $\text{HCO}^+$   $J=3-2$  emission line. These features are interpreted to be due to the P Cygni profile by outflow activity of  $\text{HCO}^+$ .
8. In the continuum map of IRAS 13509+0442 at  $\sim 235$  GHz, a source even brighter than IRAS 13509+0442 was detected at  $\sim 1''$  eastern and 8–9'' northern side. No obvious optical counterpart was identified in the SDSS. No emission lines were seen

in our ALMA spectra. The nature of this source is still enigmatic.

We thank Dr. K. Saigo, Y. Ao, and A. Kawamura for their support regarding analysis of the ALMA data, and K. Sakamoto for useful discussions. We are grateful to the anonymous referee for his/her constructive comment which has helped a lot to improve the clarity of the descriptions of this manuscript. M.I. was supported by JSPS KAKENHI Grant Number 23540273, 15K05030 and the ALMA Japan Research Grant of the NAOJ Chile Observatory, NAOJ-ALMA-0001, 0023, 0072. T.I. is thankful for the fellowship received from the Japan Society for the Promotion of Science (JSPS). This paper makes use of the following ALMA data: ADS/JAO.ALMA#2012.1.00034.S, 2013.1.00032.S, 2013.1.00188.S, and 2015.1.00027.S. ALMA is a partnership of ESO (representing its member states), NSF (USA) and NINS (Japan), together with NRC (Canada), NSC and ASIAA (Taiwan), and KASI (Republic of Korea), in cooperation with the Republic of Chile. The Joint ALMA Observatory is operated by ESO, AUI/NRAO, and NAOJ. This research has made use of NASA's Astrophysics Data System and the NASA/IPAC Extragalactic Database (NED) which is operated by the Jet Propulsion Laboratory, California Institute of Technology, under contract with the National Aeronautics and Space Administration. This research has also made use of Sloan Digital Sky Survey (SDSS) data. Funding for the Sloan Digital Sky Survey (SDSS) has been provided by the Alfred P. Sloan Foundation, the Participating Institutions, the National Aeronautics and Space Administration, the National Science Foundation, the U.S. Department of Energy, the Japanese Monbukagakusho, and the Max Planck Society. The SDSS Web site is <http://www.sdss.org/>. The SDSS is managed by the Astrophysical Research Consortium (ARC) for the Participating Institutions. The Participating Institutions are The University of Chicago, Fermilab, the Institute for Advanced Study, the Japan Participation Group, The Johns Hopkins University, Los Alamos National Laboratory, the Max-Planck-Institute for Astronomy (MPIA), the Max-Planck-Institute for Astrophysics (MPA), New Mexico State University, University of Pittsburgh, Princeton University, the United States Naval Observatory, and the University of Washington.

#### REFERENCES

- Aalto, S., Booth, R. S., Black, J. H., & Johansson, L. E. B. 1995, *A&A*, 300, 369
- Aalto, S., Garcia-Burillo, S., Muller, S., et al. 2015a, *A&A*, 574, A85
- Aalto, S., Costagliola, S., Martin F., et al. 2015b, *A&A*, 584, A42
- Alonso-Herrero, A., Engelbracht, C. W., Rieke, M. J., Rieke, G. H., & Quillen, A. C. 2001, *ApJ*, 546, 952
- Alonso-Herrero, A., Ramos Almeida, C., Mason, R., et al. 2011, *ApJ*, 736, Engelbracht, C. W., Rieke, M. J., Rieke,
- Armus, L., Charmandaris, V., Bernard-Salas, J., et al. 2007, *ApJ*, 656, 148
- Asmus, D., Honig, S. F., Gandhi, P., Smette, A., & Duschl, W. J. 2014, *MNRAS*, 439, 1648
- Barvainis, R., Lonsdale, C., & Antonucci, R. 1996, *AJ*, 111, 1431
- Braito, V., Franceschini, A., Della Ceca, R. et al. 2003, *A&A*, 398, 107
- Braito, V., Reeves, J. N., Della Ceca, R. et al., 2009, *A&A*, 504, 53
- Brandl, B. R., Bernard-Salas, J., Spoon, H. W. W. et al. 2006, *ApJ*, 653, 1129
- Brenneman, L. W., Madejski, G., Fuerst, F., et al. 2014, *ApJ*, 788, 61
- Brightman, M., & Nandra, K. 2011, *MNRAS*, 414, 3084
- Burtscher, L., Meisenheimer, K., Tristram, K. R. W. et al. 2013, *A&A*, 558, 149
- Carrol, T. J., & Goldsmith, P. F., 1981, *ApJ*, 245, 891
- Condon, J. J., Anderson, M. L., & Helou, G. 1991, *ApJ*, 376, 95
- Condon, J. J., Cotton, W. D., Greisen, E. W. et al. 1998, *AJ*, 115, 1693
- Costagliola, F., Aalto, S., Rodriguez, M. I., et al. 2011, *A&A*, 528, A30
- Costagliola, F., Sakamoto, K., Muller, S., et al. 2015, *A&A*, 582, 91
- Crawford, T., Marr, J., Partridge, B., & Strauss, M. A. 1996, *ApJ*, 460, 225

- Dartois, E., & Munoz-Caro, G. M. 2007, *A&A*, 476, 1235
- Davies, P. B., Hamilton, P. A., & Rothwell, W. J. 1984, *J. Chem. Phys.*, 81, 1598
- Davies, R. I., Tacconi, L. J., & Genzel, R. 2004, *ApJ*, 602, 148
- Diaz-Santos, T., Alonso-Herrero, A., Colina, L., Packham, C., Radomski, J. T., & Telesco, C. M. 2008, *ApJ*, 685, 211
- Diaz-Santos, T., Alonso-Herrero, A., Colina, L., Ryder, S. D., & Knapen, J. H. 2007, *ApJ*, 661, 149
- Downes, D., Solomon, P. M., & Radford, S. J. E. 1993, *ApJ*, 414, L13
- Drake, C. L., McGregor, P. J., Dopita, M. A., & van Breugel, W. J. M. 2003, *AJ*, 126, 2237
- Draine, B. T., & Lee, H. M. 1984, *ApJ*, 285, 89
- Duc, P. -A., Mirabel, I. F., & Maza, J. 1997, *A&AS*, 124, 533
- Dudley, C. C., & Wynn-Williams, C. G. 1997, *ApJ*, 488, 720
- Esquej, P., Alonso-Herrero, A., Gonzalez-Martin, O., et al. 2014, *ApJ*, 780, 86
- Evans, A. S., Kim, D. C., Mazzarella, J. M. et al. 1999, *ApJ*, 521, 107L
- Evans, A. S., Mazzarella, J. M., Surace, J. A., & Sanders, D. B. 2002, *ApJ*, 580, 749
- Evans, A. S., Solomon, P. M., Tacconi, L. J., Vavilkin, T., & Downes, D. 2006, *AJ*, 132, 2398
- Farrah, D., Connolly, B., Connolly, N. et al. 2009, *ApJ*, 700, 396
- Ferrarese, L., & Merritt, D. 2000, *ApJ*, 539, L9
- Galliano, E., Alloin, D., Pantin, E., Lagage, P. O., & Marco, 2005, *A&A*, 438, 803
- Garcia-Burillo, S., Gracia-Carpio, J., Guelin, M., et al. 2006, *ApJ*, 645, L17
- Garcia-Burillo, S., Combes, F., Usero, A., et al. 2014, *A&A*, 567, 125
- Genzel, R., Weitzel, L., Tacconi-Garman, L. E., et al. 1995, *ApJ*, 444, 129
- Genzel, R., Lutz, D., Sturm, E. et al. 1998, *ApJ*, 498, 579
- Greve, T. R., Papadopoulos, P. P., Gao, Y., & Radford, S. J. E., 2009, *ApJ*, 692, 1432
- Gultekin, K., Richstone, D. O., Gebhardt, K., et al. 2009, *ApJ*, 698, 198
- Haan, S., Armus, L., Laine, S. et al. 2011, *ApJS*, 197, 27
- Harada, N., Herbst, E., & Wakelam, V. 2010, *ApJ*, 721, 1570
- Harada, N., Thompson, T. A., & Herbst, V. 2013, *ApJ*, 765, 108
- Henkel, C., Asiri, H., Ao, Y., et al. 2014, *A&A*, 565, A3
- Henkel, C., & Mauersberger, R. 1993, *A&A*, 274, 730
- Henkel, C., Mauersberger, R., Wiklind, T., et al. 1993, *A&A*, 268, L17
- Hildebrand, R. H. 1983, *QJRAS*, 24, 267
- Honig, S. F., Kishimoto, M., Gandhi, P. et al. 2010, *A&A*, 515, 23
- Hopkins, P. F., Hernquist, L., Cox, T. J., et al. 2005, *ApJ*, 630, 705
- Hopkins, P. F., Hernquist, L., Cox, T. J., et al. 2006, *ApJS*, 163, 1
- Hsieh, P.-Y., Ho, P. T. P., Kohno, K., Hwang, C.-Y., Matsushita, S. 2012, *ApJ*, 747, 90
- Huchra, J., & Burg, R. 1992, *ApJ*, 393, 90
- Ichikawa, K., Packham, C., Ramos Almeida, C., et al. 2015, *ApJ*, 803, 57
- Imanishi, M. 2002, *ApJ*, 569, 44
- Imanishi, M. 2003, *ApJ*, 599, 918
- Imanishi, M. 2006, *AJ*, 131, 2406
- Imanishi, M., & Dudley, C. C. 2000, *ApJ*, 545, 701
- Imanishi, M., Dudley, C. C., & Maloney, P. R. 2006a, *ApJ*, 637, 114
- Imanishi, M., Dudley, C. C., Maiolino, R., Maloney, P. R., Nakagawa, T., & Risaliti, G. 2007b, *ApJS*, 171, 72
- Imanishi, M., Ichikawa, K., Takeuchi, T., et al. 2011a, *PASJ*, 63, S447
- Imanishi, M., Imase, K., Oi, N., & Ichikawa, K. 2011b, *AJ*, 141, 156
- Imanishi, M., Nakagawa, T., Shirahata, M., Ohya, Y., & Onaka, T. 2010, *ApJ*, 721, 1233
- Imanishi, M., & Nakanishi, K. 2006, *PASJ*, 58, 813
- Imanishi, M., & Nakanishi, K. 2013a, *AJ*, 146, 47
- Imanishi, M., & Nakanishi, K. 2013b, *AJ*, 146, 91
- Imanishi, M., & Nakanishi, K. 2014, *AJ*, 148, 9
- Imanishi, M., & Nakanishi, K. et al. 2016c, in preparation
- Imanishi, M., Nakanishi, K., & Izumi, T. 2016b, *ApJL*, 822, L10
- Imanishi, M., Nakanishi, K., & Izumi, T. 2016a, *ApJ*, 825, 44
- Imanishi, M., Nakanishi, K., Kuno, N., & Kohno, K. 2004, *AJ*, 128, 2037
- Imanishi, M., Nakanishi, K., & Kohno, K. 2006b, *AJ*, 131, 2888
- Imanishi, M., Nakanishi, K., Tamura, Y., Oi, N., & Kohno, K. 2007a, *AJ*, 134, 2366
- Imanishi, M., Nakanishi, K., Tamura, Y., & Peng, C. -H. 2009, *AJ*, 137, 3581
- Imanishi, M., & Saito, Y. 2014, *ApJ*, 780, 106
- Imanishi, M., & Wada, K. 2004, *ApJ*, 617, 214
- Iono, D., Saito, T., Yun, M. S., et al. 2013, *PASJ*, 65, L7
- Izumi, T., Kohno, K., Aalto, S., et al. 2015, *ApJ*, 811, 39
- Izumi, T., Kohno, K., Aalto, S., et al. 2016, *ApJ*, 818, 42
- Jia, J., Ptak, A., Heckman, T. M., Braitto, V., & Reeves, J. 2012, *ApJ*, 759, 41
- Kawaguchi, K., Yamada, C., Saito, S., & Hirota, E., 1985, *J. Chem. Phys.*, 82, 1750
- Kewley, L. J., Heisler, C. A., Dopita, M. A., & Lumsden, S. 2001, *ApJS*, 132, 37
- Kim, D. -C., & Sanders, D. B., 1998, *ApJS*, 119, 41
- Kim, D. -C., Sanders, D. B., Veilleux, S., Mazzarella, J. M., & Soifer, B. T. 1995, 98, 129
- Kim, D. -C., Veilleux, S., & Sanders, D. B., 2002, *ApJS*, 143, 277
- Kohno, K. 2005, in *AIP Conf. Ser.* 783, *The Evolution of Starbursts*, ed. S. Hüttemeister, E. Manthey, D. Bomans, & K. Weis (New York: AIP), 203 (astro-ph/0508420)
- Komatsu, E., Dunkley, J., Nolte, M. R., et al. 2009, *ApJS*, 180, 330
- Krips, M., Neri, R., Garcia-Burillo, S., Martin, S., Combes, F., Gracia-Carpio, J., & Eckart, A. 2008, *ApJ*, 677, 262
- Lintott, C., & Viti, S. 2006, *ApJ*, 646, L37
- Ma, C., Arias, E. F., Eubanks, T. M. et al. 1998, *AJ*, 116, 516
- Magorrian, J., Tremaine, S., Richstone, D., et al. 1998, *ApJ*, 115, 2285
- Malkan, M. A., Gorjian, V., & Tam, R., 1998, *ApJS*, 117, 25
- Marco, O., & Alloin, D. 1998, *A&A*, 336, 823
- Marshall, J. A., Herter, T. L., Armus, L., et al. 2007, *ApJ*, 670, 129
- Martin, S., Aladro, R., Martin-Pintado, J., & Mauersberger, R. 2010, *A&A*, 522, A62
- Martin, S., Aalto, S., Sakamoto, K., et al. 2016, *A&A*, 590, A25
- McConnell, N. J. & Ma, C.-P. 2013, *ApJ*, 764, 184
- Meijerink, R., & Spaans, M. 2005, *A&A*, 436, 397
- Meijerink, R., Spaans, M., & Israel, F. P. 2007, *A&A*, 461, 793
- Miles, J. W., Houck, J. R., Hayward, T. L., & Ashby, M. L. N. 1996, *ApJ*, 465, 191
- Mirabel, I. F., Lutz, D., & Maza, J. 1991, *A&A*, 243, 367
- Moorwood, A. F. M. 1986, *A&A*, 166, 4
- Nagy, Z., van der Tak, F. F. S., Fuller, G. A., & Plume, R. 2015, *A&A*, 577, A127
- Nardini, E., Risaliti, G., Salvati, M., et al. 2008, *MNRAS*, 385, L130
- Nardini, E., Risaliti, G., Salvati, M., et al. 2009, *MNRAS*, 399, 1373
- Nardini, E., Risaliti, G., Watabe, Y., Salvati, M., & Sani, E. 2010, *MNRAS*, 405, 2505
- Orienti, M., & Prieto, M. A. 2010, *MNRAS*, 401, 2599
- Papadopoulos, P. P. et al. 2007, *ApJ*, 656, 792
- Pereira-Santaella, M., Colina, L., Alonso-Herrero, A. et al. 2015, *MNRAS*, 454, 3679
- Pinoncelli, E., Jimenez-Bailon, E., Guainazzi, M., et al. 2005, *A&A*, 432, 15
- Privon, G. C., Herrero-Illana, R., Evans, A. S., et al. 2015, *ApJ*, 814, 39
- Ranalli, P., Comastri, A., & Setti, G. 2003, *A&A*, 399, 39
- Rangwala, N., Maloney, P. R., Glenn, J., et al. 2011, *ApJ*, 743, 94
- Reunanen, J., Tacconi-Garman, L. E., & Ivanov, V. D. 2007, *MNRAS*, 382, 951
- Reunanen, J., Prieto, M. A., & Siebenmorgen, R. 2010, *MNRAS*, 402, 879
- Risaliti, G., Maiolino, R., Marconi, A. et al. 2003, *ApJ*, 595, L17
- Roche, P. F., Aitken, D. K., Smith, C. H., & Ward, M. J., 1991, *MNRAS*, 248, 606
- Rodriguez-Ardila, A., & Viegas, S. M. 2003, *MNRAS*, 340, L33
- Roy, A. L., Norris, R. P., Kesteven, M. J., Troup, E. R., & Reynolds, J. E. 1998, *MNRAS*, 301, 1019
- Rush, B., Malkan, M. A., & Spinoglio, L. 1993, *ApJS*, 89, 1
- Sakamoto, K., Aalto, S., Evans, A. S., Wiedner, M., & Wilner, D. 2010, *ApJ*, 725, L228
- Sakamoto, K., Aalto, S., Wilner, D. J., et al. 2009, *ApJ*, 700, L104
- Sanders, D. B., & Mirabel, I. F. 1996, *ARA&A*, 34, 749
- Schmidt, M., & Green, R. F. 1983, *ApJ*, 269, 352

- Scoville, N. Z., Evans, A. S., Thompson, R., et al. 2000, *AJ*, 119, 991
- Scoville, N., Sheth, K., Walter, F., et al. 2015, *ApJ*, 800, 70
- Shang, Z., Brotherton, M. S., Wills, B. J., et al. 2011, *ApJ*, 196, 2
- Soifer, B. T., Bock, J. J., Marsh, K., Neugebauer, G., Matthews, K., Egami, E., & Armus, L. 2003, *AJ*, 126, 143
- Soifer, B. T., Neugebauer, G., Matthews, K., et al. 2000, *AJ*, 119, 509
- Soifer, B. T., Sanders, D. B., Madore, B. F., et al. 1987, *ApJ*, 320, 238
- Soifer, B. T., Neugebauer, G., Matthews, K. et al. 2001, *AJ*, 122, 1213
- Solomon, P. M., Rivolo, A. R., Barrett, J., et al. 1987, *ApJ*, 319, 730
- Spoon, H. W. W., Keane, J. V., Tielens, A. G. G. M., Lutz, D., Moorwood, A. F. M., & Laurent, O. 2002, *A&A*, 385, 1022
- Spoon, H. W. W., Tielens, A. G. G. M., Armus, L., et al. 2006, *ApJ*, 638, 759
- Stierwalt, S., Armus, L., & Surace, J. A., et al. 2013, *ApJS*, 206, 1
- Strauss, M. A., Huchra, J. P., Davis, M., et al. 1992, *ApJS*, 83, 29
- Teng, S. H., Rigby, J. R., Stern, D. et al. 2015, *ApJ*, 814, 56
- Teng, S. H., Brandt, W. N., Harrison, F. A. et al., 2014, *ApJ*, 785, 19
- Teng, S. H., Veilleux, S., Anabuki, N., et al. 2009, *ApJ*, 691, 261
- White, S. D. M., & Rees, M. J. 1978, *MNRAS*, 183, 341
- Wilson, A. S., Helfer, T. T., Haniff, C. A., & Ward, M. J. 1991, *ApJ*, 381, 79
- Yamada, M., Wada, K., & Tomisaka, K. 2007, *ApJ*, 671, 73
- Vega, O., Clemens, M. S., Bressan, A., et al. 2008, *A&A*, 484, 631
- Veilleux, S., Kim, D. -C., & Sanders, D. B. 1999, *ApJ*, 522, 113
- Veilleux, S., Kim, D. -C., Sanders, D. B., Mazzarella, J. M., & Soifer, B. T. 1995, *ApJS*, 98, 171
- Veilleux, S., Melendez, M., Sturm, E., et al. 2013, *ApJ*, 776, 27
- Veilleux, S., Sanders, D. B., & Kim, D. -C. 1997, *ApJ*, 484, 92
- Veilleux, S., Rupke, D. S. N., Kim, D.-C., et al. 2009, *ApJS*, 182, 628
- Voit, G. M. 1992, *MNRAS*, 258, 841
- Wu, Y., Charmandaris, V., Huang, J., Spinoglio, L., & Tommasin, S. 2009, *ApJ*, 701, 658
- Yuan, T. -T., Kewley, L. J., & Sanders, D. B. 2010, *ApJ*, 709, 884
- Ziurys, L. M., & Turner, B. E. 1986, *ApJ*, 300, L19



TABLE 1  
BASIC PROPERTIES OF OBSERVED GALAXIES

Object	Redshift	Physical scale [kpc''']	f <sub>12</sub> [Jy]	f <sub>25</sub> [Jy]	f <sub>60</sub> [Jy]	f <sub>100</sub> [Jy]	log L <sub>IR</sub> [L <sub>⊙</sub> ]	Optical Class
(1)	(2)	(3)	(4)	(5)	(6)	(7)	(8)	(9)
NGC 7469	0.0164	0.33	1.35	5.79	25.87	34.90	11.6	Sy1 <sup>a</sup>
I Zw 1	0.0611	1.2	0.51	1.21	2.24	2.63	11.9	Sy1 <sup>b</sup>
IC 4329 A	0.0160	0.32	1.08	2.21	2.03	1.66	10.9	Sy1 <sup>c</sup>
IRAS 08572+3915	0.0580	1.1	0.32	1.70	7.43	4.59	12.1	LI <sup>d</sup> (Sy2 <sup>e</sup> )
Superantennae (IRAS 19254–7245)	0.0617	1.2	0.22	1.24	5.48	5.79	12.1	Sy2 <sup>f</sup>
IRAS 12112+0305	0.0730	1.4	0.12	0.51	8.50	9.98	12.3	LI <sup>d</sup> (Sy2 <sup>e</sup> )
IRAS 22491–1808	0.0776 <sup>A</sup> (0.076)	1.5	0.05	0.55	5.44	4.45	12.2	HII <sup>d,e</sup>
NGC 1614	0.0160	0.32	1.38	7.50	32.12	34.32	11.7	HII <sup>a,g</sup> (Cp <sup>e</sup> )
IRAS 12127–1412	0.1332 <sup>A</sup> (0.133)	2.3	<0.13	0.24	1.54	1.13	12.2	LI <sup>d</sup> (HII <sup>e</sup> )
IRAS 15250+3609	0.0552 <sup>A</sup> (0.054)	1.1	0.16	1.31	7.10	5.93	12.0	LI <sup>a</sup> (Cp <sup>e</sup> )
PKS 1345+12 (IRAS 13451+1232)	0.1215 <sup>A</sup> (0.122)	2.2	0.14	0.67	1.92	2.06	12.3	Sy2 <sup>d,e</sup>
IRAS 06035–7102	0.0795	1.5	0.12	0.57	5.13	5.65	12.2	LI <sup>h</sup>
IRAS 13509+0442	0.1364 <sup>A</sup> (0.136)	2.4	0.10	<0.23	1.56	2.53	12.3	HII <sup>d</sup> (Cp <sup>e</sup> )
IRAS 20414–1651	0.0870 <sup>A</sup> (0.086)	1.6	<0.65	0.35	4.36	5.25	12.3	HII <sup>d</sup> (Cp <sup>e</sup> )

NOTE. — Col.(1): Object name. The top three sources are optical Seyfert 1 galaxies. The next five and bottom six sources are LIRGs observed in ALMA Cycle 2 and Cycle 3, respectively. Col.(2): Redshift. Col.(3): Physical scale in [kpc arcsec<sup>-1</sup>]. Col.(4)–(7): f<sub>12</sub>, f<sub>25</sub>, f<sub>60</sub>, and f<sub>100</sub> are IRAS fluxes at 12 μm, 25 μm, 60 μm, and 100 μm, respectively, taken from the IRAS Faint Source Catalog (FSC). Col.(8): Decimal logarithm of infrared (8–1000 μm) luminosity in units of solar luminosity (L<sub>⊙</sub>), calculated with  $L_{\text{IR}} = 2.1 \times 10^{39} \times D(\text{Mpc})^2 \times (13.48 \times f_{12} + 5.16 \times f_{25} + 2.58 \times f_{60} + f_{100})$  [ergs s<sup>-1</sup>] (Sanders & Mirabel 1996). Col.(9): Optical spectroscopic classification. “Sy1”, “Sy2”, “LI”, “HII”, and “Cp” refer to Seyfert 1, Seyfert 2, LINER, HII-region, and starburst+AGN composite, respectively. <sup>a</sup>: Veilleux et al. (1995). <sup>b</sup>: Schmidt & Green (1983). <sup>c</sup>: Rush et al. (1993). <sup>d</sup>: Veilleux et al. (1999). <sup>e</sup>: Yuan et al. (2010). <sup>f</sup>: Mirabel et al. (1991). <sup>g</sup>: Kewley et al. (2001). <sup>h</sup>: Duc et al. (1997).

<sup>A</sup> The observed peak frequencies of the detected HCN J=3–2 and HCO<sup>+</sup> J=3–2 emission lines in our ALMA spectra are significantly offset from those expected from optically-derived redshifts (Soifer et al. 1987; Strauss et al. 1992; Kim et al. 1995; Kim & Sanders 1998; Veilleux et al. 1999). Our high quality ALMA molecular line data provide accurate redshifts with four effective digits, which are adopted in this paper. Optically-derived redshifts (Kim et al. 1995; Kim & Sanders 1998) are shown in parentheses.

TABLE 2  
LOG OF OUR ALMA OBSERVATIONS

Object	Date [UT]	Antenna Number	Baseline [m]	Integration [min]	Bandpass	Calibrator Flux	Phase
(1)	(2)	(3)	(4)	(5)	(6)	(7)	(8)
NGC 7469	2014 April 29	35	21–558	25	J2148+0657	Neptune	J2257+0743
	2014 May 3	31	17–532	25	J2148+0657	Neptune	J2257+0743
	2014 July 22	34	18–784	24	J2253+1608	J2232+117	J2253+1608
I Zw 1	2014 May 4	39	17–558	22	J2148+0657	Neptune	J0121+1149
	2014 May 4	39	17–558	22	J0006–0623	Neptune	J0121+1149
	2014 July 16	34	20–650	14	J0237+2848	J0238+166	J0121+1149
IC 4329 A	2014 April 10	32	21–484	27	J1107–4449	Pallas	J1342–2900
IRAS 08572+3915	2015 June 9	36	21–784	11	J0854+2006	Ganymede	J0927+3902
Superantennae	2015 May 18	37	21–555	10	J2056–4714	Ceres	J1933–6942
IRAS 12112+0305	2015 May 14	37	23–558	5	J1058+0133	Ganymede	J1229+0203
IRAS 22491–1808	2015 May 24	34	21–539	5	J2258–2758	Titan	J2056–4714
NGC 1614	2015 May 24	36	21–539	5	J0423–0120	Callisto	J0423–0120
IRAS 12127–1412	2016 March 3	41	15–396	29	J1256–0547	J1256–0547	J1215–1731
IRAS 15250+3609	2016 March 13	38	15–460	11	J1751+0939	Titan	J1453+2648
PKS 1345+12	2016 March 3	41	15–396	18	J1229+0203	Titan	J1415+1320
IRAS 06035–7102	2016 March 14	43	15–460	12	J0519–4546	J0519–4546	J0601–7036
IRAS 13509+0442	2016 March 3	39	15–396	24	J1256–0547	J1256–0547	J1359+0159
IRAS 20414–1651	2016 March 26	38	15–460	11	J1924–2914	Pallas	J2011–1546

NOTE. — Col.(1): Object name. Col.(2): Observing date in UT. The bottom six sources were observed in ALMA Cycle 3. Col.(3): Number of antennas used for observations. Col.(4): Baseline length in meters. Minimum and maximum baseline lengths are shown. Col.(5): Net on-source integration time in min. Cols.(6), (7), and (8): Bandpass, flux, and phase calibrator for the target source, respectively.

TABLE 3  
CONTINUUM EMISSION PROPERTIES

Object	Position	Frequency [GHz]	Flux [mJy beam <sup>-1</sup> ]	Peak Coordinate (RA,DEC)J2000	rms [mJy beam <sup>-1</sup> ]	Beam [" × " (°)]
(1)	(2)	(3)	(4)	(5)	(6)	(7)
NGC 7469	Nucleus	260.8–265.4	3.4 (33σ)	(23 03 15.62, +08 52 26.1)	0.10	0.57×0.52 (72°)
	SB1	260.8–265.4	1.2 (12σ)	(23 03 15.52, +08 52 25.1)	0.10	0.57×0.52 (72°)
	SB2	260.8–265.4	0.71 (7σ)	(23 03 15.69, +08 52 27.1)	0.10	0.57×0.52 (72°)
	SB3	260.8–265.4	0.86 (8σ)	(23 03 15.58, +08 52 27.4)	0.10	0.57×0.52 (72°)
I Zw 1	Nucleus	249.7–254.2	1.2 (21σ)	(00 53 34.94, +12 41 36.0)	0.057	0.67×0.60 (60°)
IC 4329 A	Nucleus	260.7–265.4	13.0 (69σ)	(13 49 19.26, −30 18 34.2)	0.19	0.95×0.53 (83°)
IRAS 08572+3915	Nucleus	250.4–254.9	2.5 (23σ)	(09 00 25.36, +39 03 53.9)	0.11	0.89×0.47 (−19°)
Superantennae	Nucleus	249.5–254.4	5.0 (29σ)	(19 31 21.41, −72 39 21.6)	0.17	0.87×0.61 (21°)
IRAS 12112+0305	NE	246.8–251.3	8.3 (46σ)	(12 13 46.06, +02 48 41.5)	0.18	0.73×0.55 (66°)
	SW	246.8–251.3	0.80 (4σ)	(12 13 45.94, +02 48 39.1)	0.19	0.73×0.55 (66°)
IRAS 22491–1808	Nucleus	246.1–250.7	4.7 (19σ)	(22 51 49.35, −17 52 24.2)	0.25	0.92×0.59 (67°)
NGC 1614	S-peak	260.8–265.5	2.6 (8σ)	(04 34 00.01, −08 34 45.7)	0.31	1.06×0.58 (−75°)
	N-peak	260.8–265.5	2.5 (8σ)	(04 33 59.99, −08 34 44.7)	0.31	1.06×0.58 (−75°)
IRAS 12127–1412	Nucleus	233.7–238.4	1.4 (25σ)	(12 15 19.13, −14 29 41.7)	0.057	0.94×0.74 (71°)
IRAS 15250+3609	Nucleus	251.0–255.8	11 (41σ)	(15 26 59.42, +35 58 37.4)	0.27	1.21×0.72 (−0°)
PKS 1345+12	Nucleus	236.0–240.7	364 (70σ)	(13 47 33.37, +12 17 24.2)	5.2	0.92×0.85 (−24°)
IRAS 06035–7102	Nucleus	245.4–250.2	2.4 (19σ)	(06 02 53.95, −71 03 10.2)	0.13	1.12×0.78 (49°)
IRAS 13509+0442	Nucleus	233.1–237.7	1.5 (20σ)	(13 53 31.57, +04 28 04.8)	0.076	0.99×0.81 (46°)
	NE source	233.1–237.7	1.9 (26σ)	(13 53 31.66, +04 28 13.1)	0.076	0.99×0.81 (46°)
IRAS 20414–1651	Nucleus	243.9–248.6	5.2 (38σ)	(20 44 18.17, −16 40 16.8)	0.14	0.76×0.66 (−89°)

NOTE. — Col.(1): Object name. Col.(2): Position inside galaxy. Col.(3): Observed frequency used for continuum extraction in [GHz]. Frequencies at obvious emission lines are removed. Col.(4): Flux in [mJy beam<sup>-1</sup>] at the emission peak. The value at the highest flux pixel (0.1 pixel<sup>-1</sup>) in the continuum map is adopted. The detection significance relative to the rms noise is shown in parentheses, where possible systematic uncertainty is not included. The possible systematic ambiguity in The Superantennae could be larger than the remaining sources due to the very broad HCN/HCO<sup>+</sup> J=3–2 emission line profiles, extending almost all frequency coverage of each of the corresponding spectral windows. Col.(5): The coordinate of the continuum emission peak in J2000. Col.(6): The rms noise level (1σ) in [mJy beam<sup>-1</sup>], derived from the standard deviation of sky signals in each continuum map. Col.(7): Synthesized beam in [arcsec × arcsec] and position angle in [degree]. The position angle is 0° along the north–south direction and increases in the counterclockwise direction.

TABLE 4  
FLUX OF THE HCN J=3–2 EMISSION LINE

Object	Pos	Integrated intensity (moment 0) map				Velocity [km s <sup>-1</sup> ]	Gaussian line fit		
		Peak [Jy beam <sup>-1</sup> km s <sup>-1</sup> ]	rms [Jy beam <sup>-1</sup> km s <sup>-1</sup> ]	Ch Sum	Beam [" × "]		Peak [mJy]	FWHM [km s <sup>-1</sup> ]	Flux [Jy km s <sup>-1</sup> ]
(1)	(2)	(3)	(4)	(5)	(6)	(7)	(8)	(9)	(10)
NGC 7469	Nuc	5.4 (59σ)	0.092	21	0.58×0.52	4909±2	24±1	220±3	5.5±0.1
	SB1	0.96 (10σ)	0.092	21	0.58×0.52	4966±1	15±1	63±1	0.96±0.03
	SB2	0.70 (8σ)	0.092	21	0.58×0.52	4916±1	11±1	65±2	0.72±0.03
	SB3	0.67 (7σ)	0.092	21	0.58×0.52	5028±1	12±1	51±2	0.65±0.03
	ring	—	—	—	—	4952±5	45±2	214±12	10.1±1.0
I Zw 1	Nuc	2.6 (31σ)	0.086	21	0.69×0.63	18335±3	10±1	296±7	2.9±0.1
08572+3915	Nuc	2.5 (14σ)	0.18	27	0.91×0.47	17501±7	6.6±0.2	382±17	2.6±0.1
Superant	Nuc	9.6 (20σ)	0.47	58	0.88×0.66	18540±7	12.8±0.2	821±17	10.6±0.3 <sup>E</sup>
12112+0305	NE	8.3 (28σ)	0.30	34	0.73×0.54	21661±18, 21958±20	15.0±1.4, 14.6±1.2	283±34, 273±46	8.1±1.2
	SW	0.72 (4σ)	0.17 <sup>B</sup>	16 <sup>B</sup>	0.73×0.54	21807±4 <sup>C</sup>	24±1 <sup>C</sup>	431±14 <sup>C</sup>	10.4±0.7 <sup>C</sup>
22491–1808	Nuc	7.3 (26σ)	0.28	29	0.95×0.60	21970±34	2.0±0.5	323±75	0.64±0.22
NGC 1614	SB1	0.86 (4σ)	0.21	16	1.07×0.58	23309±6	18.0±0.5	458±13	8.1±0.3
	SB2	1.0 (5σ)	0.21	16	1.07×0.58	4847±7	8.1±1.2	103±18	0.87±0.20
	2'5	—	—	—	—	4763±8	7.2±1.0	128±23	0.85±0.22
12127–1412	Nuc	1.1 (12σ)	0.087	14	0.94×0.74	4812±23	19.1±3.8	258±66	5.1±1.7
15250+3609	Nuc	4.7(32σ) <sup>A</sup>	0.15 <sup>A</sup>	9 <sup>A</sup>	1.21×0.73	39961±14	2.6±0.1	524±33	1.3±0.1
PKS 1345	Nuc	2.3(20σ)	0.11	12	0.92×0.86	16575±5 <sup>A</sup>	19±1 <sup>A</sup>	274±10 <sup>A</sup>	5.2±0.3 <sup>A</sup>
06035–7102	Nuc	4.4(25σ)	0.17	13	1.12×0.78	36456±15	6.0±0.4	480±34	2.7±0.3
13509+0442	Nuc	0.96(13σ)	0.074	9	0.99×0.81	23853±5	14±1	367±12	4.9±0.2
20414–1651	Nuc	3.9 (26σ)	0.15	17	0.76×0.66	40937±6	4.5±0.2	268±15	1.1±0.2
						25829±11, 26216±12	7.4, 8.2	250±24, 309±28	4.3±0.3
						26050±4 <sup>D</sup>	53±15 <sup>D</sup>	336±20 <sup>D</sup>	17±5 <sup>D</sup>

NOTE. — Col.(1): Object. Col.(2): Position. For NGC 7469, “ring” refers to an annular region with a radius of 0'8–2'5. For NGC 1614, “2'5” refers to a 2'5 radius circular region. Col.(3): Integrated intensity of the HCN J=3–2 emission line ( $\nu_{\text{rest}}=265.89$  GHz) in [Jy beam<sup>-1</sup> km s<sup>-1</sup>] at the emission peak. The detection significance relative to the rms noise ( $1\sigma$ ) in the moment 0 map is shown in parentheses. Possible systematic uncertainty is not included. Col.(4): rms noise ( $1\sigma$ ) level in the moment 0 map in [Jy beam<sup>-1</sup> km s<sup>-1</sup>], derived from the standard deviation of sky signals in each moment 0 map. Col.(5): The number of velocity channels summed to create moment 0 maps. Each velocity channel has a width of  $\sim 20$  MHz ( $\sim 20$  km s<sup>-1</sup>) for objects observed in ALMA Cycles 1 and 2, or  $\sim 40$  MHz ( $\sim 40$  km s<sup>-1</sup>) for those observed in ALMA Cycle 3 (bottom six sources). Col.(6): Beam size in [arcsec × arcsec]. Cols.(7)–(10): Gaussian fits of emission lines in the spectra at the continuum peak position (except for NGC 1614), within the beam size, or integrated starburst regions for NGC 7469 and NGC 1614. For NGC 1614, spectra are taken at the HCN J=3–2 emission peaks. Col.(7): Optical local standard of rest (LSR) velocity ( $\nu_{\text{opt}}$ ) of the emission peak in [km s<sup>-1</sup>]. Col.(8): Peak flux in [mJy]. Col.(9): Observed FWHM in [km s<sup>-1</sup>] in the left panels of Figure 9. Col.(10): Flux in [Jy km s<sup>-1</sup>]. The observed FWHM in [km s<sup>-1</sup>] in column 9 is divided by  $(1+z)$  to obtain the intrinsic FWHM in [km s<sup>-1</sup>].

<sup>A</sup> Only the bright main emission component at 251.8–252.2 GHz in Figure 5(j) is considered. The fainter sub-peak component at 251.3–251.8 GHz, which is likely to be of outflow origin, is not included.

<sup>B</sup> The frequency range of significant signal detection is slightly different between the NE and SW nuclei. We created the moment 0 map of the SW nucleus by summing channels with significant signal detection at the SW nucleus.

<sup>C</sup> Single Gaussian fit after removing data points affected by the central dips, based on the assumption of self-absorption. Data at 21360–21650 km s<sup>-1</sup> and 21970–22260 km s<sup>-1</sup> in Figure 9 are used for the fit.

<sup>D</sup> Single Gaussian fit after removing data points affected by the central dips, based on the assumption of self-absorption. Data at 25200–25760 km s<sup>-1</sup> and 26340–27000 km s<sup>-1</sup> in Figure 9 are used for the fit.

<sup>E</sup> Because the HCN J=3–2 emission line is extremely broad, extending almost all frequency coverage of the ALMA spectral window, the ambiguity of the continuum determination is large. The possible systematic uncertainty is expected to be larger than for other objects.

TABLE 5  
FLUX OF THE HCO<sup>+</sup> J=3–2 EMISSION LINE

Object	Pos	Integrated intensity (moment 0) map				Velocity [km s <sup>-1</sup> ]	Gaussian line fit		Flux [Jy km s <sup>-1</sup> ]
		Peak [Jy beam <sup>-1</sup> ]	rms [km s <sup>-1</sup> ]	Ch Sum	Beam [" × "]		Peak [mJy]	FWHM [km s <sup>-1</sup> ]	
(1)	(2)	(3)	(4)	(5)	(6)	(7)	(8)	(9)	(10)
NGC 7469	Nuc	4.6 (49σ)	0.094	19	0.57×0.52	4914±2	21±1	217±3	4.8±0.1
	SB1	1.2 (13σ)	0.094	19	0.57×0.52	4966±1	22±1	57±1	1.3±0.03
	SB2	0.97 (10σ)	0.094	19	0.57×0.52	4914±1	15±1	63±1	0.96±0.03
	SB3	0.86 (9σ)	0.094	19	0.57×0.52	5028±1	19±1	46±1	0.93±0.03
	ring	—	—	—	—	4948±6	63±3	217±12	14.4±1.0
I Zw 1	Nuc	1.2 (23σ)	0.053	18	0.66×0.59	18328±5	4.5±0.1	314±13	1.4±0.1
08572+3915	Nuc	2.8 (13σ)	0.21	19	0.89×0.47	17482±7	9.7±0.5	300±16	2.9±0.2
Superant	Nuc	6.6 (19σ)	0.35	48	0.88×0.62	18555±10	9.9±0.3	767±23	7.6±0.3 <sup>E</sup>
12112+0305	NE	4.5 (17σ)	0.26	25	0.76×0.62	21665±7, 21979±6	11.1±0.7, 12.4±0.8	185±18, 208±20	4.6±0.4
						21829±5 <sup>C</sup>	27±3 <sup>C</sup>	331±19 <sup>C</sup>	9.0±0.1 <sup>C</sup>
22491–1808	SW	1.4 (7σ)	0.21 <sup>B</sup>	18 <sup>B</sup>	0.76×0.62	21888±17, 22071±16	4.5±0.5, 4.3±0.8	186±37, 125±33	1.4±0.3
	Nuc	3.5 (14σ)	0.25	26	0.95×0.60	23255±11	9.7±0.5	371±30	3.6±0.3
NGC 1614	SB1	2.0 (7σ)	0.28	18	1.06×0.57	4846±1	27.3±1.2	65±4	1.9±0.1
	SB2	2.0 (7σ)	0.28	18	1.06×0.57	4769±4	15.4±1.2	112±11	1.8±0.2
	2'5	—	—	—	—	4766±13	57±4	263±18	15.7±1.5
12127–1412	Nuc	0.80 (11σ)	0.075	11	0.94×0.74	39980±16	2.3±0.2	457±32	0.97±0.09
15250+3609	Nuc	2.0(21σ) <sup>A</sup>	0.094 <sup>A</sup>	7 <sup>A</sup>	1.21×0.72	16568±9 <sup>A</sup>	11±1 <sup>A</sup>	186±19 <sup>A</sup>	2.0±0.3 <sup>A</sup>
PKS 1345	Nuc	3.3(29σ)	0.12	12	0.92×0.85	36454±13	8.7±0.5	486±27	4.0±0.3
06035–7102	Nuc	5.6(32σ)	0.18	13	1.12×0.78	23868±4	17±1	378±9	6.3±0.2
13509+0442	Nuc	1.2(18σ)	0.063	7	0.97×0.80	40923±6	5.9±0.3	251±13	1.4±0.1
20414–1651	Nuc	2.6 (13σ)	0.21	15	0.76×0.67	25834±12, 26259±12	5.8±0.5, 6.3±0.5	235±31, 273±32	3.0±0.3
						26055±3 <sup>D</sup>	37±9 <sup>D</sup>	348±17 <sup>D</sup>	13±3 <sup>D</sup>

NOTE. — Col.(1): Object. Col.(2): Position. Definitions are the same as those in Table 4. Col.(3): Integrated intensity of the HCO<sup>+</sup> J=3–2 emission ( $\nu_{\text{rest}} = 267.56$  GHz) in [Jy beam<sup>-1</sup> km s<sup>-1</sup>] at the emission peak. The detection significance relative to the rms noise ( $1\sigma$ ) in the moment 0 map is shown in parentheses. Possible systematic uncertainty is not included. Col.(4): rms noise ( $1\sigma$ ) level in the moment 0 map in [Jy beam<sup>-1</sup> km s<sup>-1</sup>], derived from the standard deviation of sky signals in each moment 0 map. Col.(5): The number of velocity channels summed to create moment 0 maps. Each velocity channel has a width of  $\sim 20$  MHz ( $\sim 20$  km s<sup>-1</sup>) for objects observed in ALMA Cycles 1 and 2, or  $\sim 40$  MHz ( $\sim 40$  km s<sup>-1</sup>) for those observed in ALMA Cycle 3 (bottom six sources). Col.(6): Beam size in [arcsec × arcsec]. Cols.(7)–(10): Gaussian fits of emission lines in the spectra, made in the same way as Table 4. Col.(7): Optical LSR velocity ( $v_{\text{opt}}$ ) of the emission peak in [km s<sup>-1</sup>]. Col.(8): Peak flux in [mJy]. Col.(9): Observed FWHM in [km s<sup>-1</sup>] in the right panels of Figure 9. Col.(10): Flux in [Jy km s<sup>-1</sup>].

<sup>A</sup> Only the bright main emission component at 253.4–253.7 GHz in Figure 5(j) is considered. The fainter sub-peak component at 253.0–253.3 GHz, which is likely to be of outflow origin, is not included.

<sup>B</sup> The frequency range for significant signal detection is slightly different between the NE and SW nuclei. We created the moment 0 map of the SW nucleus by summing channels with significant signal detection at the SW nucleus.

<sup>C</sup> Single Gaussian fit after removing data points affected by the central dips, based on the assumption of self-absorption. Data at 21500–21660 km s<sup>-1</sup> and 21970–22130 km s<sup>-1</sup> in Figure 9 are used for the fit.

<sup>D</sup> Single Gaussian fit after removing data points affected by the central dips, based on the assumption of self-absorption. Data at 25200–25760 km s<sup>-1</sup> and 26340–27000 km s<sup>-1</sup> in Figure 9 are used for the fit.

<sup>E</sup> Because the HCO<sup>+</sup> J=3–2 emission line is extremely broad, extending across almost all frequency coverage of the ALMA spectral window, the ambiguity in continuum determination is large. The possible systematic uncertainty is expected to be larger than that of other objects.

TABLE 6  
FLUX OF VIBRATIONALLY EXCITED ( $v_2=1F$ ) HCN AND HCO<sup>+</sup> J=3–2 EMISSION LINES FOR SELECTED SOURCES

Object	Line	$\nu_{\text{rest}}$ [GHz]	Integrated intensity (moment 0) map			
			Peak [Jy beam <sup>-1</sup> km s <sup>-1</sup> ]	rms (5)	Channels Summed (6)	Beam [" × "'] (°) (7)
(1)	(2)	(3)	(4)	(5)	(6)	(7)
NGC 7469 (nucleus)	HCN $v_2=1f$ J=3–2	267.20	<0.10 (<3 $\sigma$ )	0.032	10	0.57×0.52 (78°)
	HCO <sup>+</sup> $v_2=1f$ J=3–2	268.69	<0.11 (<3 $\sigma$ )	0.034	10	0.56×0.50 (54°)
I Zw 1	HCN $v_2=1f$ J=3–2	267.20	<0.10 (<3 $\sigma$ )	0.032	10	0.66×0.59 (61°)
	HCO <sup>+</sup> $v_2=1f$ J=3–2	268.69	<0.11 (<3 $\sigma$ )	0.035	10	0.62×0.60 (–31°)
IRAS 08572+3915	HCN $v_2=1f$ J=3–2	267.20	0.28 (2.2 $\sigma$ ) {<0.38 (<3 $\sigma$ )}	0.13	15	0.89×0.47 (–19°)
	HCO <sup>+</sup> $v_2=1f$ J=3–2	268.69	<0.21 (<3 $\sigma$ )	0.067	10	0.88×0.46 (–19°)
IRAS 12112+0305 NE	HCN $v_2=1f$ J=3–2	267.20	0.52 (4.5 $\sigma$ )	0.11	13	0.76×0.62 (68°)
	HCO <sup>+</sup> $v_2=1f$ J=3–2	268.69	<0.41 (<3 $\sigma$ )	0.13	10	0.72×0.54 (68°)
IRAS 22491–1808	HCN $v_2=1f$ J=3–2	267.20	0.45 (4.0 $\sigma$ )	0.11	9	0.91×0.60 (67°)
	HCO <sup>+</sup> $v_2=1f$ J=3–2	268.69	<0.40 (<3 $\sigma$ )	0.13	10	0.89×0.59 (67°)
IRAS 20414–1651	HCN $v_2=1f$ J=3–2	267.20	0.13 (2.0 $\sigma$ ) {<0.20 (<3 $\sigma$ )}	0.064	4	0.76×0.67 (–88°)
	HCO <sup>+</sup> $v_2=1f$ J=3–2	268.69	<0.19 (<3 $\sigma$ )	0.063	6	0.75×0.66 (90°)

NOTE. — Col.(1): Object. Col.(2): Observed molecular line. Col.(3): Rest-frame frequency of each molecular line in [GHz]. Col.(4): Integrated intensity in [Jy beam<sup>-1</sup> km s<sup>-1</sup>] at the emission peak. Detection significance relative to the rms noise (1 $\sigma$ ) in the moment 0 map is shown in parentheses. Possible systematic uncertainty is not included. Col.(5): rms noise (1 $\sigma$ ) level in the moment 0 map in [Jy beam<sup>-1</sup> km s<sup>-1</sup>], derived from the standard deviation of sky signals in each moment 0 map. Col.(6): The number of velocity channels summed to create moment 0 maps. Each velocity channel has a width of  $\sim 20$  MHz ( $\sim 20$  km s<sup>-1</sup>) except for IRAS 20414–1651, which has a width of  $\sim 40$  MHz ( $\sim 40$  km s<sup>-1</sup>). Col.(7): Beam size in [arcsec × arcsec] and position angle in [degree]. The position angle is 0° along the north-south direction, and increases counterclockwise.

TABLE 7  
INTRINSIC EMISSION SIZE AFTER DECONVOLUTION

Object	HCN J=3–2 [mas × mas] (°)	HCO <sup>+</sup> J=3–2 [mas × mas] (°)	continuum [mas × mas] (°)
(1)	(2)	(3)	(4)
NGC 7469 nucleus	680±60, 510±50 (48±17)	810±100, 570±80 (46±18)	2480±440, 710±150 (53±4)
I Zw 1	340±50, 190±90 (37±22)	370±50, 290±60 (40±55)	650±60, 340±50 (53±7)
IC 4329 A	—	—	190±30, 110±60 (42±21)
IRAS 08572+3915	490±150, 330±110 (145±67)	540±160, 300±160 (140±31)	500±80, 360±90 (125±28)
Superantennae	310±70, 100±160 (130±39)	520±80, 130±60 (143±13)	590±60, 340±80 (163±12)
IRAS 12112+0305 NE	360±30, 140±60 (155±13)	370±90, 150±140 (128±27)	250±40, 230±40 (85±84)
IRAS 22491–1808	210±100, 150±80 (10±64)	could not deconvolve	<430, <110 (—)
IRAS 12127–1412	<370, <240 (—)	could not deconvolve	360±90, 230±130 (66±62)
IRAS 15250+3609	380±100, 270±130 (149±50)	280±130, 140±150 (117±70)	270±100, 240±170 (179±78)
PKS 1345+12	<430, <200 (—)	340±60, 90±130 (88±16)	150±30, 100±70 (81±83)
IRAS 06035–7102	<380, <240 (—)	540±50, 480±90 (148±73)	460±110, 380±200 (103±66)
IRAS 13509+0442	<670, <270 (—)	550±100, 320±200 (174±23)	430±80, 400±100 (78±85)
IRAS 13509+0442 NE	—	—	<390, <230 (—)
IRAS 20414–1651	470±60, 300±110 (178±59)	520±120, 410±160 (105±82)	400±40, 320±50 (168±25)

NOTE. — Col.(1): Object name. Cols.(2), (3), and (4): Intrinsic emission size of HCN J=3–2, HCO<sup>+</sup> J=3–2, and continuum in [mas], respectively, after deconvolution using the CASA task “imfit”. The position angle in [degree] is shown in parentheses.

TABLE 8  
LUMINOSITY OF THE HCN AND HCO<sup>+</sup> v=0 J=3-2 EMISSION LINES

Object	HCN J=3-2 10 <sup>4</sup> [L <sub>⊙</sub> ]	HCO <sup>+</sup> J=3-2 10 <sup>4</sup> [L <sub>⊙</sub> ]	HCN J=3-2 10 <sup>7</sup> [K km s <sup>-1</sup> pc <sup>2</sup> ]	HCO <sup>+</sup> J=3-2 10 <sup>7</sup> [K km s <sup>-1</sup> pc <sup>2</sup> ]
(1)	(2)	(3)	(4)	(5)
NGC 7469 nucleus	0.74±0.01	0.65±0.01	1.2±0.1	1.1±0.1
NGC 7469 SB ring	1.33±0.01	1.92±0.01	2.2±0.1	3.1±0.1
I Zw 1	5.5±0.2	2.7±0.2	9.2±0.3	4.4±0.3
IRAS 08572+3915	4.5±0.2	5.0±0.3	7.4±0.3	8.2±0.6
Superantennae	17.9±0.8	10.8±0.6	29.7±1.3	17.5±1.0
IRAS 12112+0305 NE	16.7±0.2	9.5±0.8	27.8±4.1	15.6±1.4
IRAS 12112+0305 SW	1.8±0.6	3.9±0.8	2.9±1.0	6.3±1.3
IRAS 22491-1808	21.1±0.9	11.2±1.9	35.0±1.5	18.3±3.1
NGC 1614 (2''5 radius)	0.65±0.22	2.0±0.2	1.1±0.4	3.3±0.3
IRAS 12127-1412	12.1±0.9	9.1±0.8	20.2±1.6	14.9±1.4
IRAS 15250+3609	7.8±0.5	3.1±0.5	13.0±0.8	5.0±0.8
PKS 1345+12	21.1±2.4	31.5±2.4	35.1±3.9	51.4±3.9
IRAS 06035-7102	15.8±0.6	20.4±0.6	26.2±1.1	33.2±1.1
IRAS 13509+0442	10.8±2.0	13.8±1.0	17.9±3.3	22.5±1.6
IRAS 20414-1651	16.8±1.2	11.8±1.2	28.0±2.0	19.3±1.9

NOTE. — Col.(1): Object name. Cols.(2) and (3): Luminosity of the HCN J=3-2 and HCO<sup>+</sup> J=3-2 emission lines in units of [L<sub>⊙</sub>], respectively. Cols.(4) and (5): Luminosity of the HCN J=3-2 and HCO<sup>+</sup> J=3-2 emission lines in units of [K km s<sup>-1</sup> pc<sup>2</sup>], respectively.

TABLE 9  
LUMINOSITY OF THE HCN v<sub>2</sub>=1f J=3-2 EMISSION LINE

Object	L(HCN v <sub>2</sub> =1f J=3-2) 10 <sup>4</sup> [L <sub>⊙</sub> ]	L'(HCN v <sub>2</sub> =1f J=3-2) 10 <sup>7</sup> [K km s <sup>-1</sup> pc <sup>2</sup> ]
(1)	(2)	(3)
IRAS 12112+0305 NE	1.4	2.3
IRAS 22491-1808	1.4	2.3

NOTE. — Col.(1): Object name. Col.(2): Luminosity of the HCN J=3-2 v<sub>2</sub>=1f emission line in units of [L<sub>⊙</sub>]. Col.(3): Luminosity of the HCN J=3-2 v<sub>2</sub>=1f emission line in units of [K km s<sup>-1</sup> pc<sup>2</sup>].

TABLE 10  
RADIO PROPERTIES OF  
NGC 7469, I ZW 1, AND IC  
4329 A

Object	S <sub>1.4GHz</sub> [mJy]	q
(1)	(2)	(3)
NGC 7469	181	2.3
I Zw 1	8.8	2.5
IC 4329 A	66.8	1.5

NOTE. — Col.(1): Object name. Col.(2): Radio 1.4 GHz flux in [mJy] (Condon et al. 1998). Col.(3): Far-infrared-to-radio flux ratio, parameterized as the q-value (Condon et al. 1991).

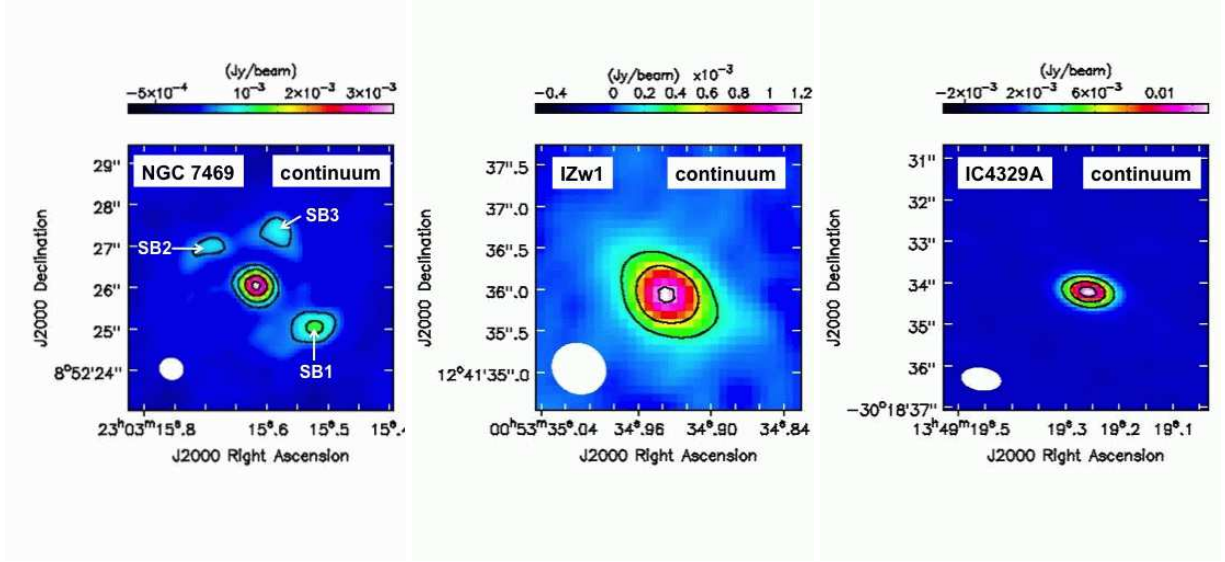


FIG. 1.— Continuum maps of NGC 7469, I Zw 1, and IC 4329 A. For NGC 7469,  $5\sigma$ ,  $10\sigma$ ,  $20\sigma$ , and  $30\sigma$  contours, as well as the locations of the starburst knots SB1, SB2, and SB3, are shown. The plotted contours are  $5\sigma$ ,  $10\sigma$ ,  $20\sigma$  for I Zw 1, and  $20\sigma$ ,  $40\sigma$ ,  $60\sigma$  for IC 4329 A.

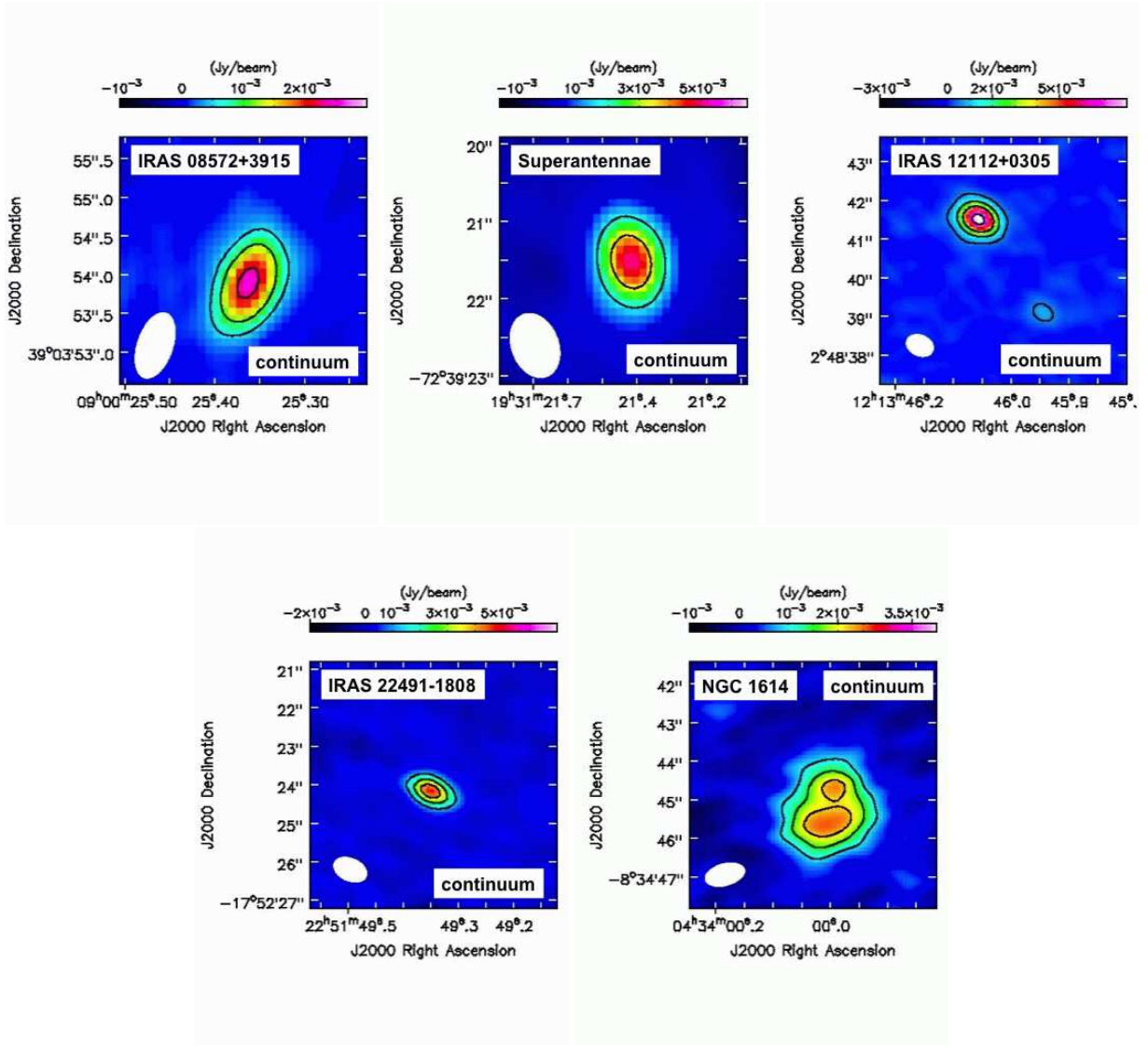


FIG. 2.— Continuum maps of LIRGs observed in ALMA Cycle 2. The displayed apparent scale depends on the structure of the individual objects and the beam size of the individual data. The contours are  $5\sigma$ ,  $10\sigma$ ,  $20\sigma$  for IRAS 08572+3915,  $10\sigma$ ,  $20\sigma$  for The Superantennae,  $3\sigma$ ,  $10\sigma$ ,  $20\sigma$ ,  $40\sigma$  for IRAS 12112+0305,  $5\sigma$ ,  $10\sigma$ ,  $15\sigma$  for IRAS 22491–1808, and  $3\sigma$ ,  $5\sigma$ ,  $7\sigma$  for NGC 1614.



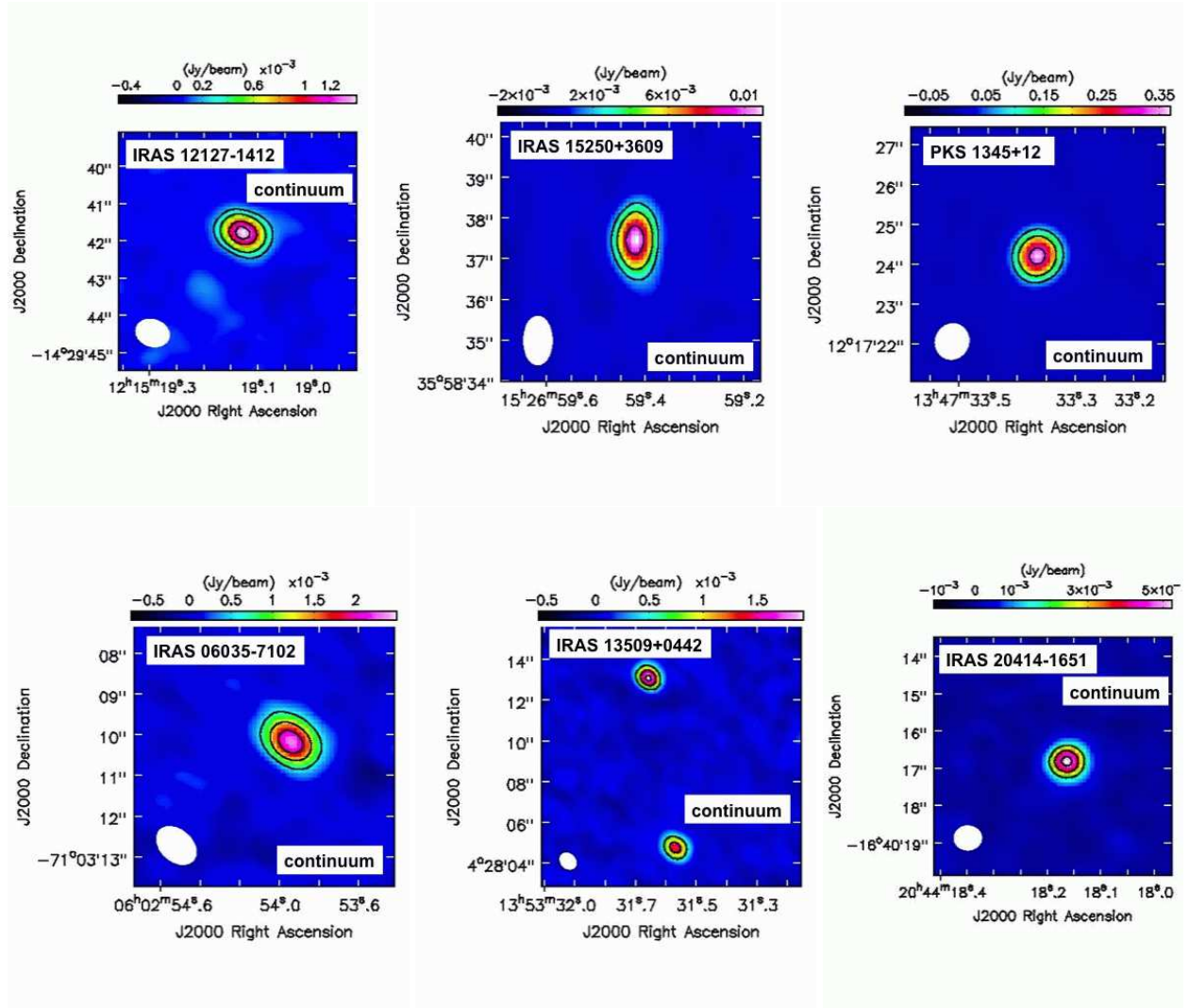


FIG. 3.— Continuum maps of LIRGs observed in ALMA Cycle 3. The displayed apparent scale depends on the structure of the individual objects and the beam size of the individual data. The contours are  $4\sigma$ ,  $8\sigma$ ,  $16\sigma$ ,  $22\sigma$  for IRAS 12127–1412,  $8\sigma$ ,  $16\sigma$ ,  $32\sigma$  for IRAS 15250+3609,  $15\sigma$ ,  $30\sigma$ ,  $60\sigma$  for PKS 1345+12,  $5\sigma$ ,  $10\sigma$ ,  $15\sigma$  for IRAS 06035–7102,  $8\sigma$ ,  $16\sigma$ ,  $24\sigma$  for IRAS 13509+0442, and  $15\sigma$ ,  $25\sigma$ ,  $35\sigma$  for IRAS 20414–1651. IRAS 13509+0442 is the galaxy seen in the lower part of the image, and the continuum emission in the upper part is from another optically faint source.

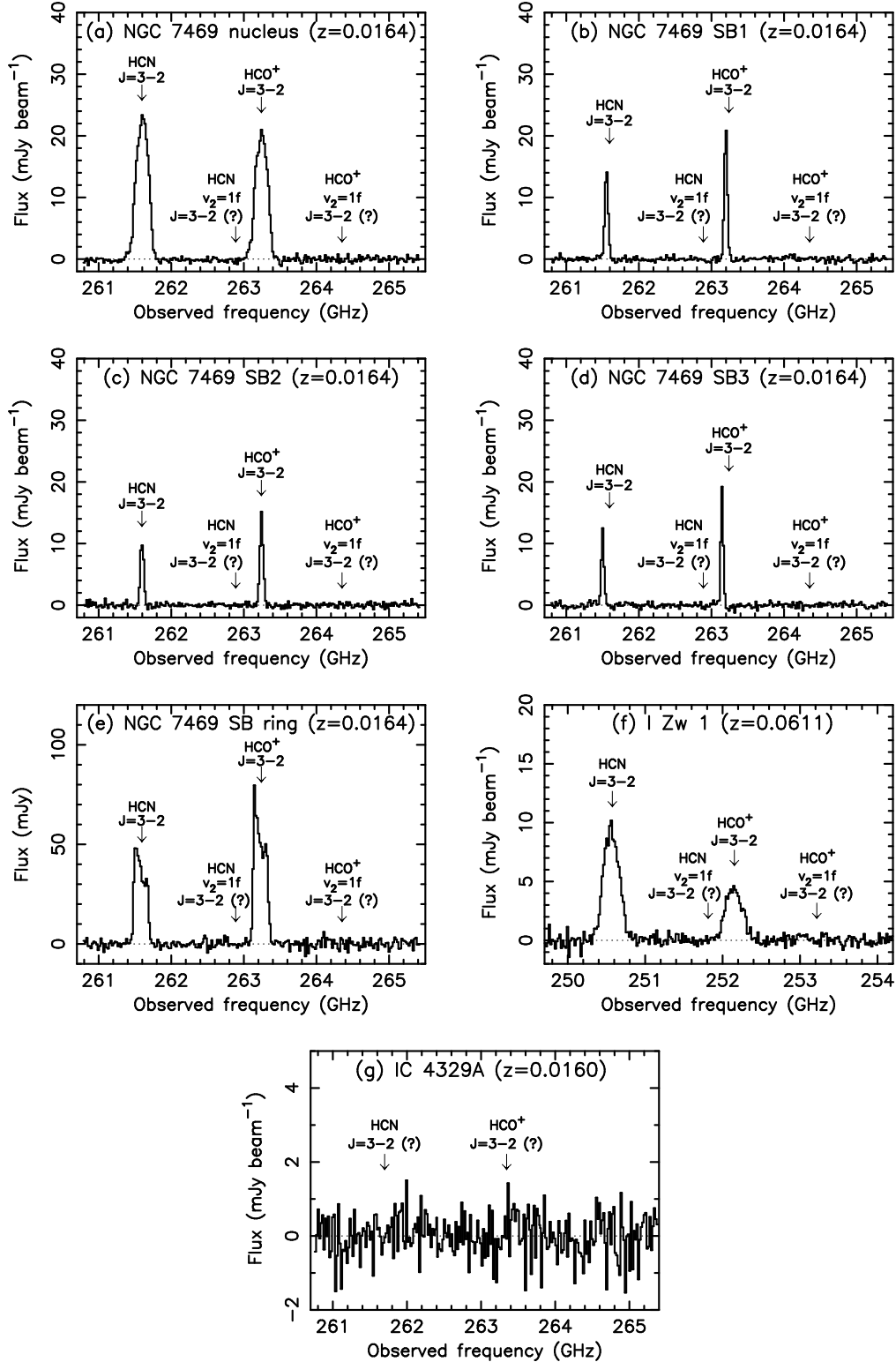
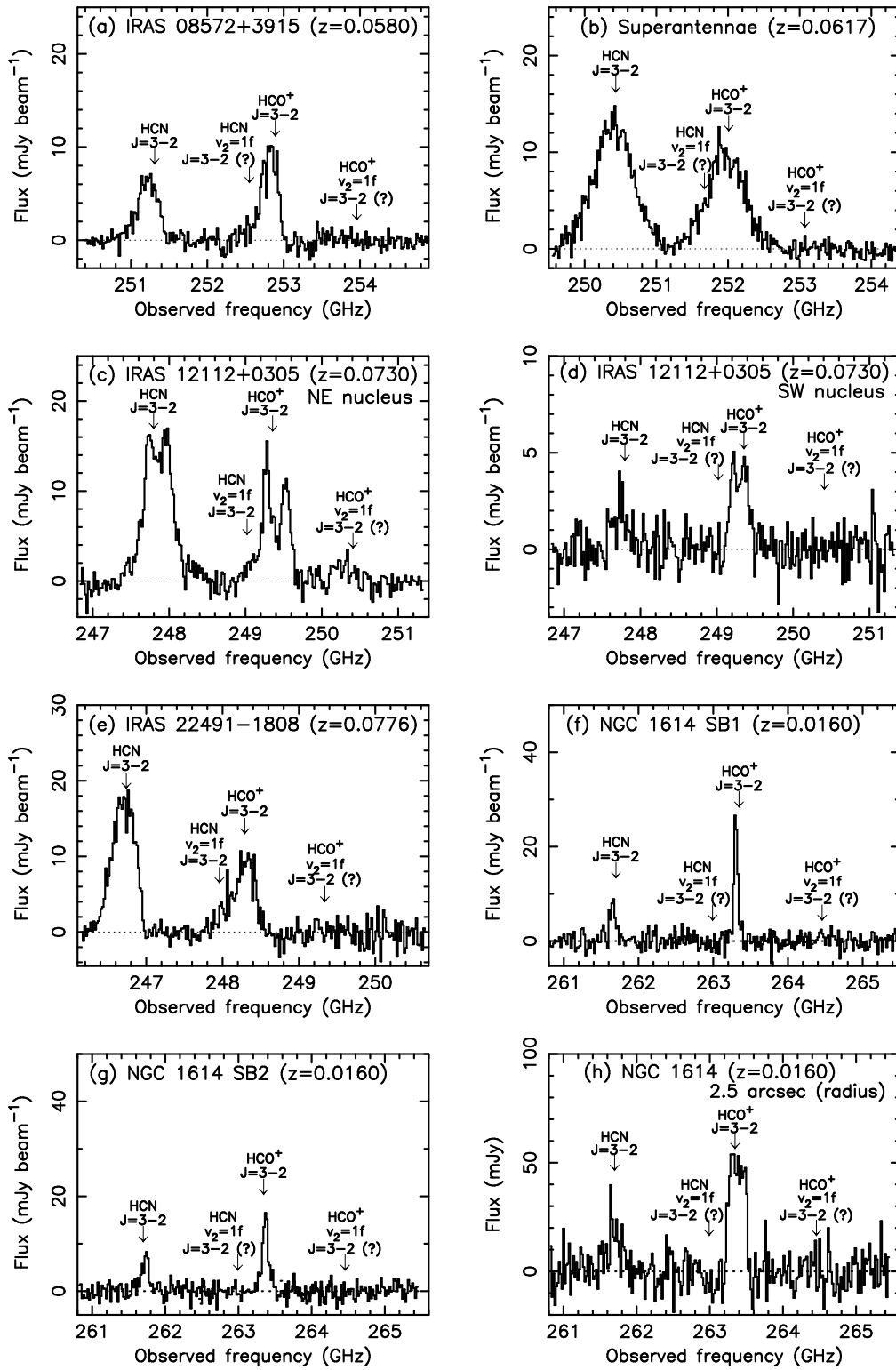


FIG. 4.— Full frequency coverage spectra at interesting regions of optical Seyfert 1 galaxies. Spectra are taken within the beam size, except for (e). (a), (b), (c), and (d) are spectra at the NGC 7469 nucleus defined as the continuum emission peak, SB1, SB2, and SB3, respectively. (e) is the area-integrated spectrum of the annular region at  $0''.8-2''.5$  radius from the nucleus of NGC 7469. (f) and (g) are spectra of the nuclei of I Zw 1 and IC 4329 A (defined as the continuum emission peaks), respectively. Down arrows are shown at the expected observed frequency of some emission lines for the adopted redshifts (Table 1).



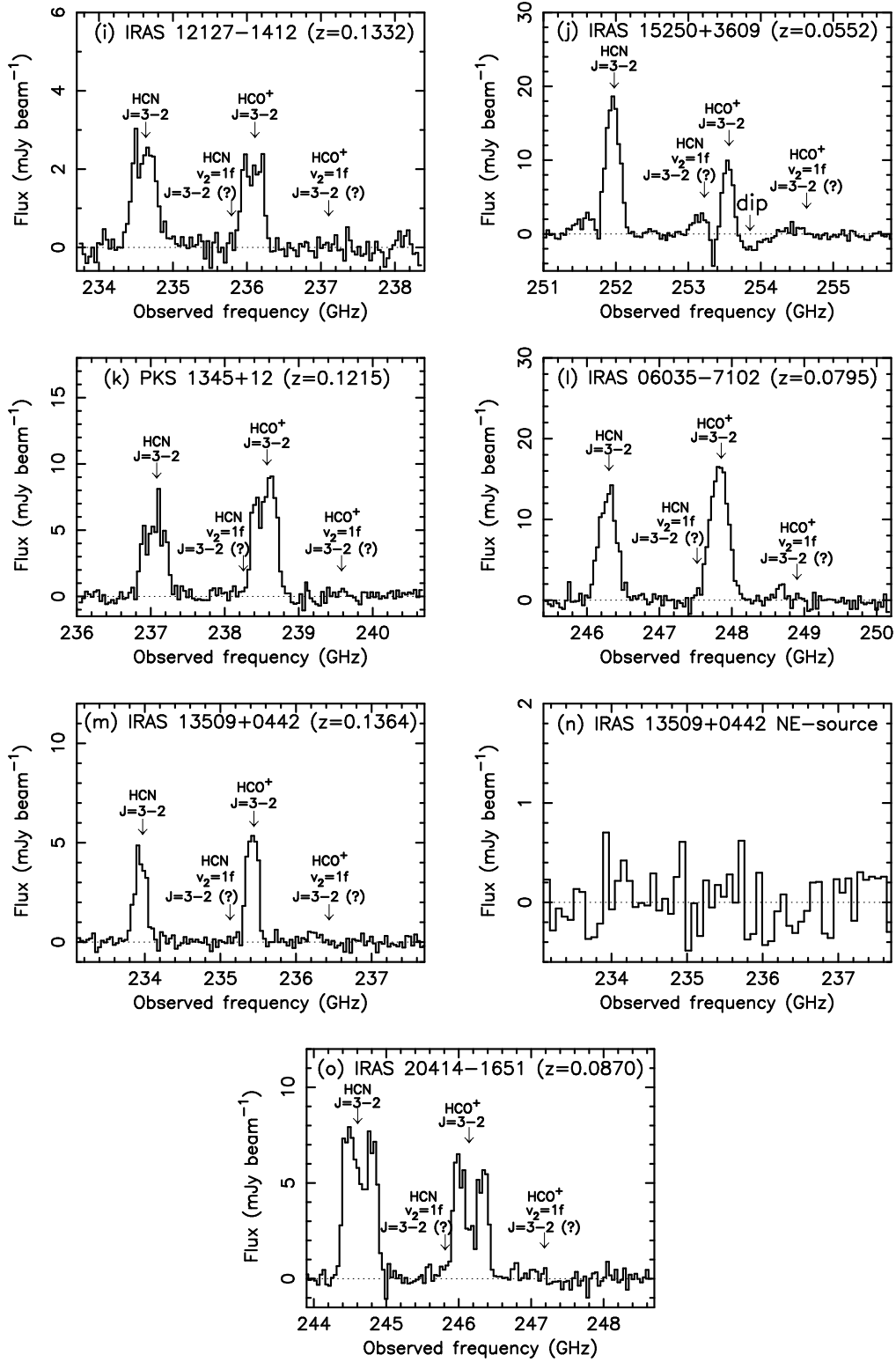


FIG. 5.— Full frequency coverage spectra of LIRGs at interesting regions. Spectra are taken within the beam size, except for (h). The SB1 and SB2 of NGC 1614 are defined from the HCN  $J=3-2$  emission peak (see text in §4). Down arrows are shown at the expected observed frequency of some emission lines for the redshifts shown in Table 1. The binned spectrum of the NE source detected in the continuum map of IRAS 13509+0442 is also shown.

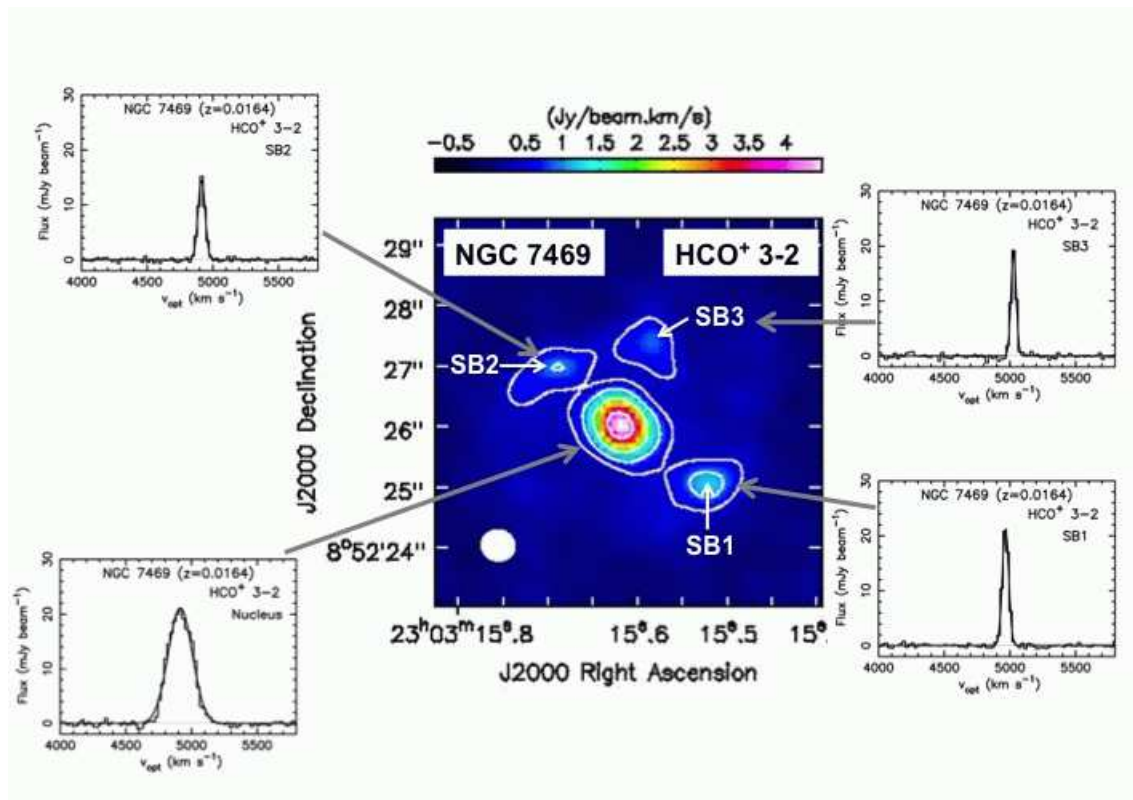
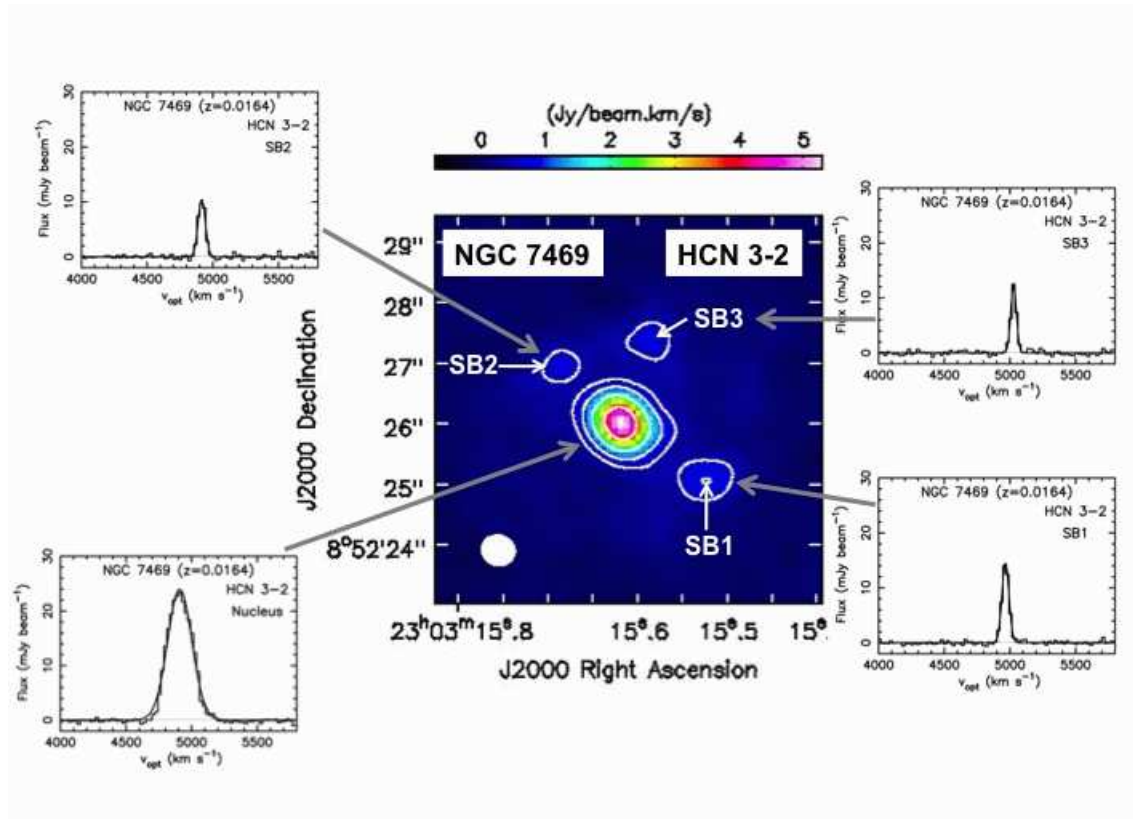


FIG. 6.— Integrated intensity (moment 0) maps of the HCN J=3-2 and HCO<sup>+</sup> J=3-2 emission lines, and their Gaussian fits in the spectra at individual locations within the beam size, for NGC 7469. For moment 0 maps of HCN J=3-2 and HCO<sup>+</sup> J=3-2, the contours represent the 5 $\sigma$ , 10 $\sigma$ , 20 $\sigma$ , and 40 $\sigma$  levels.

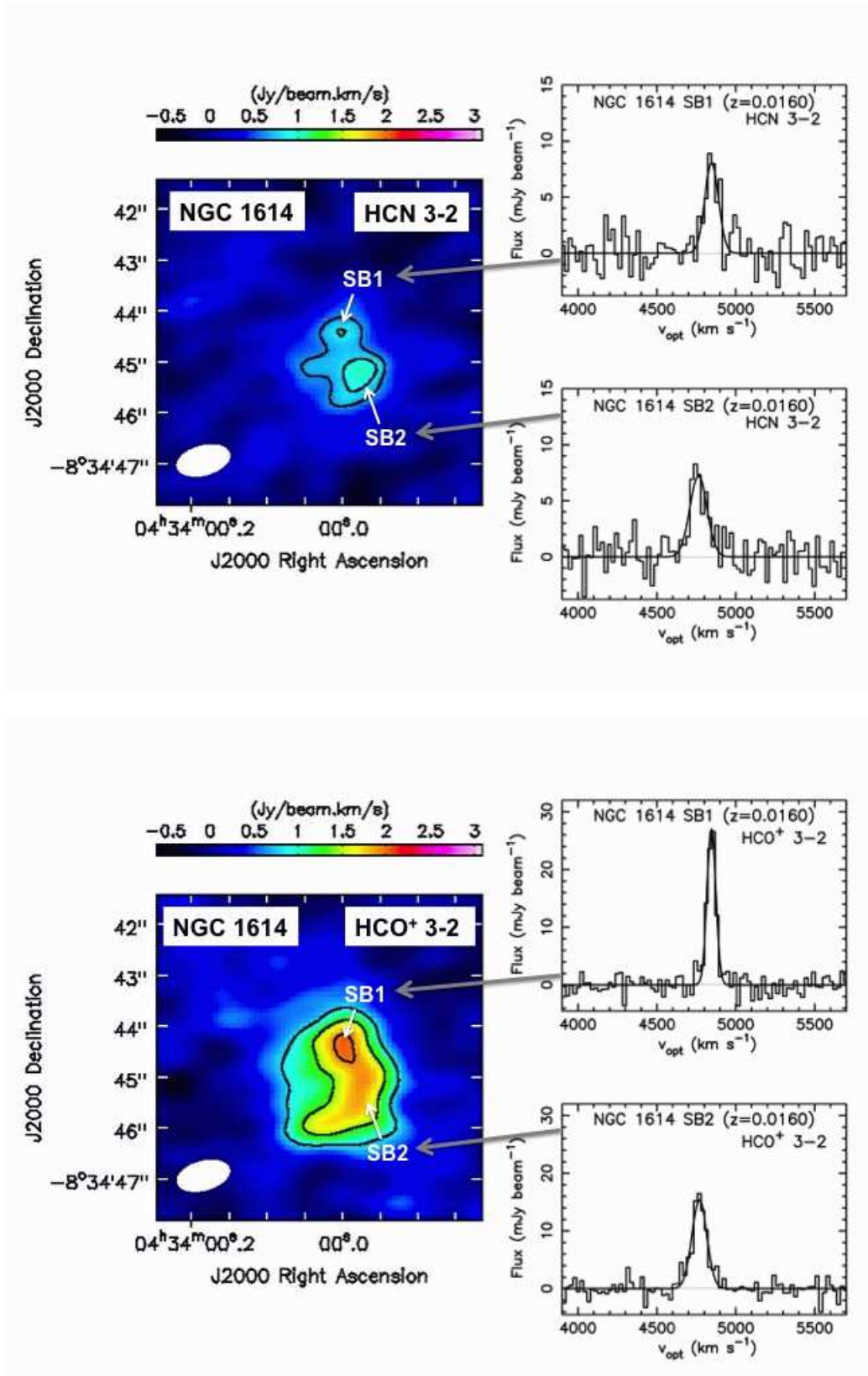
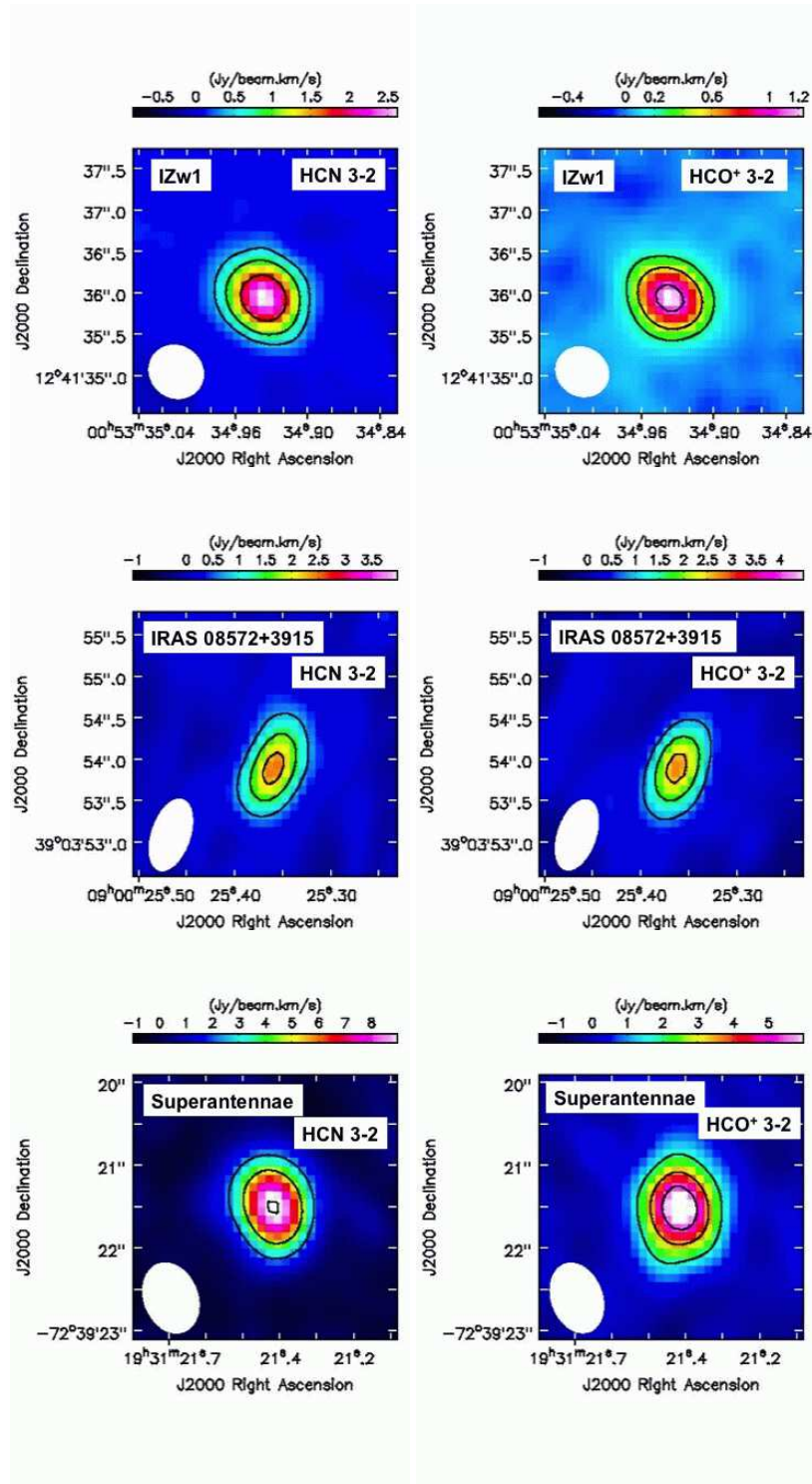
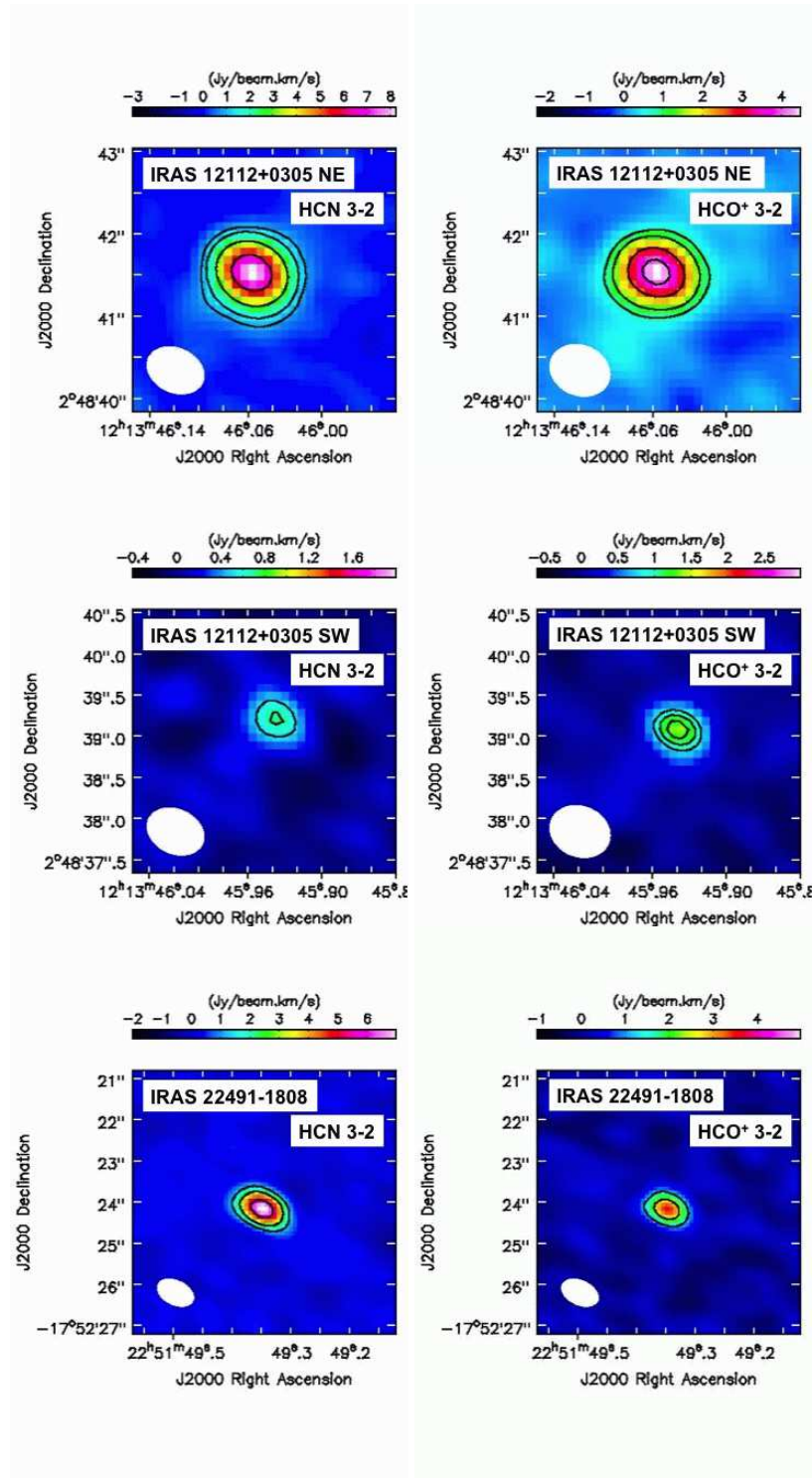
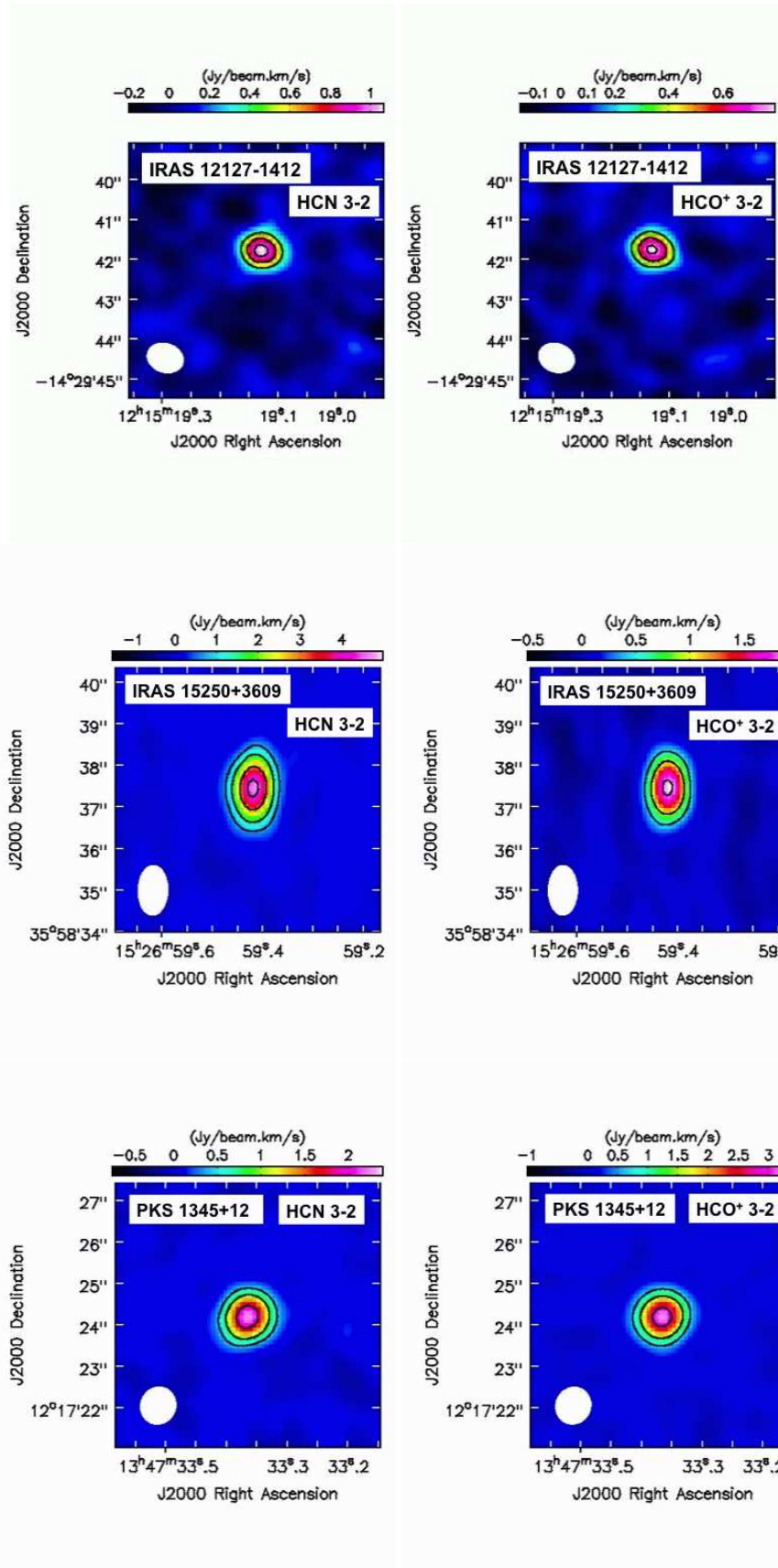


FIG. 7.— Integrated intensity (moment 0) maps of the HCN J=3-2 and HCO<sup>+</sup> J=3-2 emission lines, and their Gaussian fits in the spectra at individual locations within the beam size, for NGC 1614. The contours of the moment 0 maps are 3 $\sigma$ , 4 $\sigma$  for HCN J=3-2, and 3 $\sigma$ , 5 $\sigma$ , 7 $\sigma$  for HCO<sup>+</sup> J=3-2.









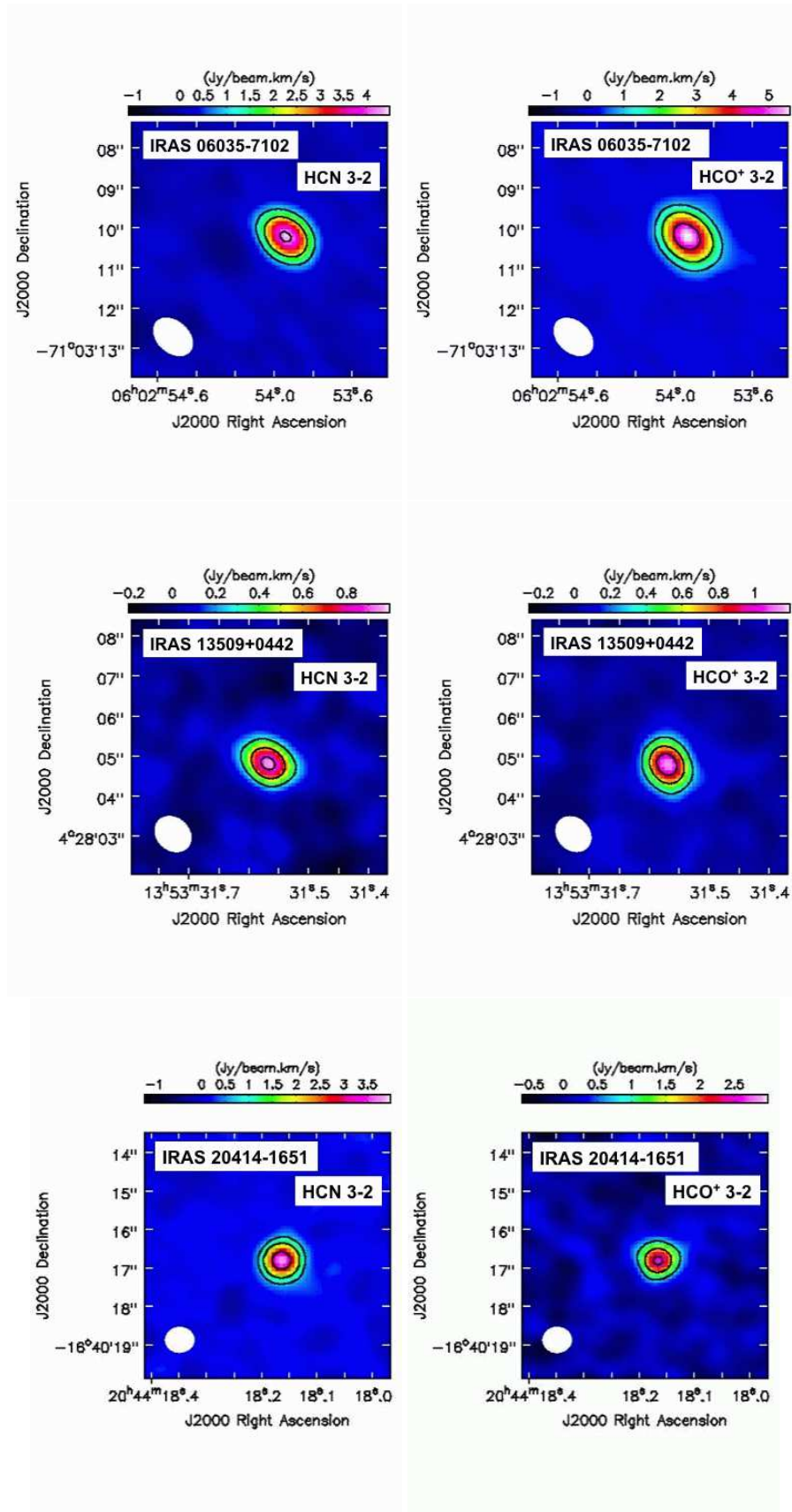
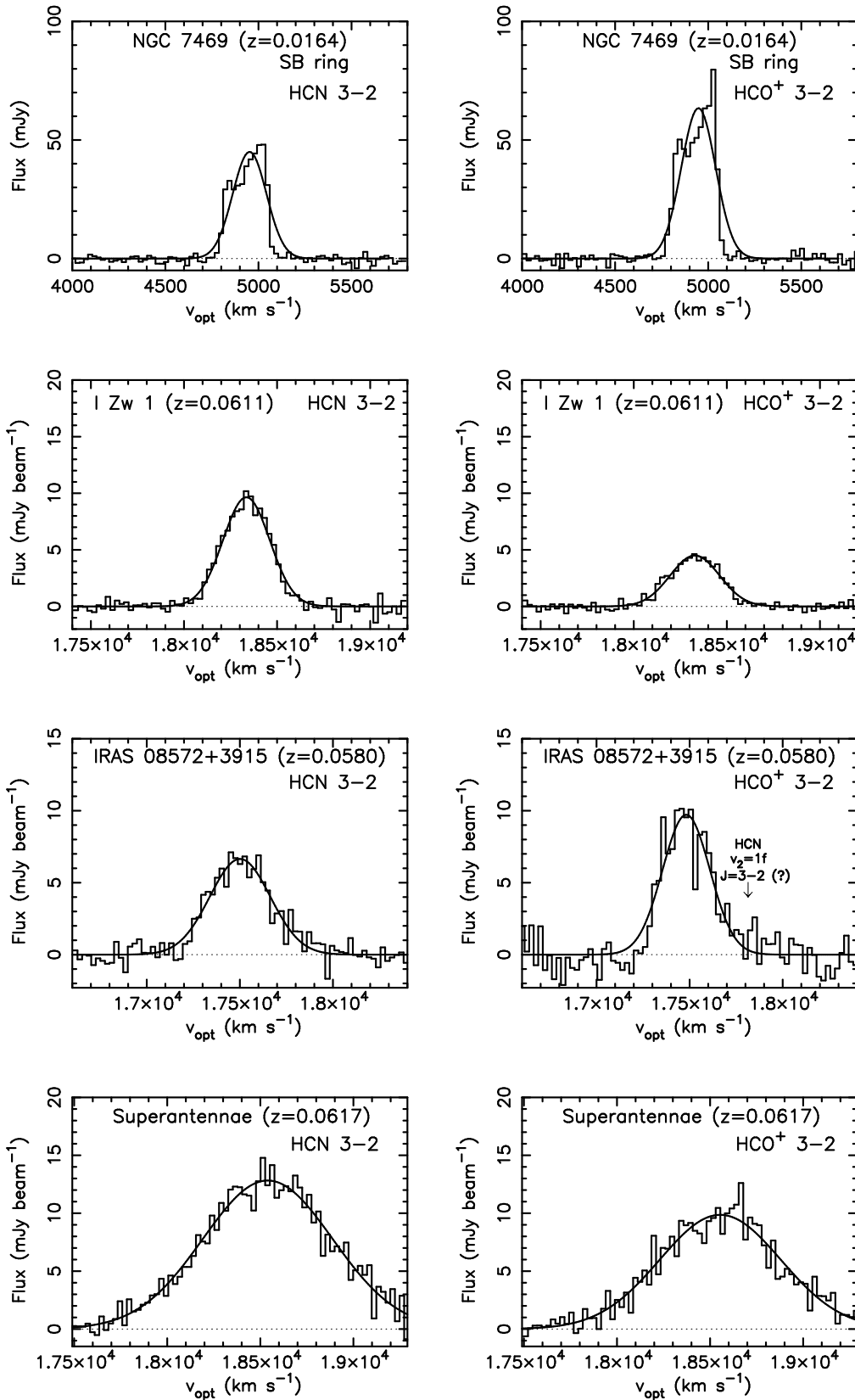
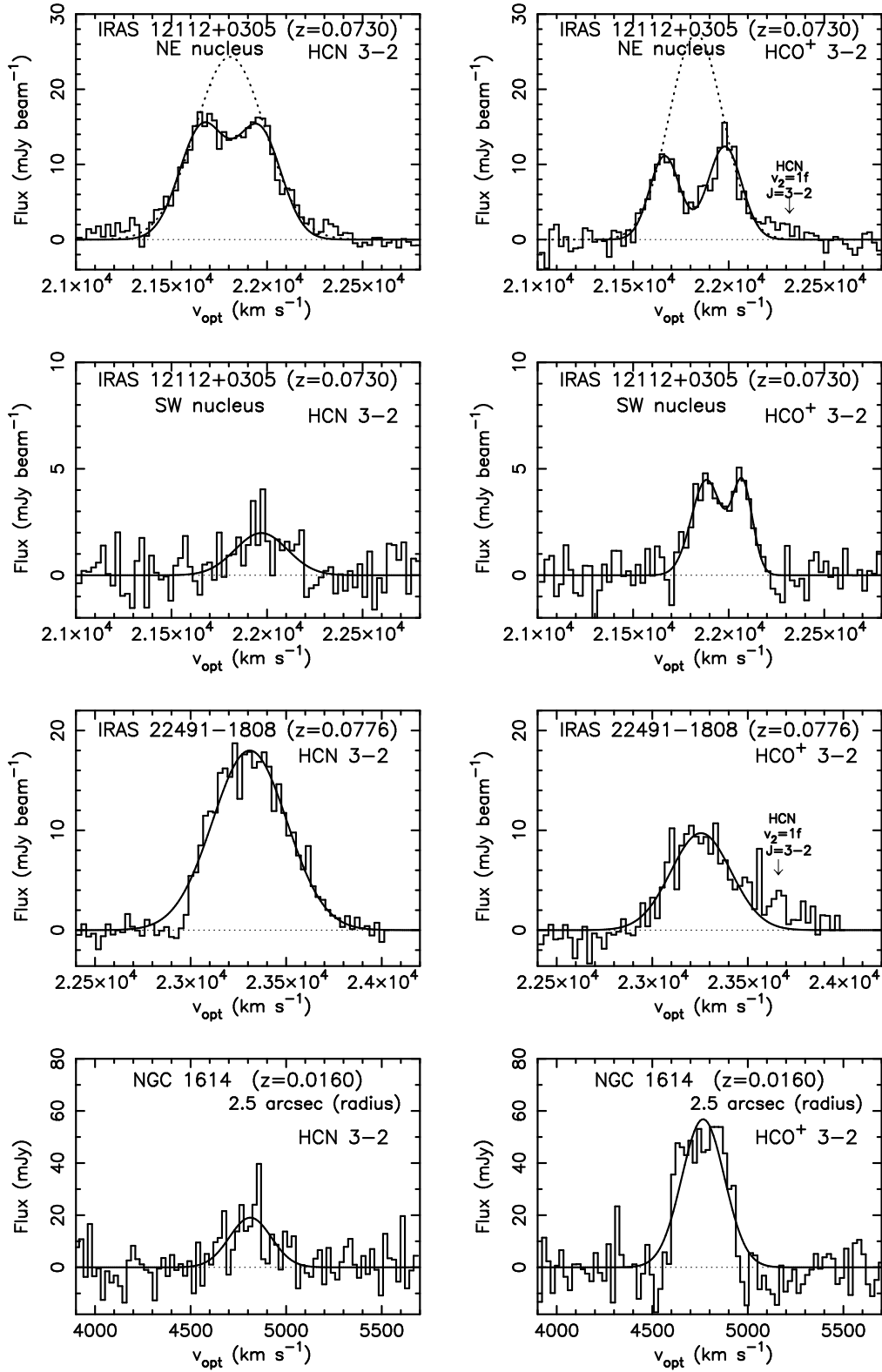
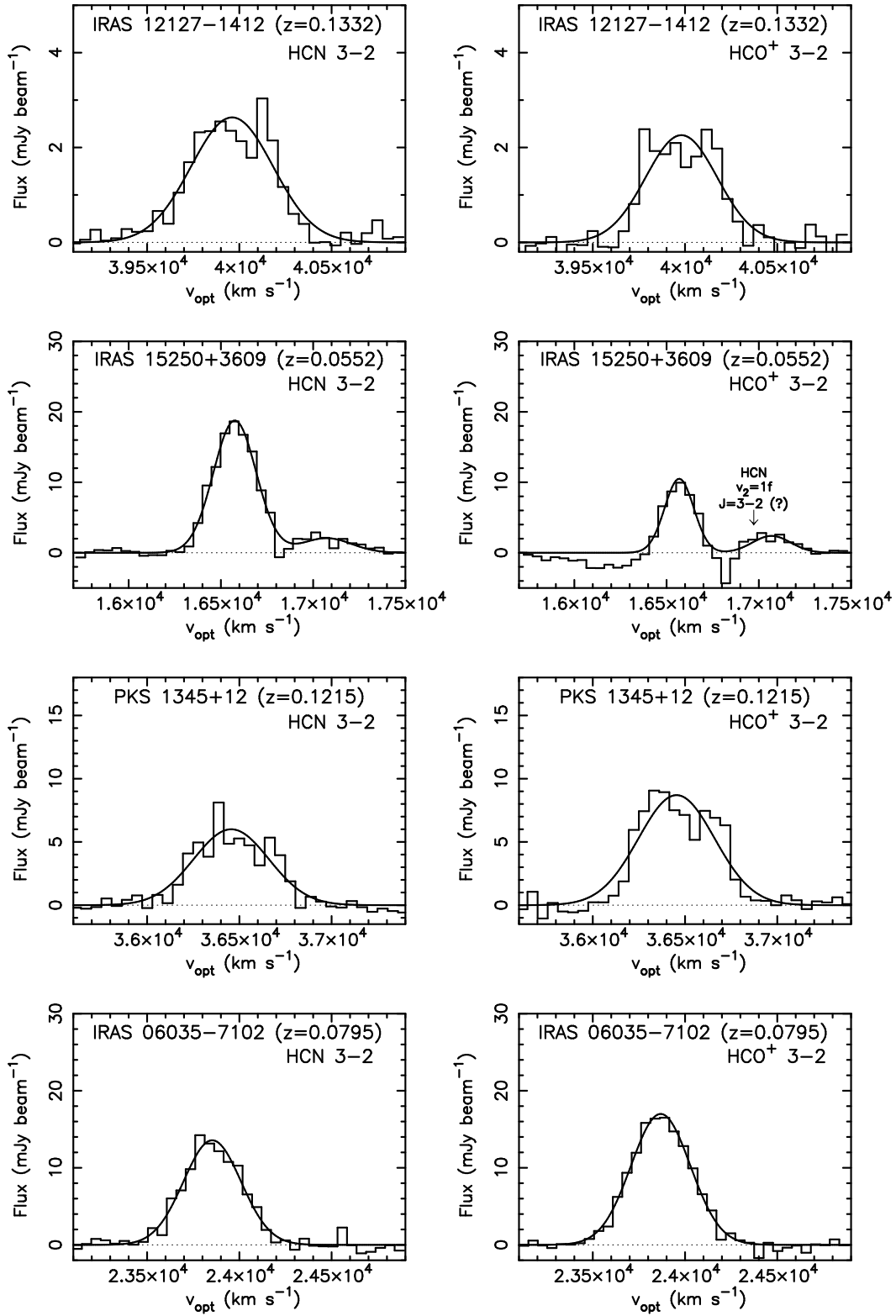


FIG. 8.— Integrated intensity (moment 0) maps of HCN J=3–2 (left) and HCO<sup>+</sup> J=3–2 (right). For I Zw 1, the contours are  $5\sigma$ ,  $10\sigma$ ,  $20\sigma$  for both HCN J=3–2 and HCO<sup>+</sup> J=3–2. For IRAS 08572+3915, the contours are  $4\sigma$ ,  $8\sigma$ ,  $12\sigma$  for both HCN J=3–2 and HCO<sup>+</sup> J=3–2. For The Superantennae, the contours are  $5\sigma$ ,  $10\sigma$ ,  $20\sigma$  for HCN J=3–2, and  $5\sigma$ ,  $10\sigma$ ,  $15\sigma$  for HCO<sup>+</sup> J=3–2. For IRAS 12112+0305 NE, the contours are  $3\sigma$ ,  $5\sigma$ ,  $10\sigma$ ,  $20\sigma$  for HCN J=3–2, and  $3\sigma$ ,  $5\sigma$ ,  $10\sigma$ ,  $15\sigma$  for HCO<sup>+</sup> J=3–2. For IRAS 12112+0305 SW, the contours are  $3\sigma$ ,  $4\sigma$  for HCN J=3–2, and  $4\sigma$ ,  $5\sigma$ ,  $6\sigma$  for HCO<sup>+</sup> J=3–2. For IRAS 22491–1808, the contours are  $5\sigma$ ,  $10\sigma$ ,  $20\sigma$  for HCN J=3–2, and  $5\sigma$ ,  $10\sigma$  for HCO<sup>+</sup> J=3–2. For IRAS 12127–1412, the contours are  $5\sigma$ ,  $8\sigma$ ,  $11\sigma$  for HCN J=3–2, and  $4\sigma$ ,  $7\sigma$ ,  $10\sigma$  for HCO<sup>+</sup> J=3–2. For IRAS 15250+3609, the contours are  $5\sigma$ ,  $10\sigma$ ,  $20\sigma$ ,  $30\sigma$  for HCN J=3–2, and  $5\sigma$ ,  $10\sigma$ ,  $20\sigma$  for HCO<sup>+</sup> J=3–2. For PKS 1345+12, the contours are  $4\sigma$ ,  $8\sigma$ ,  $16\sigma$  for HCN J=3–2, and  $6\sigma$ ,  $12\sigma$ ,  $24\sigma$  for HCO<sup>+</sup> J=3–2. For IRAS 06035–7102, the contours are  $6\sigma$ ,  $12\sigma$ ,  $24\sigma$  for both HCN J=3–2 and HCO<sup>+</sup> J=3–2. For IRAS 13509+0442, the contours are  $4\sigma$ ,  $8\sigma$ ,  $12\sigma$  for HCN J=3–2, and  $5\sigma$ ,  $10\sigma$ ,  $15\sigma$  for HCO<sup>+</sup> J=3–2. For IRAS 20414–1651, the contours are  $5\sigma$ ,  $10\sigma$ ,  $20\sigma$  for HCN J=3–2, and  $4\sigma$ ,  $8\sigma$ ,  $12\sigma$  for HCO<sup>+</sup> J=3–2.







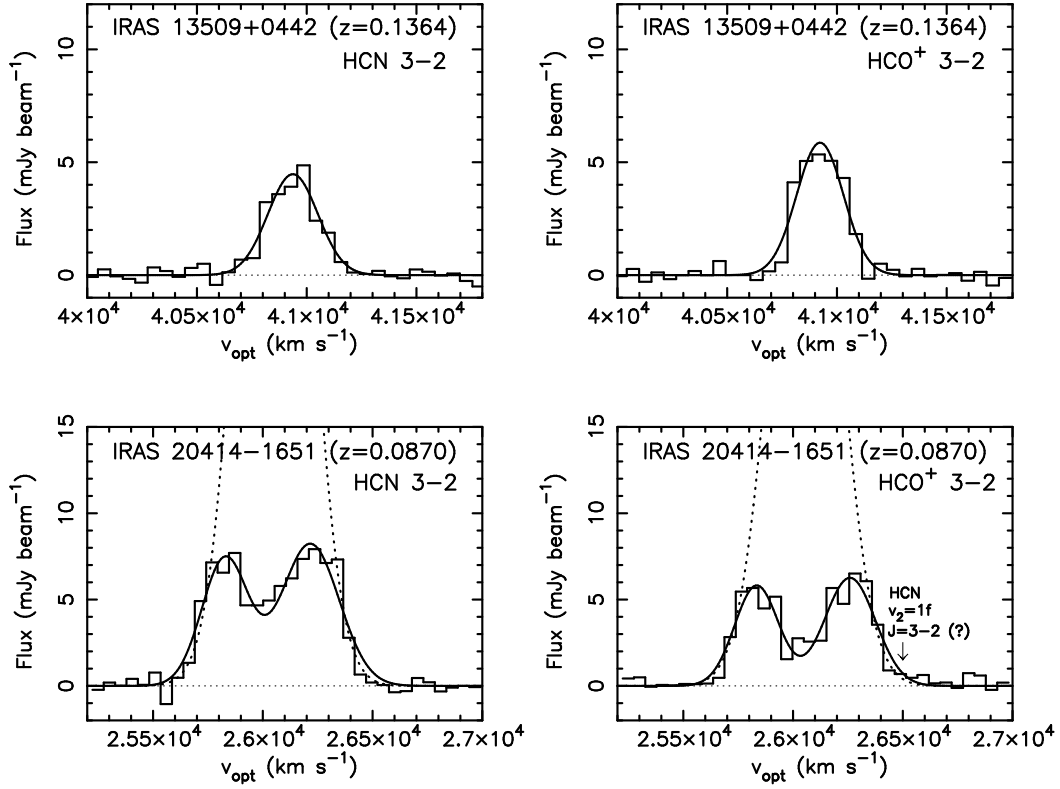


FIG. 9.— Gaussian fits to the detected HCN J=3–2 (left) and HCO<sup>+</sup>J=3–2 (v=0) (right) emission lines. For NGC 7469 and NGC 1614, Gaussian fits to the detected HCN J=3–2 and HCO<sup>+</sup>J=3–2 (v=0) emission lines from the integrated starburst regions, 0<sup>′</sup>.8–2<sup>′</sup>.5 radius annulus around the nucleus for NGC 7469, and circular region with 2<sup>′</sup>.5 radius around (04 34 00.03, –08 34 44.6)J2000 for NGC 1614, are shown here. For the IRAS 22491–1808 HCO<sup>+</sup> J=3–2 emission line, the frequency which can largely be contaminated by the HCN v<sub>2</sub>=1f J=3–2 emission line is excluded from the Gaussian fit. For IRAS 15250+3609, a Gaussian fit to the fainter sub-peak component is added, after fixing the best Gaussian fit to the main component. For objects with clear double-peaked HCN J=3–2 and HCO<sup>+</sup> J=3–2 emission line profiles (IRAS 12112+0305 NE and IRAS 20414–1651), single Gaussian fits using data points at the edge of the emission tail, after removing data possibly affected by the central dip (based on the assumption of self-absorption), are also shown with curved dashed lines.

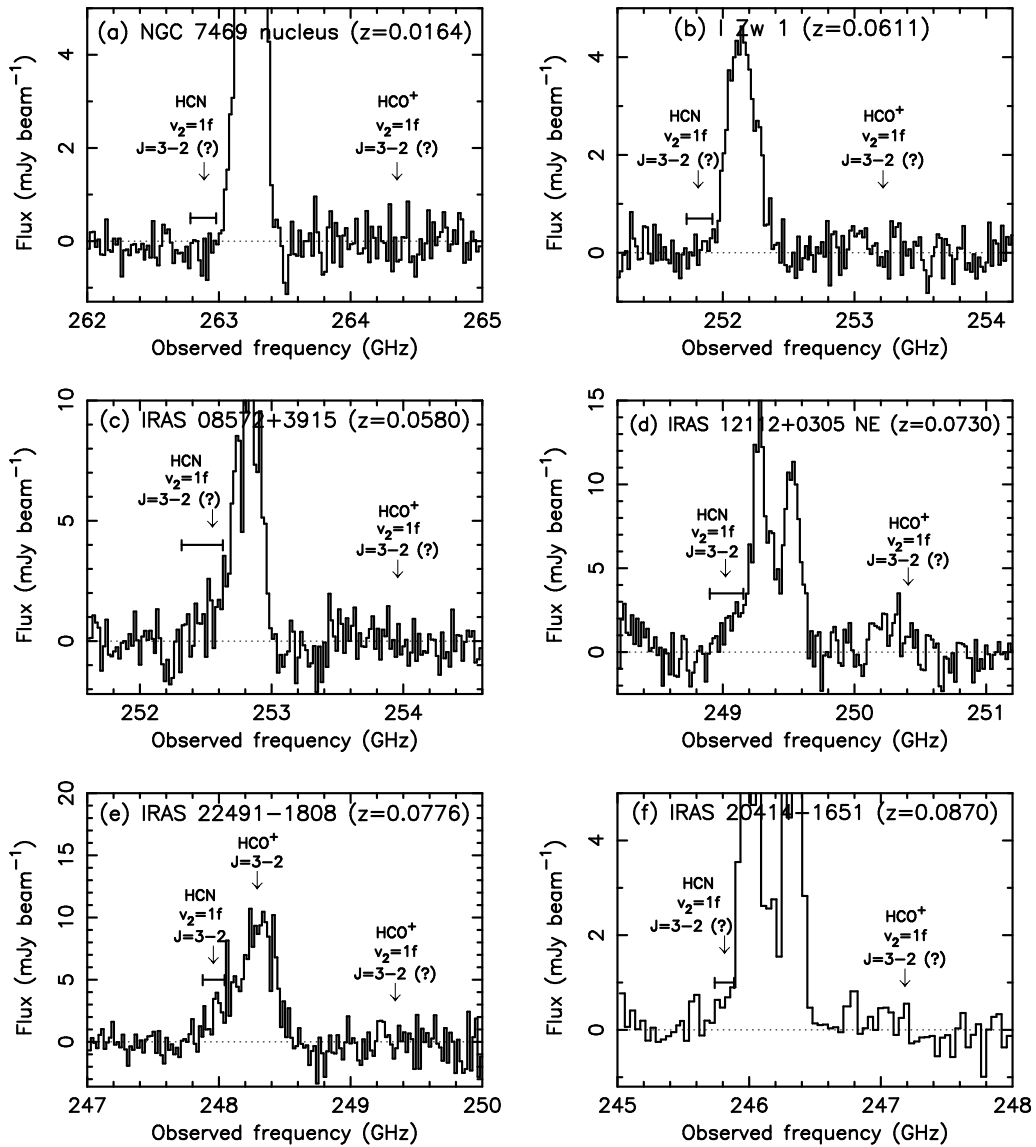


FIG. 10.— Zoomed-in spectra for selected sources to better display possible vibrationally excited ( $v_2=1f$ ) HCN  $J=3-2$  and  $\text{HCO}^+$   $J=3-2$  emission lines. The horizontal solid straight lines, inserted by short vertical solid lines, are frequency ranges used to estimate the flux of the HCN  $v_2=1f$   $J=3-2$  emission line.



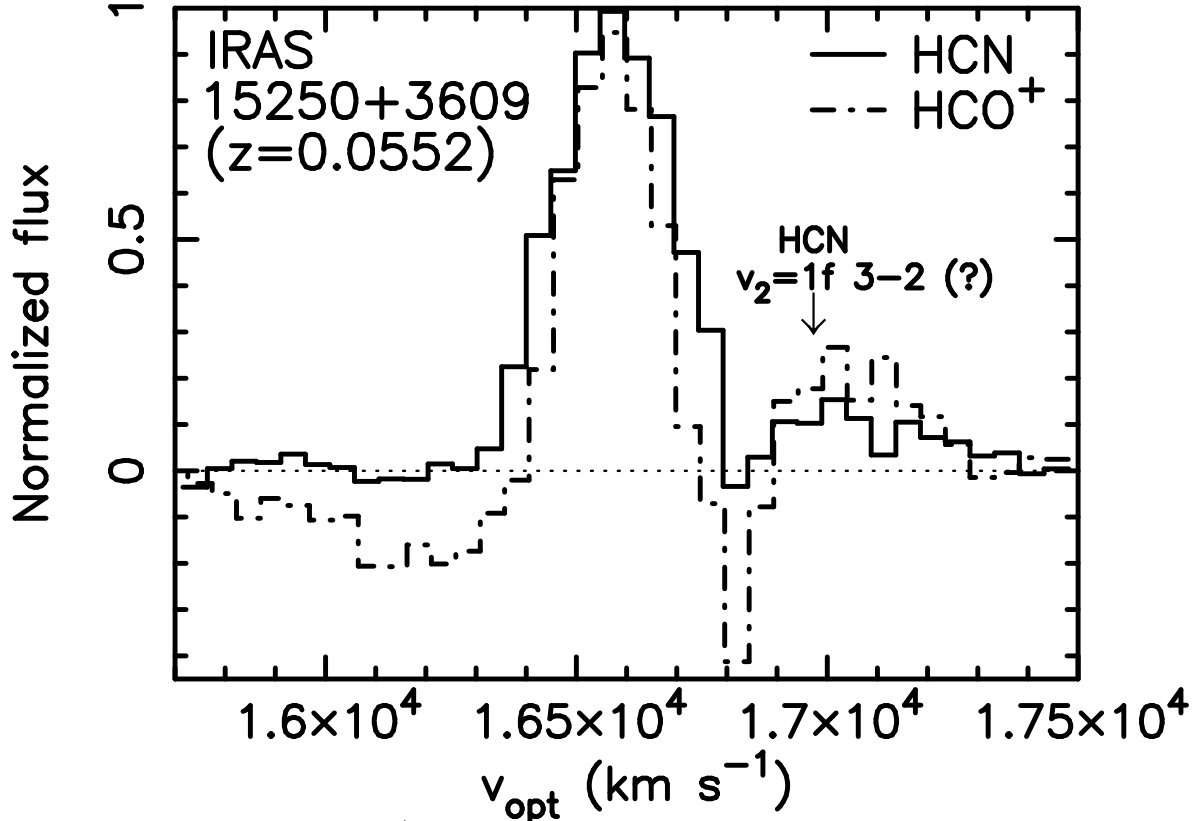


FIG. 11.— Comparison of HCN J=3-2 and HCO<sup>+</sup> J=3-2 emission line profiles for IRAS 15250+3609, after normalizing the Gaussian-fit peak flux for the brighter main component. Solid and dash-dotted lines represent HCN J=3-2 and HCO<sup>+</sup> J=3-2 emission line profiles, respectively. The expected position in the abscissa, of the HCN  $v_2=1f$  J=3-2 emission at  $z = 0.0552$  is shown as a down arrow for the HCO<sup>+</sup> J=3-2 emission line profile (dash-dotted line).

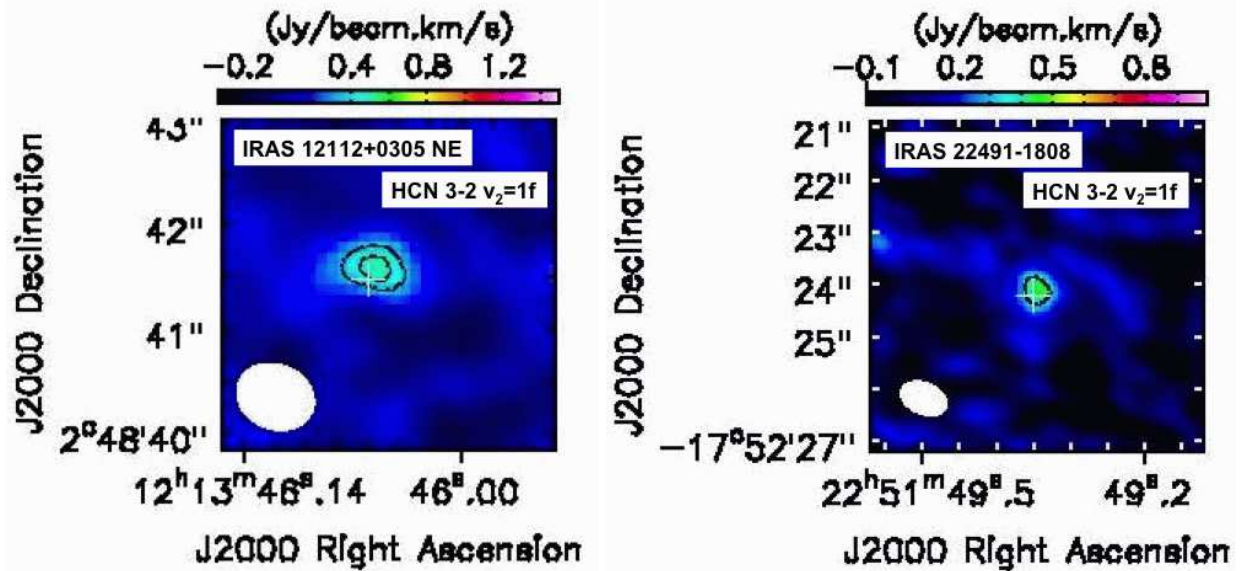
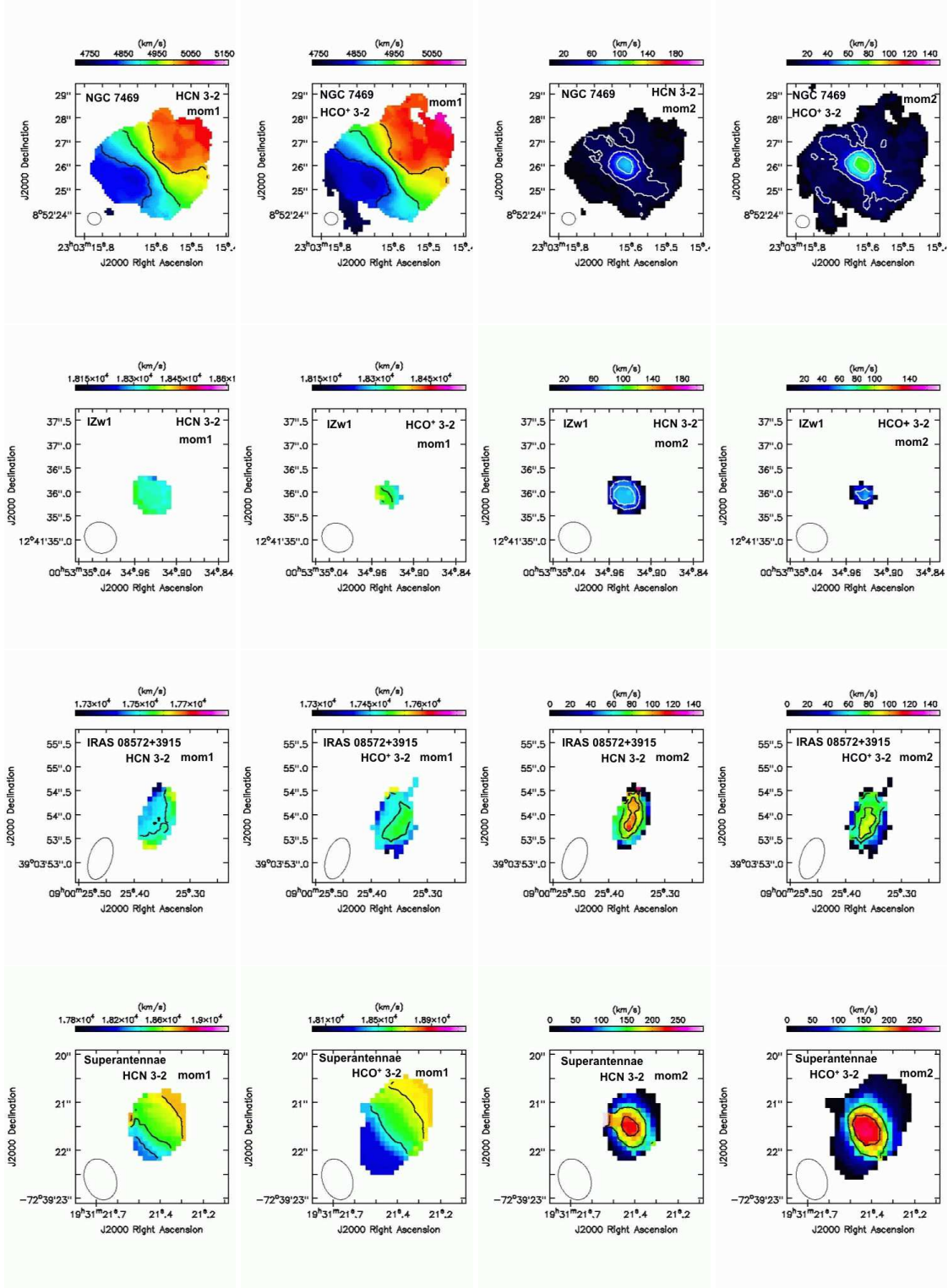
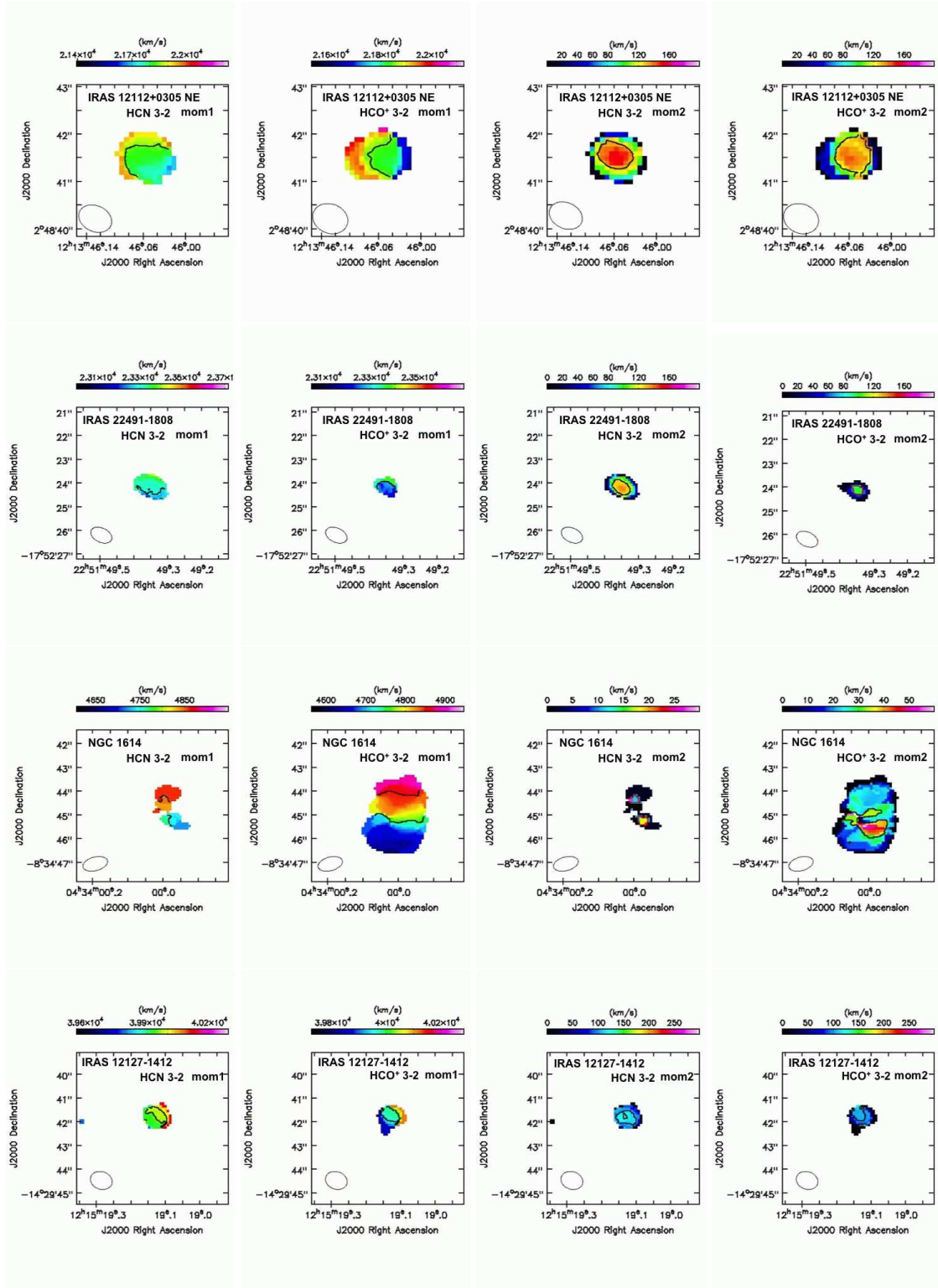
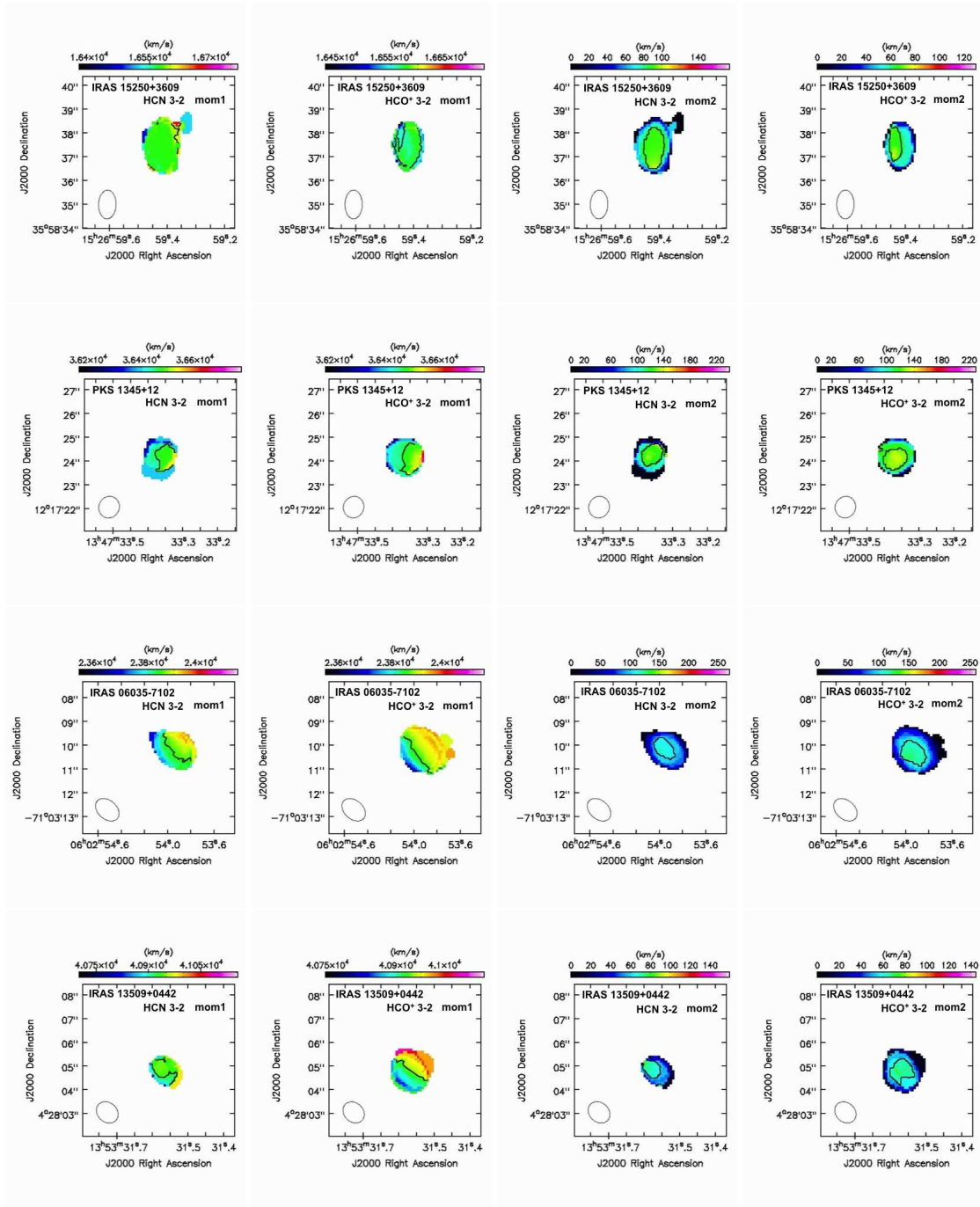


FIG. 12.— Integrated intensity (moment 0) maps of the HCN  $v_2=1f$  J=3-2 emission line of IRAS 12112+0305 NE and IRAS 22491-1808. Data at the frequency marked with a solid straight line inserted by two vertical lines in Figure 10, are used. The contours are  $3\sigma$  and  $4\sigma$  for IRAS 12112+0305 NE, and  $3\sigma$  for IRAS 22491-1808. The continuum peak positions are indicated with white crosses.







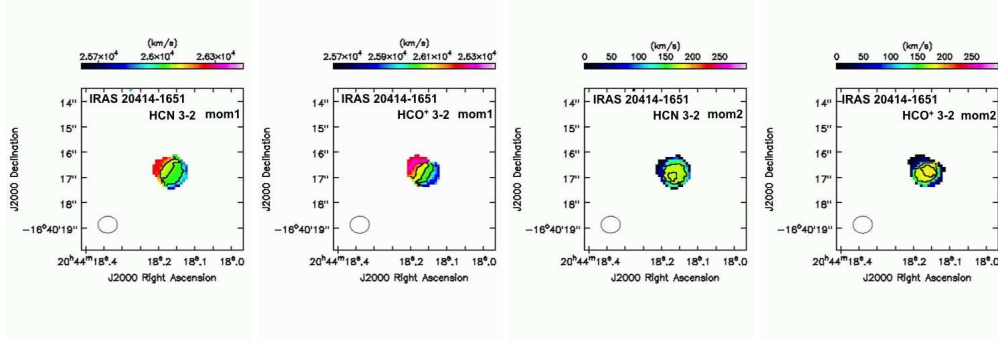


FIG. 13.— Intensity-weighted mean velocity (moment 1) and intensity-weighted velocity dispersion (moment 2) maps of the HCN J=3–2 and HCO<sup>+</sup> J=3–2 emission lines. An appropriate cut-off was applied so that the resulting maps are not dominated by noise. The left two panels are moment 1 maps. The contours represent 4850, 4925, 5000 km s<sup>−1</sup> for NGC 7469 HCN J=3–2 and HCO<sup>+</sup> J=3–2, no contour for I Zw 1 HCN J=3–2, 18335 km s<sup>−1</sup> for I Zw 1 HCO<sup>+</sup> J=3–2, 17500 km s<sup>−1</sup> for IRAS 08572+3915 HCN J=3–2, 17480 km s<sup>−1</sup> for IRAS 08572+3915 HCO<sup>+</sup> J=3–2, 18300, 18500, 18700 km s<sup>−1</sup> for The Superantennae HCN J=3–2, 18500, 18700 km s<sup>−1</sup> for The Superantennae HCO<sup>+</sup> J=3–2, 21850 km s<sup>−1</sup> for IRAS 12112+0305 NE HCN J=3–2 and HCO<sup>+</sup> J=3–2, 23300 km s<sup>−1</sup> for IRAS 22491–1808 HCN J=3–2 and HCO<sup>+</sup> J=3–2, 4750, 4850 km s<sup>−1</sup> for NGC 1614 HCN J=3–2 and HCO<sup>+</sup> J=3–2, 39960, 40000 km s<sup>−1</sup> for IRAS 12127–1412 HCN J=3–2 and HCO<sup>+</sup> J=3–2, 16600 km s<sup>−1</sup> for IRAS 15250+3609 HCN J=3–2, 16560 km s<sup>−1</sup> for IRAS 15250+3609 HCO<sup>+</sup> J=3–2, 36460 km s<sup>−1</sup> for PKS 1345+12 HCN J=3–2 and HCO<sup>+</sup> J=3–2, 22090 km s<sup>−1</sup> for IRAS 06035–7102 HCN J=3–2 and HCO<sup>+</sup> J=3–2, 40930 km s<sup>−1</sup> for IRAS 13509+0442 HCN J=3–2 and HCO<sup>+</sup> J=3–2, and 26000, 26060, 26120 km s<sup>−1</sup> for IRAS 20414–1651 HCN J=3–2 and HCO<sup>+</sup> J=3–2. The right two panels are moment 2 maps. The contours represent 20, 45, 70 km s<sup>−1</sup> for NGC 7469 HCN J=3–2 and HCO<sup>+</sup> J=3–2, 50, 70 km s<sup>−1</sup> for I Zw 1 HCN J=3–2, 70 km s<sup>−1</sup> for I Zw 1 HCO<sup>+</sup> J=3–2, 78, 96 km s<sup>−1</sup> for IRAS 08572+3915 HCN J=3–2, 66, 81 km s<sup>−1</sup> for IRAS 08572+3915 HCO<sup>+</sup> J=3–2, 150, 210 km s<sup>−1</sup> for The Superantennae HCN J=3–2 and HCO<sup>+</sup> J=3–2, 130 km s<sup>−1</sup> for IRAS 12112+0305 NE HCN J=3–2, 120 km s<sup>−1</sup> for IRAS 12112+0305 NE HCO<sup>+</sup> J=3–2, 120 km s<sup>−1</sup> for IRAS 22491–1808 HCN J=3–2, 100 km s<sup>−1</sup> for IRAS 22491–1808 HCO<sup>+</sup> J=3–2, 10 km s<sup>−1</sup> for NGC 1614 HCN J=3–2, 30 km s<sup>−1</sup> for NGC 1614 HCO<sup>+</sup> J=3–2, 110, 125 km s<sup>−1</sup> for IRAS 12127–1412 HCN J=3–2, 102 km s<sup>−1</sup> for IRAS 12127–1412 HCO<sup>+</sup> J=3–2, 90 km s<sup>−1</sup> for IRAS 15250+3609 HCN J=3–2, 63 km s<sup>−1</sup> for IRAS 15250+3609 HCO<sup>+</sup> J=3–2, 118 km s<sup>−1</sup> for PKS 1345+12 HCN J=3–2, 120 km s<sup>−1</sup> for PKS 1345+12 HCO<sup>+</sup> J=3–2, 104 km s<sup>−1</sup> for IRAS 06035–7102 HCN J=3–2, 110 km s<sup>−1</sup> for IRAS 06035–7102 HCO<sup>+</sup> J=3–2, 60 km s<sup>−1</sup> for IRAS 13509+0442 HCN J=3–2, 62 km s<sup>−1</sup> for IRAS 13509+0442 HCO<sup>+</sup> J=3–2, 164, 174 km s<sup>−1</sup> for IRAS 20414–1651 HCN J=3–2, and 170, 184 km s<sup>−1</sup> for IRAS 20414–1651 HCO<sup>+</sup> J=3–2.

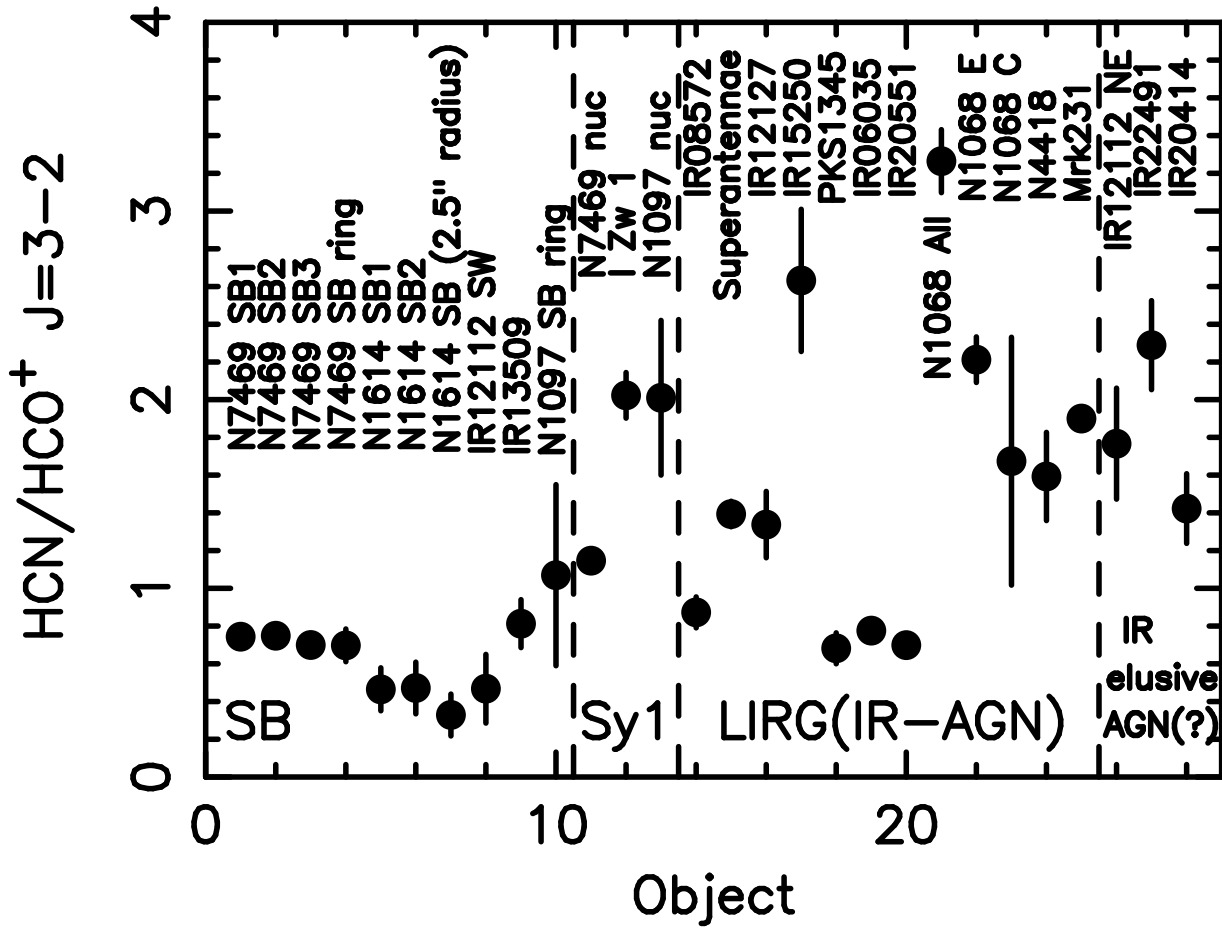


FIG. 14.— The HCN J=3–2 to HCO<sup>+</sup> J=3–2 flux ratio of observed galaxies with interferometry. Sources are categorized into starburst-dominated regions, denoted as “SB” (left), optical Seyfert 1 galaxies, denoted as “Sy1” (second left), and LIRGs which are infrared-diagnosed to contain luminous obscured AGNs, denoted as “LIRG(IR-AGN)” (second right). LIRGs which have no obvious infrared AGN indicators, but show signatures of vibrationally excited HCN  $v_2=1f$  J=3–2 emission lines, are denoted as “IR elusive AGN (?)” (right). ALMA interferometric data for IRAS 20551–4250 (Imanishi et al. 2016a) and NGC 1068 (Imanishi et al. 2016b), SMA interferometric data for NGC 1097 (Hsieh et al. 2012) and NGC 4418 (Sakamoto et al. 2010), and PdBI interferometric data for Mrk 231 (Aalto et al. 2015a) are included, in addition to the sources observed in this paper. For NGC 1068, data from the nuclear area-integrated emission within a  $2''.4$  radius circular region (denoted as “N1068 All”), molecular gas emission peak at the eastern side of the AGN (denoted as “N1068 E”), and the continuum peak as the putative location of an AGN (denoted as “N1068 C”) (Imanishi et al. 2016b), are shown.

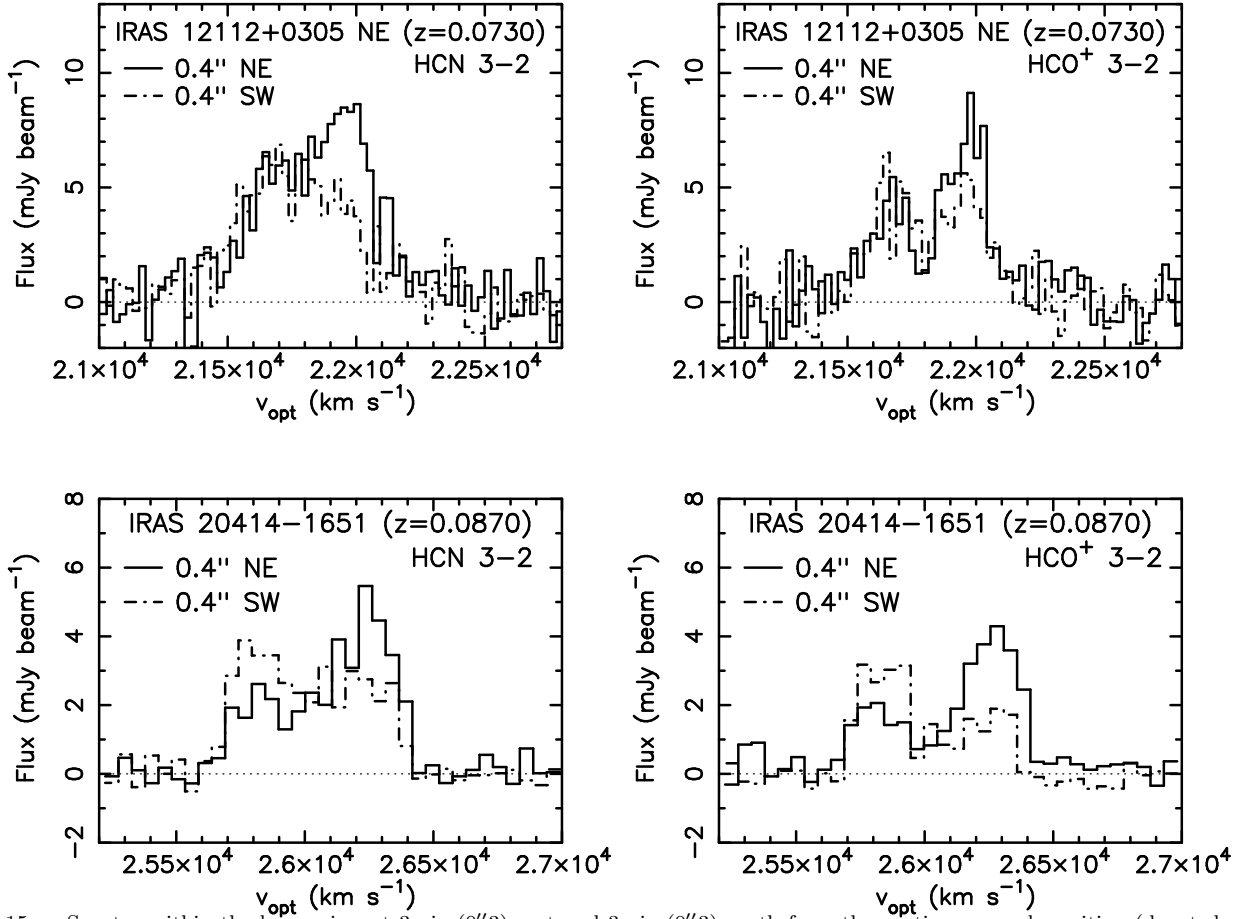


FIG. 15.— Spectra within the beam size, at 3 pix (0''.3) east and 3 pix (0''.3) north from the continuum peak position (denoted as 0.4'' NE and displayed with the solid line), and at 3 pix (0''.3) west and 3 pix (0''.3) south from the continuum peak position (denoted as 0.4'' SW and displayed with the dash-dotted line) for IRAS 12112+0305 NE and IRAS 20414–1651. In the intensity-weighted mean velocity (moment 1) maps of both objects, the north-eastern part is more redshifted than the south-western part.

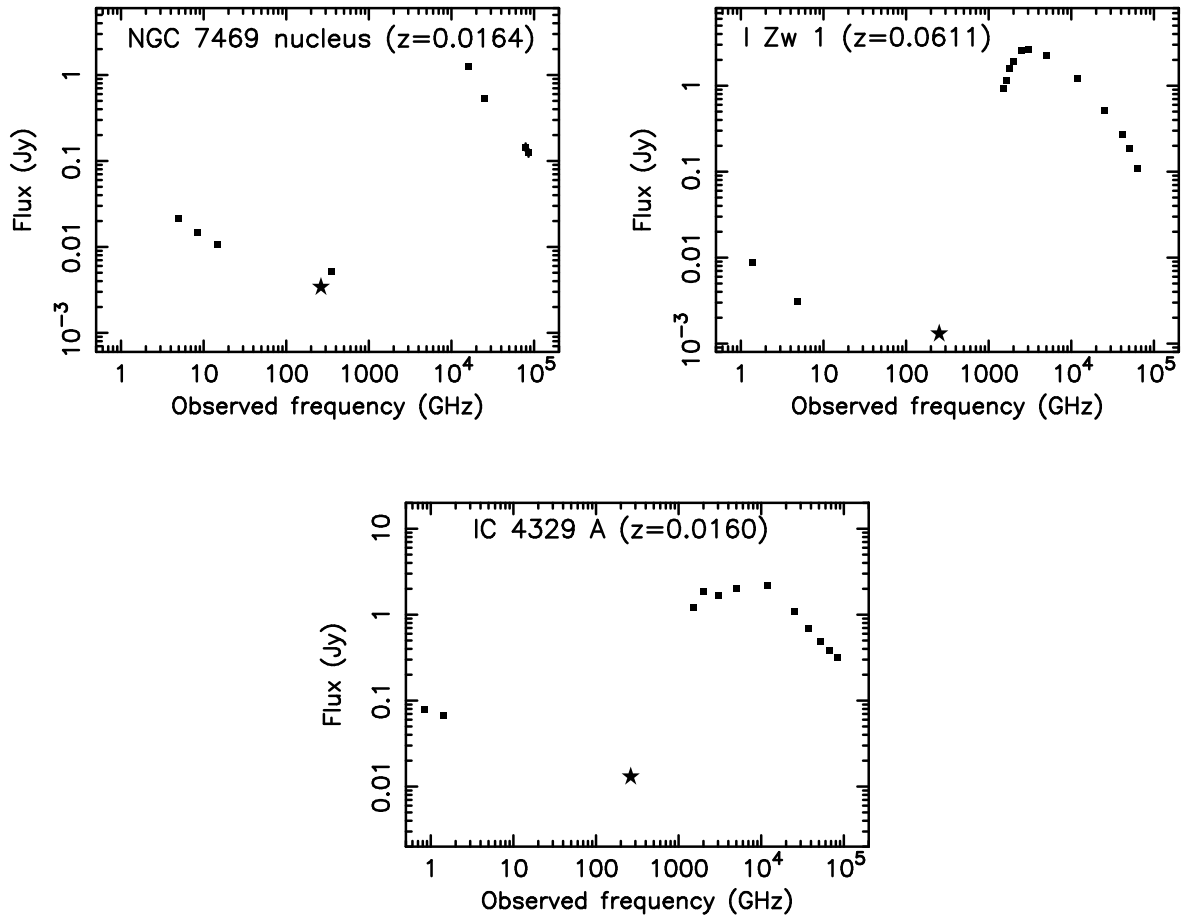


FIG. 16.— Spectral energy distribution from  $3 \mu\text{m}$  ( $10^5$  GHz) to radio ( $\sim 1$  GHz). Filled stars are from our ALMA Cycle 1 observations and filled squares are from the literature. For NGC 7469, following Izumi et al. (2015), we adopt flux measurement for the nuclear component only (Marco & Alloin 1998; Reunanen et al. 2010; Izumi et al. 2015; Wilson et al. 1991; Orienti & Prieto 2010), to remove the contamination from the spatially extended starburst ring. For I Zw 1 and IC 4329 A, we use data from the NASA/IPAC Extragalactic Database to derive the total flux at an individual frequency.